Istituto Universitario degli Studi Superiori di Pavia

On the use of anisotropic triangles in an *immersed* finite element approach with application to fluid-structure interaction problems

by

ADRIEN LEFIEUX

A Thesis Submitted in Partial Fulfillment of the Requirements for the Degree of Doctor in Philosophy in

Computational Mechanics and Advanced Materials

Supervisor:	**Prof. F. Auricchio**	Università degli Studi di Pavia
Coadvisors:	**Prof. A. Reali**	Università degli Studi di Pavia
	Prof. A. Veneziani	Emory University

XXVI Ciclo (2010-2014)

Summary

Solutions to engineering problems depend more and more on numerical methods. One of these methods, the so-called finite element method, has acquired over the years a central role in solving such problems. Its versatility relies on the capacity of the method to discretize the physical domain of the problem into simple elements: triangles, quadrilateral, tetrahedra, etc. However, for problems with complex geometries, interfaces, or involving important topological changes in time such as fluid-structure interaction problems, the construction of the domain partition becomes a bottleneck. Many solutions have been proposed, such as the so-called immersed approaches.

Moving from this framework, in the present work we first analyze several immersed strategies from the literature. A noticed crucial issue is the accuracy of immersed finite elements approaches. The goal of the present work is to provide an accurate immersed method.

The envisaged strategy consists in locally remeshing elements cut by the structure. A notable feature of this approach is the presence of anisotropic or distorted elements. Such elements are non-standard and many questions remain open such as their inf-sup stability with mixed finite elements for incompressible flows, especially for triangles. We first focus on the Hood-Taylor element and we show inf-sup stability issues in the remeshing strategy, but inf-sup instability is obtained in rare occasions, and thus this mixed element may be inf-sup stable for wide range of applications. Nevertheless, we present a strategy to stabilizes the element.

Finally, we present a fluid-structure interaction problem with an thin hinged rigid leaflet to which we apply the locally remeshing strategy. In this problem, since the pressure is likely to be discontinuous across the solid, mixed elements with discontinuous pressures are a natural choice. Again, we focus on inf-sup stability issues for two common mixed elements with discontinuous pressures, namely the schemes with constant and with discontinuous piecewise linear pressures. We show that these two elements are likely to be inf-sup unstable when the distortion of the mesh is important, while the elements with continuous pressures studied in this work remain inf-sup stable, though they are not straightforward to implement since discontinuity across the structure must be taken into account.

Keywords: mixed finite elements, incompressible viscous flows, fluid-structure interaction, Stokes and Navier-Stokes equations, immersed methods, anisotropic meshes

To Neha Gill

A mathematician's nightmare is a sequence n_ϵ that tends to 0 as ϵ becomes infinite.

Paul R. Halmos

Acknowledgments

I first would like to thank my advisor, Ferdinando Auricchio, for giving me the opportunity to write this thesis and for supporting me. Undoubtedly, without him, this thesis would never have been finished. Beyond scientific knowledge gained from him during the realization of this thesis I would like to thank him for teaching me rigor in scientific research.

I would also like to express my deep gratitude to my co-advisors Alessandro Reali and Alessandro Veneziani for their continuous help. The first Alessandro, for his critical insight on my work and his support from day one and the second Alessandro for getting me into the world of parallel Navier-Stokes equations, fluid-structure interaction, and much more, in particular in italian. A special thank to him for hosting me twice in Decatur at Emory University.

I also thank my collaborators from the mathematical side of Pavia (on the other side of the window) Daniel Boffi, Lucia Gastaldi and Franco Brezzi. In particular Franco Brezzi for the time he took to help me understanding the inf-sup condition. There still is so much to learn...

Allora, prima di continuare, vorrei ringraziare l'Italia e gli italiani per l'ospitalita e per l'accoglienza ricevuta in questi anni. Ho imparato a dire "buongiorno" solo sul primo treno verso Milano. Pensavo bastasse l'inglese, ma dopo una settimana in Italia mi sono reso conto che non era cosi. Mi ci e voluto un po' di tempo e qualche risata prima di iniziare a distinguere i vari accenti italiani, incroyabile. Suddivido le persone conosciute in Italia, italiani e non, in due gruppi, che in realtà coincidono nella maggior parte dei casi: i colleghi e gli amici. Parlo dei miei colleghi Josef, Chiara, Chiara, Anna, Giuseppe, Andrea, Carolina, Isabella, Paolo, Stephania, Rodrigo, Giulia, Elisa, Mauro, Simone e Michele. Ma anche dei miei amici: Eli, Giuso, Doni, Etienne, Valeria, Laura, Alessia, Fabrizio, e tutti gli altri che ho conosciuto.

J'arrive maintenant a la partie française, aux potes historiques de la Normandie, Maxou, Annabelle, Riton, Mamat, Louloute, JeJe, Lucie, Simon, Louise, Momo, Glawy, Pompom, Romain ... et aux amis de l'UTC : Manu, Gauthier, Saka, Brice, Mehdi, Marie ... Cette thèse n'aurait pas non plus vu le jour sans le soutien de mon conseiller de fin d'étude de mon cycle d'ingénieur Jean-François Sigrist et Serguey Iakovlev qui m'a informé à-propos de ce programme de doctorat. Mais avant tout, je tiens à remercier mes parents sans qui l'aboutissement de ce travail n'aurait pas eu lieu, pour leur indéfectible support. Je remercie aussi mon frère avec qui j'ai partagé tant, et avec qui je compte bien continuer.

Ultimo ma non meno importante, ringrazio gli italiani, with one exception for not being italian, dall'altro lato dell'Atlantico ad Emory University, Luca, Tiziano, Simona, Marina e Leandro.

Contents

List of Figures

List of Tables

CHAPTER 1

Introduction

In this thesis we deal with fluid dynamics problems. In particular, we treat incompressible and viscous fluids, which are commonly described using the incompressible Navier-Stokes system of equations in the velocity-pressure formulation. These equations are based on the assumptions that: the fluid is incompressible, isothermal, the density constant, and Newtonian (i.e., the relation between the stress and the strain rate is linear). In particular, it follows that because the density is constant the conservation of mass reduces to the incompressibility constraint, that is the divergence of the velocity is null. Furthermore, because the fluid is isothermal the conservation of momentum and conservation of mass are decoupled from the conservation of energy.

Finding the analytical solution of the Navier-Stokes system of equations is often impossible. These solutions exist but only for simple data. As a consequence, we build a *discrete* model to the continuous one which we can solve using computers. The main idea is that, for u the solution of the continuous problem and u_h the solution of the discrete problem, where h is a parameter describing the discretization of the problem, we require that the error (in a suitable norm) $u - u_h$ tends to zero, as h tends to zero.

There are several techniques available to obtain a discrete problem associated to the continuous one. In this thesis, we deal with the finite element method. This method is based on the Bubnov-Galerkin method, i.e., by building a finite dimensional subspace of the space in which we seek a solution to a *weak* (integral) form of the discrete problem. The finite element method provides a procedure to build such a subspace. We first mesh the domain by dividing it into elements (e.g., triangles), we then associate a function (e.g., a polynomial) on each element, and finally we provide global (i.e, over the whole domain) regularity and differentiability properties to the set of functions defined on each element. The solution to the discrete problem, u_h, is thus sought in such a space and h is usually the diameter of the element.

A key issue of the finite element method is to measure how fast finite elements converge to the solution of the continuous problem. Roughly speaking, the rate of convergence of the finite element method depends on the degree of the polynomial, in case we use polynomials, and of the regularity of the solution of the continuous problem. For example, if the solution is sufficiently regular then piecewise linear elements converge quadratically in the L^2-norm. The regularity of the solution of the continuous problem may depend on the geometry of the domain, initial and boundary conditions, on the physical parameters of the equations as well as on the load.

The mixed finite element method is a common approach to solve incompressible fluid dynamics problems. In this method, the incompressibility constraint is enforced weakly via a Lagrange multiplier. Because we use the velocity-pressure formulation of the Navier-Stokes system of equations, the Lagrange multiplier corresponds to the pressure. As a consequence, two fields have to be discretized, hence the term mixed. The mixed finite element method explains, among other things, how to select the velocity and the pressure finite element spaces since they cannot be picked arbitrarily. The reason is that the well-posedness of the continuous problem does not extend automatically to the discrete one, on the contrary to the finite element method with the Bubnov-Galerkin approach. With mixed finite elements a specific condition for the discrete problem must be checked. In the literature that constraint is often named *inf-sup*.

Problems we have in mind are related to *interface* problems, in particular to fluid-structure interaction ones where the common boundary between the fluid and the solid defines the interface. For such type of problems, their solutions are expected to show singularities or discontinuities across the interface. However, the solution is likely to be regular away from the interface, and thus a strategy could be to find a way to correctly capture the singularities around the interface. We may divide such problems in two types: with *sharp* or *spread* interfaces. For the former, the interface is codimension one with respect to the geometry of the problem, while the latter is codimension zero. It implies that in the first case the singularity is sharp while, in the second case, it induces large gradients. In this work we only deal with sharp interfaces.

A common approach to solve sharp interface problems is to divide the "global" domain, i.e., the domain of definition of the problem, into *sub*-domains that are separated by interfaces. Then, *sub*-finite element spaces are built on each sub-domain and interfacial constraints are enforced between the spaces. If we look at the problem in this way we might see new issues, in particular for moving interfaces: how to build a mesh for the sub-domains and how to enforce the constraints at the interface.

Regarding the first issue, building meshes for the sub-domains is difficult and many methods, instead, retain a mesh for the global domain. As a consequence, they often loose accuracy because the finite element spaces do not catch the singularity or the discontinuities, in general because the elements of the mesh do not fit the interface. In the literature such an approach is called "immersed". The term "immersed" has to be taken in a broad sense, i.e., it includes methods such as the immersed boundary method, the fictitious domain, embedded and unfitted methods. The present work is grounded on immersed approaches and we aim at providing an accurate one.

The second issue is also an active area of research, especially regarding weak enforcement of interfacial constraints, i.e., the constraints are enforced in the weak formulation of the problem and not in the finite element spaces. In the present work we do not get into details regarding weak strategies for enforcing interfacial constraints. Rather, the method we present rely on strong enforcement of interfacial constraints, that is directly into the finite element spaces. However, some numerical examples with Lagrange multipliers for such constraints are presented as well as discussions of various weak approaches from the literature.

The core of the present work is based on a strategy that consists in remeshing solely the elements of the mesh of the global domain, that are cut by the interface. For 2D problems, such a strategy involves anisotropic triangles, which are very flat triangles. It is well-known that the finite element method retains optimal convergence on anisotropic meshes (under several conditions) but their use for incompressible flow problems with the mixed finite element method (which we describe later) has not been extensively discussed in the literature and not at all for the proposed remeshing strategy.

The mixed finite element method is well established and there exists many velocity-pressure schemes that have been formally proven to be inf-sup stable. However, most of the proofs require the mesh to be isotropic and the necessity of this assumption is an open issue for many mixed finite element schemes. However, we employ anisotropic elements and this issue is crucial and the present work provides new results regarding inf-sup stability of some common finite element schemes on anisotropic meshes and, in particular, in the context of the presented "immersed" approach. In this work we only deal with 2D problems and the results are presented for triangles.

1.1. Organization of the thesis

The thesis is divided in three main chapters.

The first main chapter deals with a 1D study of several methods found in the literature for interface problems, in particular for fluid-structure interaction ones. This work has been performed in collaboration with Lucia Gastaldi and Daniele Boffi. It has been published in [**7**].

The second main chapter discusses a method based on the conclusive considerations of the first one for the two-dimensional steady incompressible Stokes problem with an immersed boundary. In this chapter we do not have an interface but an immersed boundary. However, interfaces and immersed boundaries share, for our problems, two characteristics: they are immersed in the global domain and essential constraints are enforced on them. This chapter contains most of the necessary material for the interface problem discussed in the last chapter. As discussed before, the method we study consists in remeshing solely the elements of the mesh of the global domain that are crossed by the immersed boundary such that newly added elements, called sub-elements, fit the immersed boundary. We use such a subdivision strategy to build a new finite element basis such that we may: i) represent accurately the immersed boundary, and ii) impose Dirichlet boundary conditions on it in a strong way. However, the subdivision process may imply the generation of anisotropic elements, which, for the incompressible Stokes problem, may result in the loss of inf-sup stability even for well-known stable mixed finite element schemes. This chapter focuses on that issue with continuous pressure mixed finite elements. In particular, we test the Hood-Taylor element showing that it may not be stable in the present framework. We also demonstrate numerically that by adding a cubic bubble to the velocity space we stabilize the element on the generated anisotropic triangles. This work has been done jointly with Franco Brezzi and it has been published in [**8**].

The last main chapter applies the results of the second chapter to a fluid-structure interaction problem where the structure is a hinged rigid leaflet, i.e., a simple bar. Advantages are twofold: as pointed out in the second chapter, essential constraints between the fluid and the solid may be directly enforced in the finite element spaces and, for the fluid-structure problem in mind, we may employ elements that permit the fluid stress to be discontinuous across the structure. Because anisotropic triangles are employed we focus on their inf-sup stability, and since elements with discontinuous pressures are convenient to use we test them in this chapter. We actually show that their use with anisotropic triangles is limited and that mixed elements with continuous pressure perform much better. The extensive study of the mixed element with discontinuous pressures is presented in the third appendix. This work has been done in collaboration with Alessandro Veneziani.

We then draw our conclusions with considerations on possible future works.

Four appendices are attached. The first appendix has extended numerical tests for the first chapter. The second appendix contains numerical results on the use of a Lagrange multiplier for imposing Dirichlet boundary conditions for a two-dimensional incompressible steady Stokes problem. The third appendix is a complement of Chapter 3, which provides extended results of the finite element pairs studied in Chapter 3, but we also add new results on the two mixed finite element schemes with discontinuous pressures used in Chapter 4. This work has been done in collaboration with Franco Brezzi. The last appendix are notes related to the finite element implementation.

CHAPTER 2

A study on immersed 1D finite element methods

2.1. Introduction

Increasingly enhanced computer performances allow nowadays to tackle very large fluid-structure interaction problems, and state of the art examples, such as parachutes, wind turbines, or biomechanics applications, are now the object of active research (see, e.g., [**88**]). Furthermore, problems with very large structural deformations are still open to major improvements. In particular, a promising class of methods for such a type of problems belongs to so-called *immersed boundary* approaches. Many variants of this category of techniques have been proposed in the literature under several names, such as immersed boundary methods, unfitted and embedded methods, fictitious domain methods, etc.

Accordingly, the goal of the present work is to give highlights of some fundamental issues of immersed approaches by studying a simple 1D problem within the finite element method. In particular, we study some original approaches dating back to the 70-90's and a more recent one based on the extended finite element method, able to cure some issues of the original methods. For the latter method, we also focus on the issues that may be encountered in higher dimensions, as well as on possible solutions.

We consider problems involving multiple materials, and hence characterized by the presence of an interface, on which constraints have to be imposed. For instance, fluid-structure interaction situations belong to this category of problems, where velocity and stress continuities have to be imposed at the fluid-structure interface. From the numerical standpoint, two different approaches may be considered, the first one with a mesh fitting the interface, and the second one with a mesh not fitting the interface. The latter approach, named *unfitted* or *embedded*, has the advantage of enabling the use of meshes independent of the geometry, and it is the focus of the present chapter.

The present problem is also referred in the literature as an *elliptic interface problem*. Typically, solutions of elliptic interface problems are not smooth over the whole domain, but they are smooth away from the interface (see, e.g., [**64**], [**66**], and [**77**]). Earliest error estimates can be traced back to 1970 with the work of Babŭska (see [**10**]) in which the author provided a method based on a penalty approach. An almost optimal order of convergence is recovered for piecewise linear elements in the H^1-norm, more precisely $\mathcal{O}(h^{3/4})$. In [**14**], Barrett et al. proposed to enrich the finite element space on elements cut by the interface and to enforce weakly the continuity constraint using a penalty approach. They proved the optimal error estimate in the H^1-norm but the estimate in the L^2-norm is still suboptimal, i.e., $\mathcal{O}(h^{3/2})$. However, these authors show that the optimal error in the L^2-norm can be recovered far away of the interface. In [**54**] a similar method is proposed using the Nitsche method, instead of the penalty method, and the optimal error estimate is obtained in both H^1- and L^2-norms. In [**68**], the finite element space is not enriched, but a constraint on the mesh around the interface is added. The constraint consists in defining a "resolution" of the interface by the mesh, and it has to be at least of $\mathcal{O}(h^2)$ for piecewise linear elements such that the optimal rate of convergence for the L^2- and H^1-norms can be attained. However, the development of methods for elliptic interface problems differs from the development of fictitious methods for fluid-structure interaction problems, even if many similarities between the various approaches may be portrayed. In the present chapter we consider methods proposed in the literature for fluid-structure interaction problems.

In this context, we discuss four possible schemes: i) a *one-field Fictitious Domain method*; ii) a *continuously extended two-field Fictitious Domain method with Boundary Lagrange Multipliers*; iii) *a continuously extended two-field Fictitious Domain method with Distributed Lagrange Multipliers*; iv) *a discontinuously extended Fictitious Domain method with boundary Lagrange* *multipliers*, named herein two-field Discontinuous Fictitious Domain. In the following, we briefly discuss the four methods.

The *one-field Fictitious Domain method* (shortly, *one-field FD*) is inspired by the Immersed Boundary method, proposed by Peskin in the 70's (see [**81**] and references therein), and it is based on rewriting the problem as a function of a single field defined on the global domain, which is the union of the fluid and the solid domains. In general, the fluid model is extended over the solid domain, and the solid problem acts as a constraint on the fluid extended domain. It follows that the value of the global fluid field naturally describes the fluid in the fluid domain and the solid in the solid region. Since we deal with one field over the whole domain, the continuity at the interface is automatically satisfied, while a discontinuity in the gradient of the global fluid field may occur, with important implications for numerical methods.

The *continuously extended two-field Fictitious Domain method with Boundary Lagrange Multipliers* (shortly, *two-field FD/BLM*) is inspired by the original approach proposed by Glowinski in the 90's (see [**52**] and references therein). The method formalizes the problem with two fields: the global fluid and the solid. The global fluid field is defined on the global domain, such that it describes the fluid in the fluid domain and it is non-physical (fictitious) in the solid domain. The continuity between the two fields at the interface is enforced with a boundary Lagrange multiplier, that may introduce a discontinuity in their gradients between the physical fluid domain and the non-physical fluid region. Indeed, the Lagrange multiplier represents the jump in the gradient between the physical and the non-physical fluid domains.

The *continuously extended two-field Fictitious Domain method with distributed Lagrange multipliers* (shortly, *two-field FD/DLM*) is also described in [**52**] and is based again on two fields, as the previous method, but here the fictitious fluid and the solid fields are constrained to match in the solid domain with a distributed Lagrange multiplier. However, similarly to what happens with the two techniques previously described, a discontinuity in the gradient is introduced in the global fluid field between the physical fluid domain and the non-physical fluid region. Indeed, the distributed Lagrange multiplier imposes that the non-physical fluid behaves as the solid, thus imposing a jump at the interface.

The *discontinuously extended Fictitious Domain method with boundary Lagrange multipliers* (shortly, *two-field DFD/BLM*), inspired by the extended finite element method, has been proposed in [**48**]. The method is a two-field problem, where the fluid is extended in the fictitious domain by zero, and thus is based on the introduction of a strong discontinuity at the interface between the physical fluid and the fictitious fluid. As a consequence the method differs from all three methods previously described, which are characterized by a continuous global fluid field. Since it is a two-field method we have to enforce the continuity between the two fields at the interface. This operation is performed with a boundary Lagrange multiplier.

In this work, we propose a qualitative and quantitative analysis of the four previously mentioned techniques within the framework of the finite element method. For each scheme we present a variational formulation and its finite element approximation. The focus is on the discrete schemes and their performance. In particular, the variational method is presented formally, also if without any rigorous mathematical analysis, and it serves as a justification of the proposed algorithms. We aim at studying a simple model reproducing the typical characteristics of a fluid-structure problem, that is, a problem with continuity of the primal fields and with a possible discontinuity in the gradient at the interface. In fact, we focus on a steady Poisson problem defined on 1D domains with two different materials, where one surrounds the other; the problem under consideration requires that the continuity of the primal fields and of their fluxes is maintained at the interface. The main reasons for studying primarily a 1D problem are to provide easy and comprehensive formulations of the various methods and to analyze features of the methods that are already distinctive in 1D; however, practical implications for extensions to higher dimensions are identified and discussed as well.

We perform numerical tests to analyze the convergence properties in the L^2-norm, in the H^1-norm, and in the H^1-norm far away from the interface, of the four methods with different mesh refinement strategies and various material parameters. In particular, we show that, using linear finite elements, the one-field FD, two-field FD/BLM, and two-field FD/DLM methods are only first-order accurate, while the two-field DFD/BLM method is second-order accurate. We also point out the importance of quadrature over elements cut by the interface, since it is directly related to computational efficiency. As mentioned above, the chapter is then completed by a discussion on critical problems in higher dimensions, in particular about the imposition of the continuity constraint. The main interest in this respect is in the construction of second order accurate schemes for the approximation of interface problems with non fitting meshes.

Before proceeding with the core of the chapter, we wish to emphasize that we do not discuss here other second-order accurate approaches, such as the Fat Boundary method (see [**74**] and [**19**] for an analysis with a similar 1D problem) and the Immersed Interface method (see [**69**]). The Fat Boundary method uses an iterative Dirichlet/Neumann domain decomposition type of approach, while the Immersed Interface method modifies locally (i.e., on elements crossed by the interface) the shape functions such that they represent the interface constraints, introducing physical parameters in the definition of the shape functions. We therefore believe that these methods do not fit within our comparative study.

Moreover, we highlight that a Poisson problem similar to the one treated in the present chapter has been used within the framework of the spectral element method in [**94**]. In particular, Vos et al. investigated the two-field FD/DLM method, the Finite Cell method (see [**78**]) with boundary Lagrange multipliers, the Fat Boundary method, and a modified formulation of the Fat Boundary method with boundary Lagrange multipliers. We note that the Finite Cell method shares similarities with the two-field DFD/BLM method we consider herein, since the physical parameter for the global fluid is set to a very small value in the solid domain. With this chapter, we aim at providing

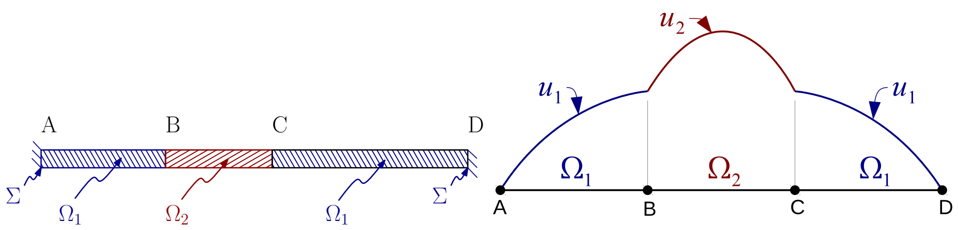

(a) Geometry of the problem.

(b) Analytical solution for a uniform load, showing a kink at the interface.

FIGURE 2.1. A two material 1D Poisson framework.

a similar study of various fictitious domain methods with traditional finite elements, and we believe that such a study highlights some fundamental issues that one has to take into account to develop this type of methods.

2.2. Model problem

We consider a Poisson problem characterized by two distinct materials, such that at the interface only continuity of the primal fields and of the corresponding fluxes have to be guaranteed.

As described in Fig. 2.1, Material 1 and Material 2 are defined on Ω_1 and Ω_2, respectively, with $\Omega_1 =]A, B[\cup]C, D[$ and $\Omega_2 =]B, C[$. We denote the interface between Ω_1 and Ω_2 by Γ (i.e., $\Gamma = \{B, C\}$). The global domain Ω is the union of Ω_1, Ω_2, and Γ, that is $\Omega =]A, D[$. External boundaries (i.e., $\partial\Omega = \{A, D\}$) are denoted by Σ.

In the following we introduce classical functional spaces that will be used in the rest of the chapter. In particular, $L^2(\Omega)$ is the space of square integrable functions on Ω, $H^1(\Omega)$ is the space of functions defined on Ω that belong to $L^2(\Omega)$ together with their first derivative, and $H^1_0(\Omega)$ the space of functions belonging to $H^1(\Omega)$ and vanishing on $\partial\Omega$.

The strong formulation for the described problem can be written as follows:

Find *two* functions $u_1 : \Omega_1 \to \mathbb{R}$ and $u_2 : \Omega_2 \to \mathbb{R}$ smooth enough such that

$$\begin{cases} -(\alpha_1 u_1')' = f_1 & \text{on } \Omega_1, \\ -(\alpha_2 u_2')' = f_2 & \text{on } \Omega_2, \\ u_{1|\Gamma} = u_{2|\Gamma}, & \\ (\alpha_1 u_1')_{|\Gamma} = (\alpha_2 u_2')_{|\Gamma}, & \\ u_{1|\Sigma} = 0, & \end{cases} \tag{2.1}$$

where $\alpha_1 \geq \bar{\alpha} > 0$, $\alpha_2 \geq \bar{\alpha} > 0$, f_1, and f_2, are given regular functions, and $u_{|\Gamma}$ is the restriction of u on Γ.

REMARK 1. *In Problem* (2.1)*, we consider for simplicity homogeneous Dirichlet boundary conditions on* Σ *but other boundary conditions can be considered as well.*

The standard weak formulation corresponding to Problem (2.1) can be readily obtained as:

Find $u \in H_0^1(\Omega)$ such that

$$\int_\Omega \alpha u' v' \mathrm{d}x = \int_\Omega f v \mathrm{d}x \qquad \forall v \in H_0^1(\Omega), \tag{2.2}$$

where

$$\alpha = \begin{cases} \alpha_1 & \text{on } \Omega_1 \\ \alpha_2 & \text{on } \Omega_2 \end{cases}, \quad \text{and } f = \begin{cases} f_1 & \text{on } \Omega_1 \\ f_2 & \text{on } \Omega_2 \end{cases}.$$

We may also split the one-field Problem (2.2) into:

Find $(u_1, u_2) \in W = \{(v_1, v_2) \in H^1(\Omega_1) \times H^1(\Omega_2);\ \text{with } v_{1|\Sigma} = 0 \text{ and } v_{1|\Gamma} = v_{2|\Gamma}\}$ such that

$$\int_{\Omega_1} \alpha_1 u_1' v_1' \mathrm{d}x + \int_{\Omega_2} \alpha_2 u_2' v_2' \mathrm{d}x - \int_{\Omega_1} f_1 v_1 \mathrm{d}x - \int_{\Omega_2} f_2 v_2 \mathrm{d}x = 0 \tag{2.3}$$

$\forall (v_1, v_2) \in W$.

Remark 2. *A discretization with finite elements of Problem* (2.3) *requires two partitions, one for* Ω_1 *and another one for* Ω_2*. In 1D this implies that the problem is fitted, since the partitions share common nodes at their interfaces. However, in higher dimensions, following the denomination of* [**56**]*, we distinguish two interface fitted cases: matching and non-matching. We say that an interface fitted problem is matching when all nodes on the interface are shared by both meshes. On the contrary, we say that an interface fitted problem is non-matching when the nodes lying on the boundary are not necessarily common to both meshes.*

Remark 3. *We add two comments on formulation* (2.3)*. Firstly, it is clear that if integrals are evaluated exactly, then the problem is equivalent to a standard Galerkin approach. However, when considering multidimensional problems, integration might be a difficult task and we may consider two different meshes for Material 1 and Material 2. Such a strategy results in a different method, that may converges, or may not, as it possibly loses consistency. Such issues are shown in numerical tests. Secondly, the reader may see the one-field FD method as a heuristic way for dealing with more complex problems such as those presented in, e.g.,* [**24**] *and* [**23**].

2.3. A one-field Fictitious Domain method

The one-field Fictitious Domain method (one-field FD) consists in rewriting Problem (2.3) in terms of a single continuous field u defined over the whole domain Ω, where $u_{|\Omega_1} = u_1$ and $u_{|\Omega_2} = u_2$, with $u_{|\Omega_i}$ denoting the restriction of u on Ω_i. Since we deal with a single continuous field u, the continuity constraint at the interface is automatically satisfied, while the continuity of the flux still needs to be enforced.

2.3.1. Continuum formulation

The strong formulation for the one-field Fictitious Domain problem can be written as follows:

Find *one* function $u : \Omega \to \mathbb{R}$ with $u_{|\Sigma} = 0$ such that

$$
(2.4) \qquad \begin{cases} -(\alpha u')' - f = 0 & \text{on } \Omega, \\ [\![\alpha u']\!]_\Gamma = 0, \end{cases}
$$

where we split α and f defined in Problem (2.2) such that

$$
\alpha = \begin{cases} \alpha_1 & \text{on } \Omega_1 \\ (\alpha_2 - \alpha_f) + \alpha_f & \text{on } \Omega_2 \end{cases},
$$

with α_f chosen such that $\alpha_f \geq \bar{\alpha} > 0$, and

$$
f = \begin{cases} f_1 & \text{on } \Omega_1 \\ (f_2 - f_f) + f_f & \text{on } \Omega_2 \end{cases}.
$$

The symbol $[\![\cdot]\!]_\Gamma$ denotes the jump on Γ.

Remark 4. *Since we consider an extension of Material 1 over Ω_2 we denote Material 1 over the whole domain Ω as* extended *(thus the subscript e) and the non-physical part (i.e., the part on Ω_2) as* fictitious *(thus the subscript f). These notations are used hereafter.*

Setting

$$
(2.5) \qquad \alpha_e = \begin{cases} \alpha_1 & \text{on } \Omega_1 \\ \alpha_f & \text{on } \Omega_2 \end{cases}, \quad \text{and} \quad f_e = \begin{cases} f_1 & \text{on } \Omega_1 \\ f_f & \text{on } \Omega_2 \end{cases},
$$

the weak formulation for Problem (2.4) can be readily obtained as:

Find *one* function $u \in H_0^1(\Omega)$ such that

$$
(2.6) \qquad \left\{ \begin{aligned} &\int_\Omega \alpha_e u' v' \mathrm{d}x - \int_\Omega f_e v \mathrm{d}x + \int_{\Omega_2} (\alpha_2 - \alpha_f) u' v' \mathrm{d}x \\ &\quad - \int_{\Omega_2} (f_2 - f_f) v \mathrm{d}x = 0, \end{aligned} \right.
$$

$\forall v \in H_0^1(\Omega)$.

It is clear that Problem (2.6) is equivalent to Problem (2.3) in the sense that $u_{|\Omega_1} = u_1$ and $u_{|\Omega_2} = u_2$. Moreover in Problem (2.6) we look for

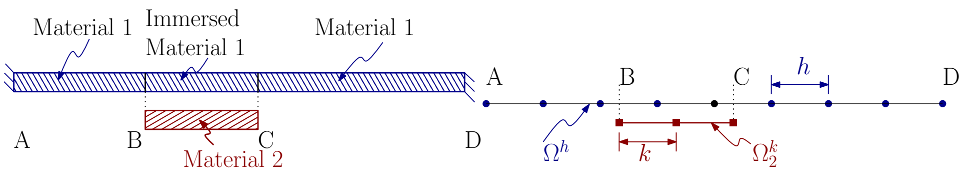

(a) An embedded domain strategy. (b) an unfitted mesh strategy.

FIGURE 2.2. An embedded domain method.

a function $u \in H_0^1(\Omega)$, thus satisfying automatically the continuity of the primal field on Γ. The continuity of the flux on Γ is instead naturally enforced in the weak formulation by continuity of the test function; see also [**29**], [**30**], and [**89**].

2.3.2. Discrete formulation

As discussed in Remark 2, we construct meshes with respect to the domain of integration for the integrals involved in the problem formulation. In Problem (2.6) integrals are defined on Ω and Ω_2, and, accordingly, we construct partitions for such domains. We consider Ω^h and Ω_2^k as partitions for Ω and Ω_2, respectively, where h and k are the sizes of the largest element in each partition (see Fig. 2(b)).

Given a finite-dimensional space $V^h \subset H_0^1(\Omega)$, the discrete formulation for Problem (2.6) can be readily obtained as:

Find $u^h \in V^h$ such that

$$\left\{ \begin{aligned} &\int_{\Omega^h} \alpha_e (u^h)'(v^h)'\mathrm{d}x + \int_{\Omega_2^k} (\alpha_2 - \alpha_f)(u^h)'(v^h)'\mathrm{d}x = \\ &\qquad \int_{\Omega^h} f_e v^h \mathrm{d}x + \int_{\Omega_2^k} (f_2 - f_f) v^h \mathrm{d}x \end{aligned} \right. \tag{2.7}$$

$\forall v^h \in V^h$.

Given the following approximation

$$u^h(x) = \mathbf{N}(x)\hat{\mathbf{u}},$$

with $\mathbf{N}(x)$ being standard piecewise linear shape functions defined on Ω^h and $\hat{\mathbf{u}}$ the primal field nodal value vector, the algebraic formulation corresponding

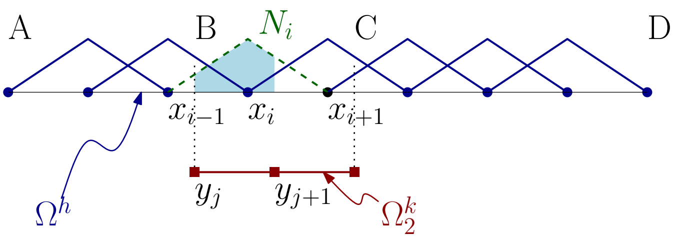

FIGURE 2.3. Quadrature issue on elements of Ω_2^k for shape functions with support on a partition for Ω. If we consider the shape function N_i (defined on a partition of Ω with support on $[x_{i-1}, x_{i+1}]$) admitting a kink on x_i in an element of a partition for Ω_2 ($K_j = [y_j, y_{j+1}]$), an exact integration on K_j requires to integrate on two sub-elements: $[y_j, x_i]$ and $[x_i, y_{j+1}]$. The blue zone corresponds to the integral of N_i on $[y_j, y_{j+1}]$.

to Problem (2.7) reads:

$$\mathbf{A}\hat{\mathbf{u}} = \mathbf{b}, \tag{2.8}$$

where

$$\begin{cases} \mathbf{A}_{|ij} = \displaystyle\int_{\Omega^h} \alpha_e N_i' N_j' \mathrm{d}x + \int_{\Omega_2^k} (\alpha_2 - \alpha_f) N_i' N_j' \mathrm{d}x, \\ \mathbf{b}_{|i} = \displaystyle\int_{\Omega^h} f_e N_i \mathrm{d}x + \int_{\Omega_2^k} (f_2 - f_f) N_i \mathrm{d}x. \end{cases}$$

REMARK 5. *We note that in Equation* (2.8) *the evaluation of the integrals defined over Ω_2^k is not an easy task. In fact, the functions N_i are polynomials over the elements of Ω^h; and may not be necessarily global polynomials. They are in general piecewise polynomials, when they are considered with respect to the elements of the discretization Ω_2^k. As an example, we may consider the case presented in Fig. 2.3. From a practical point of view, the main issue is to integrate over sub-elements which may be not trivial in higher dimensions. We do not discuss in detail such an issue in the present chapter, but the interested reader is referred to, e.g.,* **[47]** *for a review on possible integration strategies.*

2.4. A continuously extended two-field Fictitious Domain method with boundary Lagrange multipliers

The one-field Fictitious Domain method, described in the previous section, was based on the introduction of a single field u defined over the whole domain Ω. On the contrary, the two-field Fictitious Domain method introduces an extended field for Material 1 over the whole domain Ω, which is fictitious on Ω_2.

In the corresponding discrete formulation we consider unfitted meshes discretizing two fields, and hence we may use a boundary Lagrange multiplier to weakly enforce continuity of the primal fields in both materials at the interface.

In order to obtain a formulation that is consistent with Problem (2.1) we introduce an extension of u_1 on Ω_2 that does not necessarily maintain continuity of the derivatives of the extended u_1 on Γ. As a consequence, we have to consider on which side of the interface (physical or fictitious) we impose continuity of the flux; for convenience, we hereafter denote by Γ_1 and Γ_2 the limit to Γ approached from Ω_1 and Ω_2, respectively.

2.4.1. Continuum formulation

The two-field Fictitious Domain formulation is then given by:

Find *two* functions $u_e : \Omega \to \mathbb{R}$ and $u_2 : \Omega_2 \to \mathbb{R}$, with $u_{e|\Sigma} = 0$, such that

$$\begin{cases} -(\alpha_e u_e')' = f_e & \text{on } \Omega, \\ -(\alpha_2 u_2')' + (\alpha_f u_e')' = f_2 - f_f & \text{on } \Omega_2, \\ u_{e|\Gamma} = u_{2|\Gamma}, & \\ (\alpha_1 u_e')_{|\Gamma_1} = (\alpha_2 u_2')_{|\Gamma_2}. & \end{cases} \tag{2.9}$$

The weak formulation for Problem (2.9) can be readily obtained as:

Find *two* functions $(u_e, u_2) \in E_\Gamma = \{(u_e, u_2) \in H_0^1(\Omega) \times H^1(\Omega_2);\ \text{with } u_{e|\Gamma} = u_{2|\Gamma}\}$ such that for all $(v_e, v_2) \in E_\Gamma$ we have

$$
\begin{aligned}
&\int_\Omega \alpha_e u_e' v_e' \mathrm{d}x + \int_{\Omega_2} \alpha_2 u_2' v_2' \mathrm{d}x - \int_{\Omega_2} \alpha_f u_e' v_2' \mathrm{d}x = \\
&\qquad \int_\Omega f_e v_e \mathrm{d}x + \int_{\Omega_2} (f_2 - f_f) v_2 \mathrm{d}x.
\end{aligned} \tag{2.10}
$$

Since the discrete space for the extended Material 1 field may not be interpolatory at the interface, we choose to enforce weakly with a boundary Lagrange multiplier the constraint $u_{e|\Gamma} = u_{2|\Gamma}$, giving rise to the two-field Fictitious Domain with Boundary Lagrange Multipliers (two-field FD/BLM).

Find *two* functions $u_e \in H_0^1(\Omega)$ and $u_2 \in H^1(\Omega_2)$, and the Lagrange multipliers $\lambda_B \in \mathbb{R}$ and $\lambda_C \in \mathbb{R}$ such that

$$
\begin{cases}
\displaystyle\int_\Omega \alpha_e u_e' v_e' \mathrm{d}x + \lambda_B v_e(B) - \lambda_C v_e(C) = \int_\Omega f_e v_e \mathrm{d}x \\
\displaystyle\int_{\Omega_2} \alpha_2 u_2' v_2' \mathrm{d}x - \int_{\Omega_2} \alpha_f u_e' v_2' \mathrm{d}x - \lambda_B v_2(B) \\
\qquad \displaystyle + \lambda_C v_2(C) = \int_{\Omega_2} (f_2 - f_f) v_2 \mathrm{d}x, \\
\xi_B (u_e(B) - u_2(B)) = 0, \\
\xi_C (u_e(C) - u_2(C)) = 0,
\end{cases} \tag{2.11}
$$

$\forall v_1 \in H_0^1(\Omega)$, $\forall v_2 \in H^1(\Omega_2)$, $\forall \xi_B \in \mathbb{R}$ and $\forall \xi_C \in \mathbb{R}$.

REMARK 6. *We point out that the space of the Lagrange multiplier corresponds to the trace of $H^1(\Omega)$ on Γ, i.e., $H^{-1/2}(\Gamma)$, the dual of $H^{1/2}(\Gamma)$ since $\Gamma \cap \partial\Omega = \emptyset$. In one-dimension, the trace of H^1 is $\mathbb{R}$. It can be shown that the Lagrange multipliers can be interpreted as the flux across the interface:*

$$
\lambda_C = -\alpha_2 u_2'(C) + \alpha_1 u_e'(C) \quad \text{and} \quad \lambda_B = -\alpha_2 u_2'(B) + \alpha_1 u_e'(B).
$$

By introducing a Lagrange multiplier we add a constraint to the system, resulting in a saddle point problem. In order for a saddle point problem to be well-posed an inf-sup condition has to be satisfied (see **[22]** *and references* *therein). At the discrete level, such an issue is a very difficult task. We discuss the problem in Section 2.8.*

2.4.2. Discrete formulation

As explained in Section 2.3.2 for the discrete formulation of the one-field FD method, we consider Ω^h and Ω_2^k to be partitions for Ω and Ω_2, respectively, with mesh sizes h and k. Given finite-dimensional spaces V^h and W^k such that $V^h \subset H_0^1(\Omega)$ and $W^k \subset H^1(\Omega_2)$, the discrete formulation for Problem (2.11) reads:

Find *two* functions $u_e^h \in V^h$ and $u_2^k \in W^k$, and Lagrange multipliers $\tilde{\lambda}_B \in \mathbb{R}$ and $\tilde{\lambda}_C \in \mathbb{R}$, such that

$$
\begin{cases}
\displaystyle\int_{\Omega^h} \alpha_e (u_e^h)'(v_e^h)'\mathrm{d}x + \tilde{\lambda}_B v_e^h(B) - \tilde{\lambda}_C v_e^h(C) = \int_{\Omega^h} f_e v_e^h \mathrm{d}x, \\
\displaystyle\int_{\Omega_2^k} \alpha_2 (u_2^k)'(v_2^k)'\mathrm{d}x - \int_{\Omega_2^k} \alpha_f (u_e^h)'(v_2^k)'\mathrm{d}x \\
\qquad\displaystyle - \tilde{\lambda}_B v_2^k(B) + \tilde{\lambda}_C v_2^k(C) = \int_{\Omega_2^k} (f_2 - f_1) v_2^k \mathrm{d}x \\
\xi_B(u_e^h(B) - u_2^k(B)) = 0, \\
\xi_C(u_e^h(C) - u_2^k(C)) = 0,
\end{cases}
\tag{2.12}
$$

$\forall v_e^h \in V^h$, $\forall v_2^k \in W^k$, $\forall \xi_B \in \mathbb{R}$ and $\forall \xi_C \in \mathbb{R}$.

Given the following approximations

$$
u_e^h(x) = \mathbf{N}(x)\hat{\mathbf{u}}_e, \qquad u_2^k(x) = \mathbf{M}(x)\hat{\mathbf{u}}_2,
$$

where $\mathbf{N}(x)$ and $\mathbf{M}(x)$ are standard piecewise linear shape functions, $\hat{\mathbf{u}}_e$ and $\hat{\mathbf{u}}_2$ are the primal field nodal value vectors, and $\hat{\boldsymbol{\lambda}} = \{\lambda_B, \lambda_C\}^\top$, the algebraic formulation corresponding to Problem (2.12) reads

$$
\begin{bmatrix} \mathbf{A}_e & \mathbf{0} & \mathbf{L}_e^\top \\ -\mathbf{A}_{e2} & \mathbf{A}_2 & -\mathbf{L}_2^\top \\ \mathbf{L}_e & -\mathbf{L}_2 & \mathbf{0} \end{bmatrix}
\begin{Bmatrix} \hat{\mathbf{u}}_e \\ \hat{\mathbf{u}}_2 \\ \hat{\boldsymbol{\lambda}} \end{Bmatrix}
=
\begin{Bmatrix} \mathbf{f}_h \\ \mathbf{f}_k \\ \mathbf{0} \end{Bmatrix}.
\tag{2.13}
$$

The components of the system matrix are given by

$$\begin{cases} \mathbf{A}_{e|ij} = \displaystyle\int_{\Omega^h} \alpha_e N_i' N_j' \mathrm{d}x, \\ \mathbf{A}_{e2|ij} = \displaystyle\int_{\Omega_2^k} \alpha_f M_i' N_j' \mathrm{d}x, \\ \mathbf{A}_{2|ij} = \displaystyle\int_{\Omega_2^k} \alpha_2 M_i' M_j' \mathrm{d}x, \\ \mathbf{L}_{e|ij} = (\delta_i N_j)_{|\Gamma}, \\ \mathbf{L}_{2|ij} = (\delta_i M_j)_{|\Gamma}, \end{cases}$$

where $\delta_{1|B} = 1$, $\delta_{1|C} = 0$, $\delta_{2|B} = 0$, $\delta_{2|C} = 1$, and those of the right hand side by

$$\begin{cases} \mathbf{f}_{h|i} = \displaystyle\int_{\Omega^h} f_e N_i \mathrm{d}x, \\ \mathbf{f}_{k|i} = \displaystyle\int_{\Omega_2^k} (f_2 - f_f) M_i \mathrm{d}x. \end{cases}$$

REMARK 7. *In system* (2.13) *the terms* $\mathbf{A}_{e2}$ *is difficult to compute since the functions* N_i *are not defined on* Ω_2^k *but on* Ω^h *(see Remark 5 for a discussion on the implementation).*

2.5. A continuously extended two-field Fictitious Domain method with distributed Lagrange multipliers

In the two-field Fictitious Domain method, described in Section 2.4, we considered two fields u_e and u_2, where u_e was u_1 extended continuously over Ω_2. The coupling between u_e and u_2 at the interface was enforced with a boundary Lagrange multiplier. Since u_e is fictitious on Ω_2 (i.e., it has no physical meaning) we may constrain the extension of u_1 on Ω_2 such that $u_{e|\Omega_2} = u_2$ (see **[52]**). Since the nodes of the meshes for Ω_1 and Ω_2 are not necessarily common to both meshes, we may choose to enforce weakly the constraint $u_{e|\Omega_2} = u_2$ with a distributed Lagrange multiplier, giving rise to the two-field Fictitious Domain with Distributed Lagrange Multipliers (two-field FD/DLM).

2.5.1. Continuum formulation

Analogously to the case of the two-field FD/BLM method, the weak formulation for the two-field Fictitious Domain with a strong enforcement of the constraint $u_{e|\Omega_2} = u_2$ is given by:

Find $(u_e, u_2) \in E_{\Omega_2} = \{(u_e, u_2) \in H_0^1(\Omega) \times H^1(\Omega_2);\ \text{with } u_{e|\Omega_2} = u_2\}$ such that

$$\int_\Omega \alpha_e u_e' v_e' \mathrm{d}x + \int_{\Omega_2} \alpha_2 u_2' v_2' \mathrm{d}x - \int_{\Omega_2} \alpha_f u_e' v_2' \mathrm{d}x = \int_\Omega f_e v_e \mathrm{d}x + \int_{\Omega_2} (f_2 - f_f) v_2 \mathrm{d}x, \tag{2.14}$$

$\forall (v_e, v_2) \in E_{\Omega_2}$.

Enforcing weakly the constraint $u_{e|\Omega_2} = u_2$, it follows that Problem (2.14) with distributed Lagrange multipliers reads:

Find *two* functions $u_e \in H_0^1(\Omega)$, $u_2 \in H^1(\Omega_2)$, and a Lagrange multiplier $\lambda \in L^2(\Omega_2)$ such that

$$\begin{cases} \displaystyle\int_\Omega \alpha_e u_e' v_e' \mathrm{d}x + \int_{\Omega_2} \lambda v_e \mathrm{d}x = \int_\Omega f_e v_e \mathrm{d}x, \\ \displaystyle\int_{\Omega_2} \alpha_2 u_2' v_2' \mathrm{d}x - \int_{\Omega_2} \alpha_f u_e' v_2' \mathrm{d}x - \int_{\Omega_2} \lambda v_2 \mathrm{d}x \\ \displaystyle\qquad = \int_{\Omega_2} (f_2 - f_f) v_2 \mathrm{d}x, \\ \displaystyle\int_{\Omega_2} \xi (u_e - u_2) \mathrm{d}x = 0, \end{cases} \tag{2.15}$$

$\forall v_e \in H_0^1(\Omega)$, $\forall v_2 \in H^1(\Omega_2)$, and $\forall \xi \in L^2(\Omega_2)$.

REMARK 8. *We note that the two-field FD/DLM method is asymmetric. It is possible to obtain a symmetric formulation by replacing u_e by u_2 in the second equation of (2.15), since they are equal on Ω_2. At the continuous level both formulations are identical, but that is not the case at the discrete level (see* **[6]** *for more details on the asymmetric formulation).*

2.5.2. Discrete formulation

As explained in Section 2.3.2 for the discrete formulation of the one-field FD method we consider Ω^h and Ω_2^k to be partitions for Ω and Ω_2, respectively, with mesh sizes h and k.

Given finite-dimensional spaces V^h and W^k such that $V^h \subset H_0^1(\Omega)$ and $W^k \subset H^1(\Omega_2)$, the discrete formulation of Problem (2.15) reads:

Find *two* functions $u_e^h \in V^h$, $u_2^k \in W^k$, and the Lagrange multiplier $\lambda^k \in W^k$ such that

$$
\begin{cases}
\displaystyle\int_{\Omega^h} \alpha_e (u_e^h)'(v_e^h)'\mathrm{d}x + \int_{\Omega_2^k} \lambda^k v_e^h \mathrm{d}x = \int_{\Omega^h} f_e v_e^h \mathrm{d}x, \\
\displaystyle\int_{\Omega_2^k} \alpha_2 (u_2^k)'(v_2^k)'\mathrm{d}x - \int_{\Omega_2^k} \alpha_f (u_e^h)'(v_2^k)'\mathrm{d}x \\
\qquad\displaystyle - \int_{\Omega_2^k} \lambda^k v_2^k \mathrm{d}x = \int_{\Omega_2^k} (f_2 - f_f) v_2^k \mathrm{d}x \\
\displaystyle\int_{\Omega_2^k} \xi_k (u_e^h - u_2^k)\mathrm{d}x = 0,
\end{cases}
\tag{2.16}
$$

$\forall v_e^h \in V^h$, $\forall v_2^k \in W^k$, and $\forall \xi_k \in W^k$.

Remark 9. *In Problem* (2.16)*, we choose to use continuous finite elements for the Lagrange multiplier. However, since the distributed Lagrange multiplier is only in* $L^2(\Omega_2)$ *we may use discontinuous finite elements, as well.*

Given the following approximations

$$
u_e^h(x) = \mathbf{N}(x)\hat{\mathbf{u}}_e, \qquad u_2^k(x) = \mathbf{M}(x)\hat{\mathbf{u}}_2, \qquad \lambda_k(x) = \mathbf{M}(x)\hat{\boldsymbol{\lambda}},
$$

where $\mathbf{N}(x)$ and $\mathbf{M}(x)$ are standard piecewise linear shape functions, $\hat{\mathbf{u}}_e$, $\hat{\mathbf{u}}_2$, and $\hat{\boldsymbol{\lambda}}$ are the primal field and Lagrange multiplier nodal value vectors, the algebraic formulation corresponding to Problem (2.16) reads

$$
\begin{bmatrix} \mathbf{A}_e & \mathbf{0} & \mathbf{L}_e^\top \\ -\mathbf{A}_{e2} & \mathbf{A}_2 & -\mathbf{L}_2^\top \\ \mathbf{L}_e & -\mathbf{L}_2 & \mathbf{0} \end{bmatrix}
\begin{Bmatrix} \hat{\mathbf{u}}_e \\ \hat{\mathbf{u}}_2 \\ \hat{\boldsymbol{\lambda}} \end{Bmatrix}
=
\begin{Bmatrix} \mathbf{f}_h \\ \mathbf{f}_k \\ \mathbf{0} \end{Bmatrix}.
\tag{2.17}
$$

The components of the system matrix are given by

$$\begin{cases} \mathbf{A}_{e|ij} = \displaystyle\int_{\Omega^h} \alpha_e N_i' N_j' \mathrm{d}x, \\ \mathbf{A}_{e2|ij} = \displaystyle\int_{\Omega_2^k} \alpha_f M_i' N_j' \mathrm{d}x, \\ \mathbf{A}_{2|ij} = \displaystyle\int_{\Omega_2^k} \alpha_2 M_i' M_j' \mathrm{d}x, \\ \mathbf{L}_{e|ij} = \displaystyle\int_{\Omega_2^k} M_i N_j \mathrm{d}x, \\ \mathbf{L}_{2|ij} = \displaystyle\int_{\Omega_2^k} M_i M_j \mathrm{d}x, \end{cases}$$

and those of the right hand side by

$$\begin{cases} \mathbf{f}_{h|i} = \displaystyle\int_{\Omega^h} f_e N_i \mathrm{d}x, \\ \mathbf{f}_{k|i} = \displaystyle\int_{\Omega_2^k} (f_2 - f_f) M_i \mathrm{d}x. \end{cases}$$

2.6. A discontinuously extended two-field Fictitious Domain method with boundary Lagrange multipliers

In all previously presented methods, an extension of Material 1 is constructed on Ω_2 such that the extended formulation is continuous over Ω. In the next approach we also consider a two-field method but we extend u_1 on Ω_2 such that $u_{e|\Omega_2} = 0$. Therefore, the extended u_1 is discontinuous over the interface. The continuity of the primary fields at the interface is enforced with a boundary Lagrange multiplier defined on the physical sides of Material 1. We define the obtained method as the discontinuously extended two-field Fictitious Domain method with boundary Lagrange multipliers (two-field DFD/BLM).

2.6.1. Continuum formulation

In the previously described methods we considered α_e and f_e given by Equation (2.5) with the condition that $\alpha_e \geq \bar{\alpha} > 0$.

Here we consider the following extension:

$$\alpha_e = \begin{cases} \alpha_1 & \text{on } \Omega_1 \\ \tilde{\alpha}_1 & \text{on } \Omega_2 \end{cases}, \qquad \text{and} \qquad f_e = \begin{cases} f_1 & \text{on } \Omega_1 \\ 0 & \text{on } \Omega_2 \end{cases}, \tag{2.18}$$

where $\tilde{\alpha}_1 \geq \bar{\alpha} > 0$.

Let us introduce the space of discontinuous u_e on Γ,

$$D = \{u_e \in L^2(\Omega);\ \text{with } u_{e|\Omega_1} \in H^1(\Omega_1),$$
$$u_{e|\Omega_2} \in H^1_0(\Omega_2),\ \text{and } u_{e|\Sigma} = 0\}.$$

Then, since u_e admits a discontinuity on Γ we have to consider on which side of Γ we impose the continuity constraint. A weak formulation for the two-field DFD/BLM technique is given by the following statement:

Find $(u_e, u_2) \in D_\Gamma = \{(u_e, u_2) \in D \times H^1(\Omega_2);\ \text{with } u_{e|\Gamma_1} = u_{2|\Gamma_2}\}$ such that

$$\int_\Omega \alpha_e u_e' v_e' \mathrm{d}x + \int_{\Omega_2} \alpha_2 u_2' v_2' \mathrm{d}x - \int_\Omega f_e v_e \mathrm{d}x - \int_{\Omega_2} f_2 v_2 \mathrm{d}x = 0, \tag{2.19}$$

$\forall (v_e, v_2) \in D_\Gamma$.

We note that using the definitions of α_e and f_e we recover Problem (2.3).

In the following discrete formulation, partitions for Ω and Ω_2 may not be fitted, and hence the standard shape functions defined on a partition of Ω may not be interpolatory on the interface. As a consequence, we choose to enforce weakly the constraint $u_{e|\Gamma_1} = u_{2|\Gamma_2}$. For this purpose a boundary Lagrange multiplier is here employed, obtaining the following weak formulation:

Find *two* functions $u_e \in D$, $u_2 \in H^1(\Omega_2)$, and Lagrange multipliers $\lambda_B \in \mathbb{R}$ and $\lambda_C \in \mathbb{R}$ such that

$$\begin{cases} \displaystyle\int_\Omega \alpha_e u_e' v_e' \mathrm{d}x + \lambda_B v_e(B_1) - \lambda_C v_e(C_1) \\ \qquad \displaystyle= \int_\Omega f_e v_e \mathrm{d}x, \\ \displaystyle\int_{\Omega_2} \alpha_2 u_2' v_2' \mathrm{d}x - \lambda_B v_2(B_2) + \lambda_C v_2(C_2) \\ \qquad \displaystyle= \int_{\Omega_2} f_2 v_2 \mathrm{d}x, \\ \xi_B(u_e(B_1) - u_2(B_2)) = 0, \\ \xi_C(u_e(C_1) - u_2(C_2)) = 0, \end{cases} \tag{2.20}$$

$\forall v_e \in D$, $\forall v_2 \in H^1(\Omega_2)$, and $\forall \xi_B \in \mathbb{R}$ and $\forall \xi_C \in \mathbb{R}$, whereby B_1 we mean B approached from Ω_1, etc.

2.6.2. Discrete formulation

As explained in Section 2.3.2 for the discrete formulation of the one-field FD method, we consider Ω^h and Ω_2^k to be partitions for Ω and Ω_2, respectively, with mesh sizes h and k. We also assume that Ω_2 contains at least one element of Ω^h. It implies that we associate with each Lagrange multiplier on B and C at least one degree of freedom in the fictitious domain (denoted "free" node), otherwise the system is overconstrained. This can be overcome considering the extended finite element method on elements crossed by the interface as presented, for instance, in **[38]**, such that the system has enough "free" nodes with respect to the number of Lagrange multipliers. We point out that all degrees of freedom of the field of Material 1 that are associated to elements without support on Ω_1 are eliminated from the linear system of equations. Moreover an extension of the DFD/DLM method to higher dimensions is not trivial due to locking issues, as further discussed in Section 2.8.

Given finite-dimensional spaces V^h and W^k such that $V^h \subset H_0^1(\Omega)$ and $W^k \subset H^1(\Omega_2)$, the discrete formulation of Problem (2.20) reads:

Find $u_e^h \in V^h_{|\Omega_1}$, $u_2^k \in W^k$, and Lagrange multipliers $\tilde{\lambda}_B \in \mathbb{R}$ and $\tilde{\lambda}_C \in \mathbb{R}$, such that

$$\begin{cases} \displaystyle\int_{\Omega^h} H_{\Omega_1} \alpha_e (u_e^h)'(v_e^h)'\mathrm{d}x + \tilde{\lambda}_B v_e^h(B) - \tilde{\lambda}_C v_e^h(C) \\ \qquad = \displaystyle\int_{\Omega^h} f_e v_e^h \mathrm{d}x, \\ \displaystyle\int_{\Omega_2^k} \alpha_2 (u_2^k)'(v_2^k)'\mathrm{d}x - \tilde{\lambda}_B v_2^k(B) + \tilde{\lambda}_C v_2^k(C) \\ \qquad = \displaystyle\int_{\Omega_2^k} f_2 v_2^k \mathrm{d}x, \\ \xi_B u_e^h(B) - \xi_B u_2^k(B) = 0, \\ \xi_C u_e^h(C) - \xi_C u_2^k(C) = 0, \end{cases} \tag{2.21}$$

$\forall v_e^h \in V^h_{|\Omega_1}$, $\forall v_2^k \in W^k$, $\forall \xi_B \in \mathbb{R}$ and $\forall \xi_C \in \mathbb{R}$,

where $H_{\Omega_1}(x)$ is the Heaviside function, that is 1 on Ω_1 and 0 otherwise. Given the following approximations

$$u_e^h(x) = \mathbf{N}(x)\hat{\mathbf{u}}_e, \qquad u_2^k(x) = \mathbf{M}(x)\hat{\mathbf{u}}_2,$$

where $\mathbf{N}(x)$ and $\mathbf{M}(x)$ are standard piecewise linear finite elements, $\hat{\mathbf{u}}_e$ and $\hat{\mathbf{u}}_2$ are the primal field nodal value vectors, and $\hat{\boldsymbol{\lambda}} = \{\lambda_B, \lambda_C\}^\top$, the algebraic formulation to Problem (2.21) reads

$$\begin{bmatrix} \mathbf{A}_e & \mathbf{0} & \mathbf{L}_e^\top \\ \mathbf{0} & \mathbf{A}_2 & -\mathbf{L}_2^\top \\ \mathbf{L}_e & -\mathbf{L}_2 & \mathbf{0} \end{bmatrix} \begin{Bmatrix} \hat{\mathbf{u}}_e \\ \hat{\mathbf{u}}_2 \\ \hat{\boldsymbol{\lambda}} \end{Bmatrix} = \begin{Bmatrix} \mathbf{f}_h \\ \mathbf{f}_k \\ \mathbf{0} \end{Bmatrix}. \tag{2.22}$$

The components of the system matrix are given by

$$\begin{cases} \mathbf{A}_{e|ij} = \displaystyle\int_{\Omega^h} \alpha_e N_i' N_j' \mathrm{d}x, \\ \mathbf{A}_{2|ij} = \displaystyle\int_{\Omega_2^k} \alpha_2 M_i' M_j' \mathrm{d}x, \\ \mathbf{L}_{e|ij} = (\delta_i N_j)_{|\Gamma}, \\ \mathbf{L}_{2|ij} = (\delta_i M_j)_{|\Gamma}, \end{cases}$$

where $\delta_{1|B} = 1$, $\delta_{1|C} = 0$, $\delta_{2|B} = 0$, $\delta_{2|C} = 1$, and those of the right hand side by

$$\begin{cases} \mathbf{f}_{h|i} = \displaystyle\int_{\Omega^h} f_e N_i \mathrm{d}x, \\ \mathbf{f}_{k|i} = \displaystyle\int_{\Omega_2^k} f_2 M_i \mathrm{d}x. \end{cases}$$

2.7. Numerical tests

To test the performance of the four different methods discussed in Sections 2.3-2.6, we study the model in Section 2.2, considering a h-refinement strategy with piecewise linear finite elements and different material parameters (see Table 2.1). Additional tests are performed with two more combinations of material parameters and they are given in A. The additional tests reported in A confirm the trends observed with the numerical tests of this section.

Material	Test 1	Test 2
α_1	1	4
α_2	4	1

TABLE 2.1. Material parameters definitions.

As discussed in Remark 5, many integrals involve terms that are not global polynomials on elements of the mesh of Ω_2, but are polynomials on sub-elements of the mesh of Ω_2 (as depicted in Fig. 2.3). As a consequence, we have to integrate exactly with 2 Gauss points[1] per sub-element (see again Fig. 2.3), and we denote this integration strategy as *exact* quadrature scheme. Also, since integration schemes over sub-elements may be expensive, we perform integration using a standard Gauss quadrature over the elements of all meshes (2 Gauss points per element in our test problems), and we denote this integration strategy as *approximated* quadrature scheme.

2.7.1. Test problems

For all methods we consider the following geometry: $A = 0$, $B = e$, $C = 1+\pi$, $D = 6$ (see Fig. 1(a) for a description of the geometry). Interfaces B and C are such that the problem remains unfitted for all refinement steps (see Table 2.2 and 2.3), and, to accomplish this goal easily, we select irrational numbers for B and C and rational numbers for A and D. The material parameters for Material 1 (α_1) and Material 2 (α_2) are chosen constant on $]A, B[\cup]C, D[$ and $]B, C[$, respectively, and we select constant loads $f_1 = 1$ on $]A, B[\cup]C, D[$ and $f_2 = 1$ on $]B, C[$. The extension of Material 1 for the one-field FD and two-field FD methods over Ω_2 is chosen such that $\alpha_f = \alpha_1$ and $f_f = f_1$. For the two-field DFD method α_e and f_e are defined in Equation (2.18).

The different set of material parameters are given in Table 2.1 with the corresponding analytical solutions reported in Fig. 2.4.

[1]Since the two-field FD/DLM method requires at least 2 Gauss points per element to integrate exactly integrals involving the distributed Lagrange multiplier, we choose to use a 2 Gauss-Legendre point rule for all integral terms for all methods

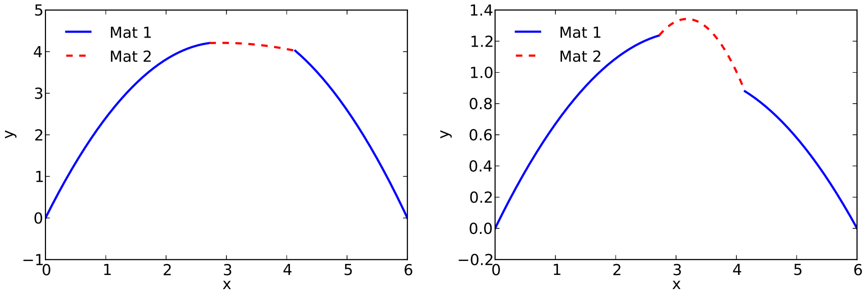

(a) Test 1. (b) Test 2.

FIGURE 2.4. Analytical solutions for the numerical test with $f_1 = 1$ on $]A, B[\cup]C, D[$, $f_2 = 1$ on $]B, C[$, for the different material parameters reported in Table 2.1.

All simulations are performed using piecewise linear finite elements to approximate all unknown fields, including the discrete distributed Lagrange multipliers which are defined on the mesh of Ω_2.

2.7.2. Refinement ratios

Recalling that h and k denote, respectively, the sizes of the largest element in Ω^h and Ω_2^k, we denote by $h_r = h/k$ the mesh ratio, by L the length of $]A, D[$ (i.e., Ω), and by L_2 the length of $]B, C[$ (i.e., Ω_2). We consider two uniform h-refinement strategies such that $h_r < 1$ (i.e., $h_r = L/L_2 \times 1/8 = 6/(1 + \pi - e) \times 1/8 \approx 1/2$, that is, h is "roughly" twice smaller than k) and $h_r > 1$ (i.e., $h_r = L/L_2 \times 1/2 = 6/(1+\pi-e) \times 1/2 \approx 2$, that is, h is "roughly" twice larger than k). Such mesh refinement strategies are presented for each mesh in Tables 2.2 and 2.3.

For the one-field FD with an exact quadrature scheme the choice of a partition for Ω_2 has no impact on the solution since integration is performed exactly. On the contrary, with the approximated quadrature scheme the integration error depends on the partition for Ω_2, and thus on the mesh ratio h_r. However, since the mesh ratio has no impact on the rate of convergence of the method with an exact quadrature scheme and that, with an approximated one, the mesh ratio has only an impact on the integration error, we pick only one refinement strategy (i.e., $h_r > 1$ presented in Table 2.2, that is the one that leads to the best quadrature). Such a choice implies that care

h/L	$1/24$	$1/48$	$1/96$	$1/192$	$1/368$	$1/768$	$1/1536$	$1/3072$
k/L_2	$1/12$	$1/24$	$1/48$	$1/96$	$1/192$	$1/368$	b1/768	$1/1536$

TABLE 2.2. Mesh refinement strategy for a mesh ratio $h_r \approx 2$.

h/L	$1/24$	$1/48$	$1/96$	$1/192$	$1/384$	$1/768$	$1/1536$	$1/3072$
k/L_2	$1/3$	$1/6$	$1/12$	$1/24$	$1/48$	$1/96$	$1/192$	$1/368$

TABLE 2.3. Mesh refinement strategy for a mesh ratio $h_r \approx 1/2$.

should be taken to generalize the results for different mesh ratios with an approximated quadrature scheme.

For two-field methods, boundary and distributed Lagrange multipliers are different since, for a 1D problem, a boundary Lagrange multiplier is defined on a set of discrete points and a distributed Lagrange multiplier on a segment. The boundary Lagrange multiplier is thus identically defined for every choice of meshes for Ω_2. Its definition is only affected by the choice of a mesh for Ω (because the evaluation of the shape functions $M(x)$ at the boundary of the domain Ω_2 is always 1, which is not the case for shape functions $N(x)$ at the boundary of the domain Ω_2). Thus, the convergence rate is not affected by a change in the mesh ratio. We therefore pick an arbitrary mesh ratio (i.e., $h_r > 1$ as presented in Table 2.2) for problems with boundary Lagrange multipliers. For distributed Lagrange multipliers we choose to use a mesh of Ω_2 with piecewise linear finite elements, and thus the method with distributed Lagrange multipliers depends on the mesh ratio h_r. We test the two-field FD/DLM method with both mesh ratios $h_r > 1$ and $h_r < 1$, as presented in Tables 2.2 and 2.3.

2.7.3. Error measurement

Since the one-field FD method involves a single field u_h, we use the relative error in L^2-norm, defined by

$$E_{0,\Omega} = \frac{\left(\int_\Omega (u - u_h)^2 \mathrm{d}x\right)^{\frac{1}{2}}}{\left(\int_\Omega u^2 \mathrm{d}x\right)^{\frac{1}{2}}} = \frac{||u - u_h||_{0,\Omega}}{||u||_{0,\Omega}}, \tag{2.23}$$

where u is the analytical solution of the problem over Ω.

In the same fashion, we define the relative H^1-seminorm by

$$E_{1,\Omega} = \frac{\left(\int_\Omega (u' - u_h')^2 \mathrm{d}x\right)^{\frac{1}{2}}}{\left(\int_\Omega (u')^2 \mathrm{d}x\right)^{\frac{1}{2}}} = \frac{|u' - u_h'|_{1,\Omega}}{|u'|_{1,\Omega}}. \tag{2.24}$$

We note that the H^1-seminorm is equivalent to the H^1-norm in virtue of the Poincaré-Friedrichs inequality.

In [**68**] it is pointed out that when computing the H^1-norm away from the interface the optimal convergence rate in the H^1-norm can be obtained, precisely when using the error measurement:

$$E_{1,\Omega\backslash\Gamma_\epsilon} \quad \text{with} \quad \Gamma_\epsilon = \{x \in \Omega : \mathrm{dist}(x, \Gamma) < \epsilon\}. \tag{2.25}$$

In the numerical tests we choose $\epsilon = h$. Such a choice is discussed in Remark 10

REMARK 10. *In* [**68**] *a constraint for the construction of the mesh is added. It is required that the mesh is "ϵ-resolved" near the interface, i.e., there must not be an element that overlaps Γ_ϵ. In that work, it is proved that for $\epsilon = \mathcal{O}(h^2)$ the method has the optimal rate of convergence in both L^2- and H^1-norms. However, in our numerical experiments the mesh is not ϵ-resolved for $\epsilon = \mathcal{O}(h^2)$ but it is for $\epsilon = \mathcal{O}(h)$. It justifies our choice of $\epsilon = h$. In the present numerical tests we show that we do not have the optimal rate of convergence for the $H^1(\Omega)$- and $L^2(\Omega)$-norms, at the exception of the DFD/BLM method, but we may attain it using the $H^1(\Omega\backslash\Gamma_\epsilon)$-norm.*

For two-field methods we only measure errors in physical domains (i.e., Ω_1 and Ω_2). Our error measurement (in L^2-norm) is given by

$$E_{0,\Omega} = \frac{\left(||u_1 - u_e^h||^2_{\Omega_1} + ||u_2 - u_2^k||^2_{\Omega_2}\right)^{\frac{1}{2}}}{\left(||u_1||^2_{\Omega_1} + ||u_2||^2_{\Omega_2}\right)^{\frac{1}{2}}}, \tag{2.26}$$

where $||\cdot||_\Omega$ is defined as in (2.23) and u_1 and u_2 are the analytical solutions of the problem over Ω_1 and Ω_2, respectively.

In the same fashion, the H^1-seminorm is defined by

$$E_{1,\Omega_1,\Omega_2} = \frac{\left(|u_1 - u_e^h|^2_{1,\Omega_1} + |u_2 - u_2^k|^2_{1,\Omega_2}\right)^{\frac{1}{2}}}{\left(|u_1|^2_{1,\Omega_1} + |u_2|^2_{1,\Omega_2}\right)^{\frac{1}{2}}}, \tag{2.27}$$

while our measurement in the $H^1(\Omega\backslash\Gamma_\epsilon)$-seminorm is given by

$$E_{1,\Omega_1\backslash\Gamma_\epsilon,\Omega_2}. \tag{2.28}$$

2.7.4. Results

In order to emphasize the impact of the quadrature schemes, we first present the results with an exact quadrature scheme and then with an approximated quadrature. Finally, we discuss the conditioning of the various methods.

2.7.4.1. *Finite elements with exact quadrature*

For the one-field FD

method we observe in Fig. 5(a) and Fig. 5(b) that the rates of convergence oscillate, but averagely a convergence of order 1 is attained in L^2-norm and of order 1/2 in H^1-norm. Instead, in the $H^1(\Omega\backslash\Gamma_\epsilon)$-seminorm a linear order of convergence is achieved. We recall that assuming an exact integration this method is equivalent to the standard Galerkin method.

Remark 11. *We can observe in Fig. 6(a) that the error $u - u_h$ at the interface propagates to the whole domain, preventing a possible optimal convergence rate in the L^2-norm away from the interface. On the contrary, for the H^1-norm, we can observe (see Fig. 6(b)) that the error in the derivatives clearly converges linearly away from the interface, even showing a superconvergence property at the middle of the elements not cut by the interface. Differently to $u - u_h$, the quantity $u' - u_h'$ does not appear to converge on the interface, but here the support of the large error values is limited to the elements crossed by the interface. It follows that the optimal rate of convergence would be obtained if the error is integrated only on elements not crossed by the interface. This example also shows that if the mesh is ϵ-resolved with $\epsilon = \mathcal{O}(h^2)$, then we may obtain the optimal rate of convergence in the H^1-norm for a smaller ϵ, i.e., $\epsilon < h$, as observed in* **[68]**.

For the two-field FD/BLM method, we also observe in Fig. 7(a) and Fig. 7(b) that the rates of convergence also oscillate but averagely the method has a convergence of order 1 in the L^2-norm and of order 1/2 in the H^1-norm. On the contrary to the one-field FD method, the error in the $H^1(\Omega\backslash\Gamma_\epsilon)$-norm appears to be optimal only with $\alpha_1/\alpha_2 < 1$ while the error for $\alpha_1/\alpha_2 > 1$ in the $H^1(\Omega\backslash\Gamma_\epsilon)$-norm is equivalent to the error in the H^1-norm. Indeed, the norm for the two-field problems is defined as a combination of the errors in both fields. Results from the one-field method show that the error is concentrated at the interface, and thus in case of a two-field problem the error on the interface is "transmitted" from the first field to the second field. It follows that a suboptimal $H^1(\Omega\backslash\Gamma_\epsilon)$ rate of convergence is obtained. In fact, further tests show that the $H^1(\Omega\backslash\Gamma_\epsilon)$ rate of convergence is optimal if the error is restricted to Ω_1 but not if it is restricted to Ω_2. Surprisingly, for $\alpha_1/\alpha_2 < 1$ the $H^1(\Omega\backslash\Gamma_\epsilon)$ convergence rate is almost optimal, indicating an almost optimal rate of convergence in the $H^1(\Omega_2)$-norm.

REMARK 12. *The two-field FD/BLM may be second-order accurate if u_1' is continuous over Ω, as described in* [**50**]. *But such a case is unlikely with our definition of the extension over the whole domain Ω of the load f_1. We note that in order to obtain an optimal method we may seek for an extension f_f on Ω_2 such that $u_e \in H^2(\Omega)$ (see for instance the work of* [**43**]*).*

For the two-field FD/DLM method we observe in Fig. 2.9 that for a mesh ratio $h_r \approx 1/2$ the method has a linear convergence behavior in L^2. This result is due to the poor approximation of the Lagrange multipliers. That issue also occurs for fitted meshes (see Remark 13). On the contrary, for a mesh ratio $h_r \approx 2$ the method converges with oscillatory rates of convergence, but averagely the rate of convergence is linear in L^2, as depicted in Fig. 2.8.In general, the H^1 convergence rate appears closer to 1/2 rather than 1, showing a suboptimal behavior. On the contrary, for the $H^1(\Omega\backslash\Gamma_\epsilon)$ rate of convergence, identical conclusions can be drawn from the two-field FD/BLM method.

Finally, the two-field DFD/BLM method is second-order accurate, as depicted in Fig. 2.10. We note that the error is slightly dependent of the material ratio.

To summarize, the fact that the first three methods are not second-order accurate is not surprising, since they are all characterized by a discontinuity in the gradient at the interface; as a consequence, their corresponding solutions are not in $H^2(\Omega)$ and the rate of convergence cannot be optimal. The solution depends on the position of the interface with respect to the mesh of Ω, which varies arbitrarily with a h-refinement, and hence the rates of convergence are not constant.However, results confirm that away from the interface the H^1 rate of convergence may be optimal, i.e., in the $H^1(\Omega\backslash\Gamma_\epsilon)$-norm. Comparing one-field and two-field methods, there is a clear advantage in using a one-field approach since the optimal $H^1(\Omega\backslash\Gamma_\epsilon)$ convergence rate is recovered on both Ω_1 and Ω_2. However, for two-field methods the optimal rate of convergence in the $H^1(\Omega\backslash\Gamma_\epsilon)$-norm is recovered only restricting it to Ω_1 but the rate of convergence is almost optimal when $\alpha_1/\alpha_2 < 1$, a case which represents a large class of applications. On the contrary to the previous methods, the two-field DFD method explicitly takes into account the discontinuity at the interface in the finite element space and thus it attains a second-order rate of convergence.

REMARK 13. *With fitted meshes all methods are second-order accurate, except the two-field FD/DLM method which is only first-order accurate with a mesh ratio strictly lower than 1. The fact that the methods are second-order accurate with fitted meshes results from our finite element basis that allows jumps in the gradient at vertices. In the case of the two-field FD/DLM method with fitted meshes and a mesh ratio strictly lower than 1, the method is not second-order accurate since the Lagrange multiplier space is not rich enough (see Fig. 2.11).*

2.7.4.2. *Finite elements with approximated quadrature*

The one-field FD method with approximate quadrature converges with a similar rate of convergence as with an exact quadrature scheme only if the material ratio α_1/α_2 is lower than one, as depicted in Fig. 5(c), while it simply does not converge otherwise, as depicted in Fig. 5(d). Another noticeable result is that the $H^1(\Omega\backslash\Gamma_\epsilon)$ rate of convergence is suboptimal with a rate of 1/2. For the one-field FD method the mesh ratio and the quadrature rule are a very important factor. Indeed, for a finer partition of Ω_2, or a more precise quadrature rule, the quadrature error is reduced and thus the method may converge even for a large material ratio α_1/α_2, since the method converges with an exact integration. Nevertheless, the relation between the quadrature rule and the material ratio remains unclear, and thus the approximated quadrature for the one-field FD method requires specific care.

The two-field FD/BLM and two-field FD/DLM methods with approximate quadrature converge for all cases with similar convergence rates as with an exact quadrature, as depicted for the FD/BLM method in Fig. 2.7, and for the FD/DLM method in Fig. 2.8 and Fig. 2.9. Such a result follows from the two-field structure of the methods, which implies that as long as the extended Material 1 may converge then the convergence for both fields is maintained. Similar results as with the exact integration cases are found for the errors in the $H^1(\Omega)$- and $H^1(\Omega\backslash\Gamma_\epsilon)$-seminorms.

The two-field DFD/BLM method loses its second order property in the L^2-norm and it appears to converge at most linearly, as depicted in Fig. 2.10. We show the importance of an exact quadrature for the two-field DFD/BLM method in another numerical test by integrating with a higher number of Gauss points on elements crossed by the interface. The results in Fig. 2.12 show that a clear quadratic rate of convergence is recovered with 400 Gauss points per element crossed by the interface. Notice that when using approximated quadrature the $H^1(\Omega\backslash\Gamma_\epsilon)$ convergence rate remains optimal and it is almost optimal in the $H^1(\Omega)$-seminorm.

The integration scheme is an important point to be taken into account since it influences the cost of the method. A first-order accurate method is interesting if it is much faster in terms of computational time than a second-order accurate method. We might therefore use a standard integration scheme with the first-order accurate methods since their convergence rates are not drastically changed with respect to an exact integration scheme (with special care for the one-field FD method). On the contrary, for the two-field DFD method it is mandatory to integrate exactly or a drastic loss

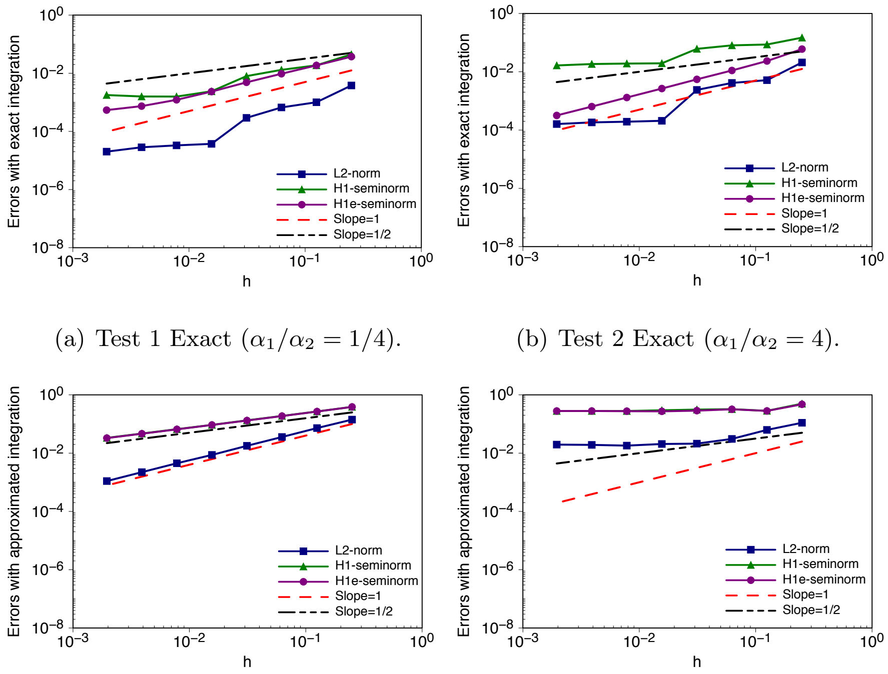

(a) Test 1 Exact ($\alpha_1/\alpha_2 = 1/4$).
(b) Test 2 Exact ($\alpha_1/\alpha_2 = 4$).
(c) Test 1 Approximated ($\alpha_1/\alpha_2 = 1/4$).
(d) Test 2 Approximated ($\alpha_1/\alpha_2 = 4$).

FIGURE 2.5. The one-field FD method.

in the rate of convergence in the L^2-norm has to be expected, but approximated integration appears to have a small impact on the H^1 and $H^1(\Omega\backslash\Gamma_\epsilon)$ rates of convergence.

2.7.4.3. *Conditioning*

The condition numbers for the various methods are presented in Fig. 2.13. Clearly, the one-field method as well as the methods using boundary Lagrange multipliers show a standard $\mathcal{O}(h^{-2})$ conditioning. Instead, the method using the distributed Lagrange multipliers shows a much higher conditioning of order $\mathcal{O}(h^{-4})$; this result appears to be independent of the mesh ratio.

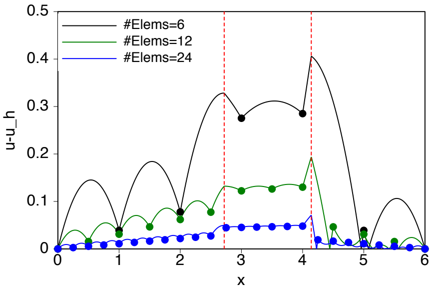

(a) Error $u - u_h$

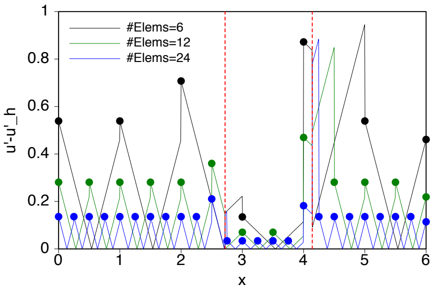

(b) Error $u' - u'_h$

FIGURE 2.6. Errors for Test 1 ($\alpha_1/\alpha_2 = 1/4$) with the one-field FD method with exact quadrature (i.e., standard Galerkin). The dots symbolize the position of the nodes, while the red lines the position of the interface.

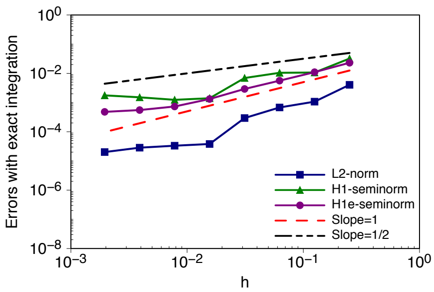

(a) Test 1 Exact ($\alpha_1/\alpha_2 = 1/4$).

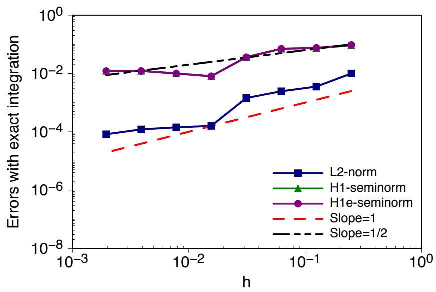

(b) Test 2 Exact ($\alpha_1/\alpha_2 = 4$).

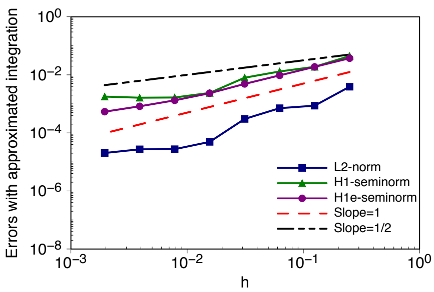

(c) Test 1 Approximated ($\alpha_1/\alpha_2 = 1/4$).

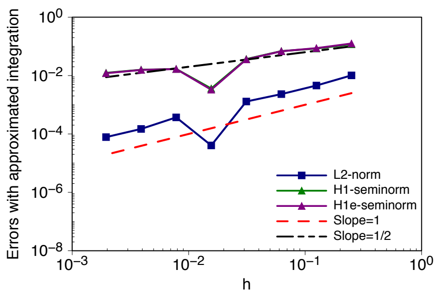

(d) Test 2 Approximated ($\alpha_1/\alpha_2 = 4$).

FIGURE 2.7. The two-field FD/BLM method.

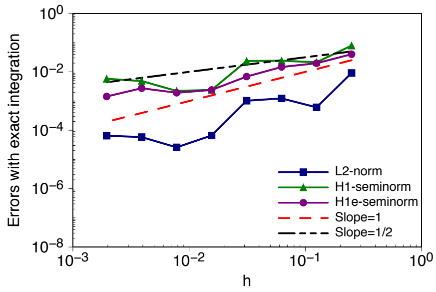

(a) Test 1 Exact ($\alpha_1/\alpha_2 = 1/4$).

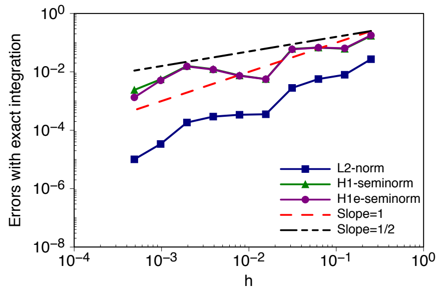

(b) Test 2 Exact ($\alpha_1/\alpha_2 = 4$).

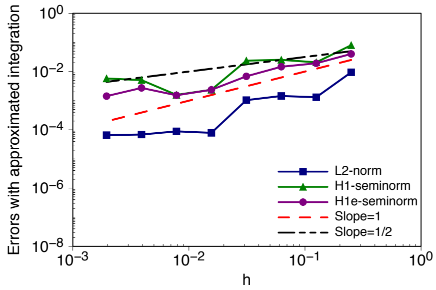

(c) Test 1 Approximated ($\alpha_1/\alpha_2 = 1/4$).

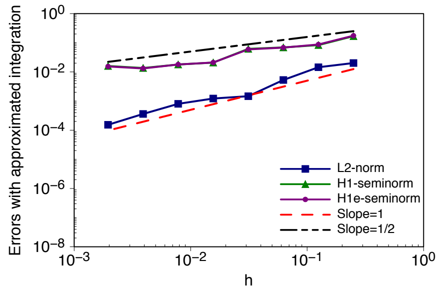

(d) Test 2 Approximated ($\alpha_1/\alpha_2 = 4$).

FIGURE 2.8. The two-field FD/DLM method with $h_r \approx 2$.

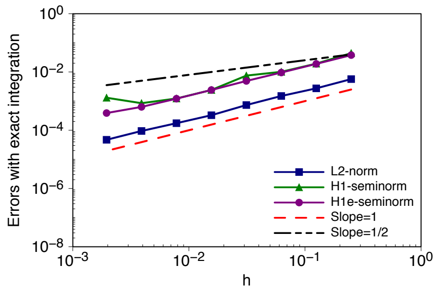

(a) Test 1 Exact ($\alpha_1/\alpha_2 = 1/4$).

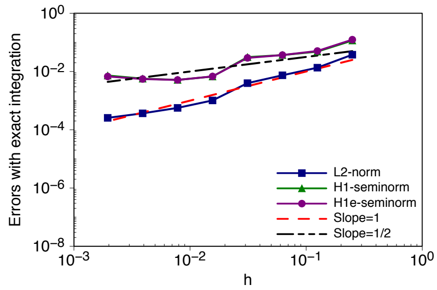

(b) Test 2 Exact ($\alpha_1/\alpha_2 = 4$).

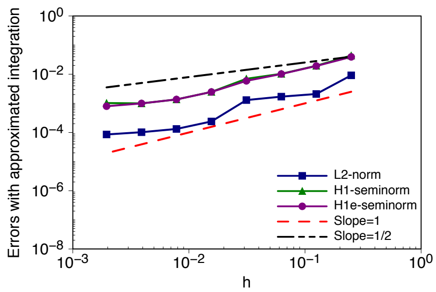

(c) Test 1 Approximated ($\alpha_1/\alpha_2 = 1/4$).

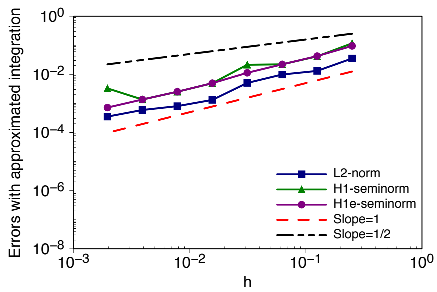

(d) Test 2 Approximated ($\alpha_1/\alpha_2 = 4$).

FIGURE 2.9. The two-field FD/DLM method with $h_r \approx 1/2$.

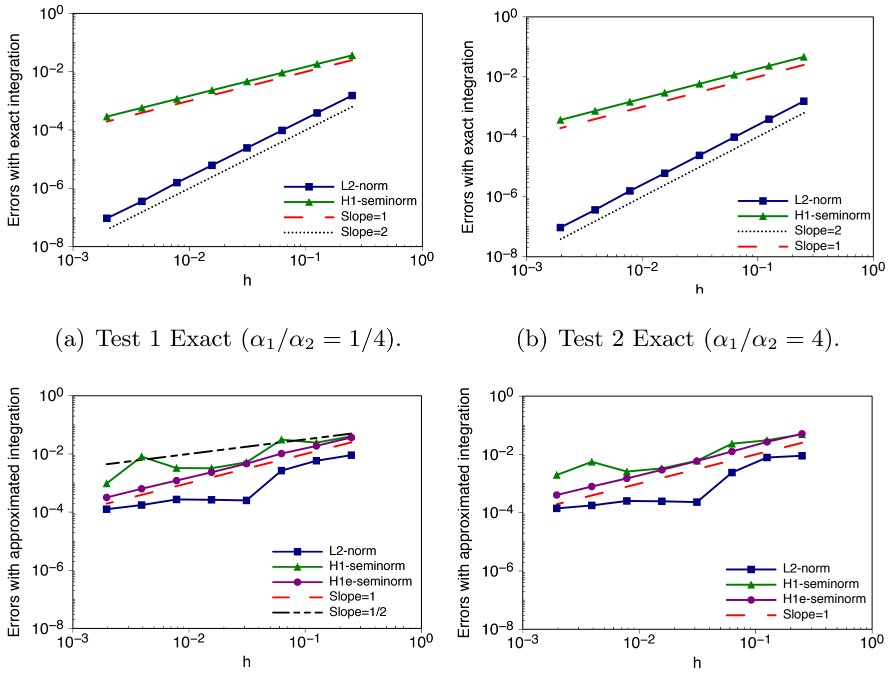

(a) Test 1 Exact ($\alpha_1/\alpha_2 = 1/4$). (b) Test 2 Exact ($\alpha_1/\alpha_2 = 4$).

(c) Test 1 Approximated ($\alpha_1/\alpha_2 = 1/4$). (d) Test 2 Approximated ($\alpha_1/\alpha_2 = 4$).

FIGURE 2.10. The two-field DFD/BLM method.

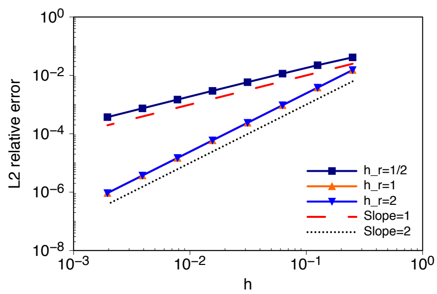

FIGURE 2.11. Convergence rates of the two-field FD/DLM problem for a fitted case and different mesh ratios, with A=0, B=3, C=4.5, D=6. The coefficients are given by $\alpha_1 = 1$ and $\alpha_2 = 4$ (similar results can be obtained with different material ratios). It can be noticed that, for this method, $h_r < 1$ results in first-order convergence also for the fitted case.

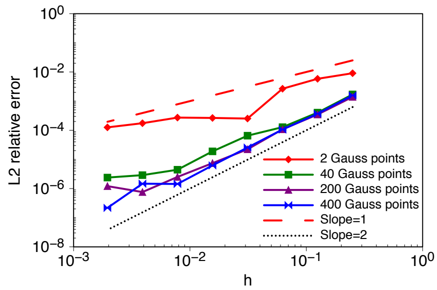

FIGURE 2.12. Importance of the quadrature scheme for the two-field DFD/BLM method using a standard quadrature with a different number of Gauss points on elements cut by the interface. Since the method is independent of the material ratio, we perform only one test, Test 1 (see Table 2.1), and the h-refinement strategy is described in Table 2.2. It can be observed that a clear quadratic rate of convergence is recovered with 400 Gauss points.

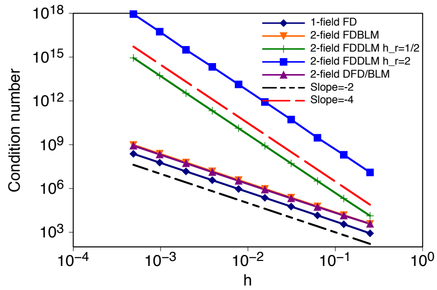

FIGURE 2.13. Condition numbers of the global linear system of the various methods. The problem under consideration is Test 1 with exact quadrature. However, similar results were obtained for different material parameters with exact and approximated integrations.

2.8. Discussion on the extension to higher dimensions, with a focus on the discontinuously extended two-field Fictitious Domain method with boundary Lagrange multipliers

The methods discussed in this chapter represent a stepping stone for multiple dimensional problems. For instance, the one-field method of Section 2.3 can be seen as an extremely simplified configuration with respect to more complex fluid-structure interaction problems studied in [**24**] or [**23**]. The order of accuracy of these methods is limited by the regularity of the solution and by the fact that the computational mesh does not fit with the interface. The focus of this chapter is to compare different approaches in order to identify the numerical schemes that can achieve higher order of convergence also in presence of material discontinuities.

Two-field methods, like the ones discussed in Sections 2.4 and 2.5 are saddle point problems and thus they require that an inf-sup condition is satisfied. Interested readers are referred to, e.g., [**50**] for Boundary Lagrange Multipliers and to [**51**] or [**6**] for distributed Lagrange multiplier. Since these methods are only first-order accurate we choose not to give here a detailed account about their extension, and we focus instead on the two-field DFD/BLM method which, under the assumptions presented in this chapter, is second-order accurate.

A simple approach for the Lagrange multiplier (e.g., by constructing a piecewise linear Lagrange multiplier space where the nodes are the intersection points of the interface with the extended mesh) in 2D or 3D results in locking (see for instance [**84**] and Appendix B). Such a problem occurs since there are more constraints by the Lagrange multiplier than "free" nodes associated with the elements cut by the interface.

We mention three possible strategies to solve the problem:

(1) Adding degrees of freedom in the primary field, such as bubbles (see [**83**]);
(2) Lowering the dimension of the Lagrange multiplier space (see [**16**]);
(3) Using stabilization techniques such as Nitsche (see [**84**]) or Barbosa-Hughes (see [**57**]).

The first strategy, if used with a piecewise constant Lagrange multiplier, consists in enriching elements cut by the interface with a bubble function (the bubble can be eliminated at the element level by static condensation). It is also possible to apply static condensation a second time to eliminate the Lagrange multiplier, and thus the method shares similarities with the Nitsche method (as shown in the work of [**83**]). An important feature of the method is that it does not depend on user parameters, unlike the third approach.

The second strategy has been applied to 2D problems in [**16**] and to 3D problems in [**58**]. The method consists in properly selecting intersection vertices of the interface with the extended mesh and taking the trace on the interface of the shape functions of the global mesh to build the Lagrange multiplier finite element space. Such a method is called the "Lagrange Multiplier Vital Vertices." It has been proven in [**16**] that it satisfies an inf-sup condition for 2D problems. We note that the main drawback of lowering the dimension of the Lagrange multiplier space is that it reduces the accuracy of the flux at the interface.

Concerning the third strategy, we have to say that the Nitsche method was introduced for interface problems in [**54**]. However, it has been shown in [**84**] that this method does not achieve satisfactory results for specific situations, but that a slight modification of the method introducing a second user parameter cures the problem. This method is known as the γ-Nitsche method. We point out that in [**54**] the first Nitsche parameter is given by geometrical consideration, and is thus defined locally on each intersected element, while the parameter γ may more likely depend on material parameters. Alternatively, in [**57**], a Barbosa-Hughes stabilization technique is proposed. We note that it has been shown in [**87**] that such a stabilization technique can be derived from the Nitsche method. Both approaches are dependent on user parameters which depend heavily on how the interface cuts the element. An inappropriate choice of parameters might result in a dramatic loss of accuracy. For instance, specific techniques have to be employed when subelements are very small compared to their global elements (see for instance

[**57**]). However, a promising path following [**21**] on the use of stabilization by projection has been introduced for boundary Lagrange multipliers in, e.g., [**13**], avoiding the computation of a stabilization parameters. These kinds of approaches constitute currently an active area of research (see, e.g., [**27**] and [**2**]).

2.9. Conclusive considerations for Chapter 2

In this chapter, we aimed at giving highlights of some fundamental issues of immersed approaches. In particular, within the finite element method, we analyzed various embedded approaches in order to tackle a 1D Poisson problem with different materials in a unified framework. We focused on four embedded methods inspired by the Immersed Boundary, the Fictitious Domain, and the Extended Finite Element, methods.

Detailed results showed that, in unfitted cases, the first three studied methods are only first-order accurate since they consider a continuous extension using standard finite elements, while the method inspired by the extended finite element method is second-order accurate because the irregularity of the solution at the interface was explicitly taken into account. Moreover, since it seems that for the latter method it is not straightforward conserving the optimal second order of convergence in higher dimensions while imposing essential constraints inside elements, we also commented on possible extension strategies of such a method to 2D/3D.

We note that one of the main issues regarding the efficiency of the method inspired by the extended finite element method, besides the imposition of essential boundary conditions on the interface, lies in the need to integrate correctly over sub-elements to obtain second-order accuracy. In other words, an important work is required in order to compute the intersection of the interface with the crossed elements. On the contrary, a much cheaper and easier to implement, in particular in 2D/3D, integration scheme may be used for first-order accurate methods without corrupting their rate of convergence. Therefore, a trade-off between computational cost and accuracy has to be always considered when dealing with immersed approaches.

CHAPTER 3

An "immersed" finite element method based on a locally anisotropic remeshing for the incompressible Stokes problem

3.1. Introduction

One of the key ingredients of the success of the finite element method is its flexibility in the representation of the geometry on which the problem is defined. However, for several applications with highly complex geometries or very localized singularities (such as interfaces, cracks, etc.), generating a correct geometry representation is a difficult task.

In this chapter we study an alternative approach, that consists in using a mesh which does not fit *a priori* the geometry, or the singularities, of the problem. For this reason, we refer to such class of approaches as *immersed boundary* methods. In the literature, these methods may be found under several names such as embedded, unfitted, and fictitious domain.

Many immersed boundary methods do not take into account explicitly the existence of the boundary and, as a consequence, they experience loss of accuracy. A possible solution consists in enriching the finite element basis on the elements that are crossed by the immersed boundary, such that the irregularity of the solution is taken into account. An example of methods using local enrichments are the so-called *eXtended Finite Element Method* (XFEM) (see [**57**] for a presentation of the XFEM method in the context considered in the present chapter, or [**47**] for a general overview of the method).

A first difficulty of the XFEM is that classical enriched functions might not be smooth inside an element, which leads to one of the major issues associated with such a methodology, i.e., a correct integration on elements that contain discontinuous functions. Nevertheless, the enriched functions are piecewisely smooth and, since the boundaries or the singularities are codimension 1 with respect to the geometry of the problem, we may construct "subelements" on which we can use standard quadrature rules. It follows that an important work is required to compute geometric structures to integrate.

A second difficulty is the imposition of essential constraints since the finite element basis may not be interpolatory on the immersed boundary. A possible solution consists in weakly enforcing constraints inside elements. However, such a strategy is not an easy solution (see for instance [**84**] and references therein).

On the contrary, in [**61**] an alternative approach is proposed. The method consists in reconstructing standard shape functions on the previously described subelements. Such an operation is rather an easy task with respect to the computational work required to obtain a geometric representation of the subelements. Their strategy is to use a stabilized low order finite element scheme such that newly added degrees of freedom, resulting from the reconstruction of the mesh, may be eliminated, with the advantage of a direct impact on the size of the system to solve. Drawbacks of the method are twofold. Firstly, only low order elements can be used such that there are no additional degrees of freedom and a stabilized finite element scheme is needed to ensure stability. Secondly, low order elements have a poor representation of the geometry and higher order elements may be preferred.

In the present chapter, we propose an approach similar to the one proposed by [**61**], but with higher order elements, starting from the Hood-Taylor. Notably, the subdivision process generates highly distorted elements. This approach is also similar to Octree and Delaunay mesh generation with boundary recovery (see, e.g., [**72**] or [**46**] and references therein). In a similar framework as proposed here, in [**90**] and [**91**] higher order elements are used for a fluid dynamics problem. However, both of these works employ a "smoothing" procedure in order to ensure a "good" shape of the refined elements. In particular, in [**91**] a geometric parameter is introduced to enforce well shaped elements. However, here we prefer not to use a smoothing procedure such that there is no change in the distribution of the vertices of the original mesh. An important consequence of such a choice is that the subdivision process generates highly distorted elements.A possible effect of the distortion of the elements for the Stokes problem is a loss in the inf-sup stability, even for well known stable elements. In [**5**], it has been noted that the Hood-Taylor may lack of inf-sup stability on stretched meshes. They provide five numerical tests and the Hood-Taylor element fails three of them. They also showed that adding an extra bubble to the velocity field stabilizes the element for all tests provided. Since our application may generate different structures for the distorted elements, we propose a test inspired by the presented immersed approach to stress the stability of both finite element scheme by computing a Smallest Generalized Eigenvalue (SGE) test. We effectively show that $\mathbf{P}_2/P_1$ may be unstable, whereas $\mathbf{P}_2^+/P_1$ (i.e., $\mathbf{P}_2/P_1$ with a cubic bubble on the velocity field) passes all SGE-tests. Additionally, we show with the SGE-test that the loss of stability of $\mathbf{P}_2/P_1$ may occur within small triangles in corners for which both edges are constrained by a Dirichlet boundary condition. We then present more complex cases from real applications to check the results from the SGE-tests. We present a test for which no elements are constrained in a corner and we find that both schemes are stable. Hence, it appears that $\mathbf{P}_2/P_1$ may be stable for a wide class of applications, but not for all, as we present two other problems where instability arises, as guessed from the SGE-test results. On the contrary, the inf-sup stability of $\mathbf{P}_2^+/P_1$ element is always obtained.

3.2. Geometry

In this section we consider the geometric aspects of the method, i.e., the problem of the construction of a mesh conveniently discretizing the considered physical domain. Two strategies are possible: "fitted" or "unfitted" (cf. Figure 3.1).

In the fitted approach the discretized domain fits the boundary of the problem, while in the unfitted approach the physical domain is a subset of the discretization. More precisely, in the unfitted case, we consider a problem defined on $\Omega \subset \mathbb{R}^2$ such that a part of the boundary of $\partial\Omega$, denoted by Γ (named *immersed boundary*), is not fitted *a priori* by the triangulation of $\hat{\Omega}$,

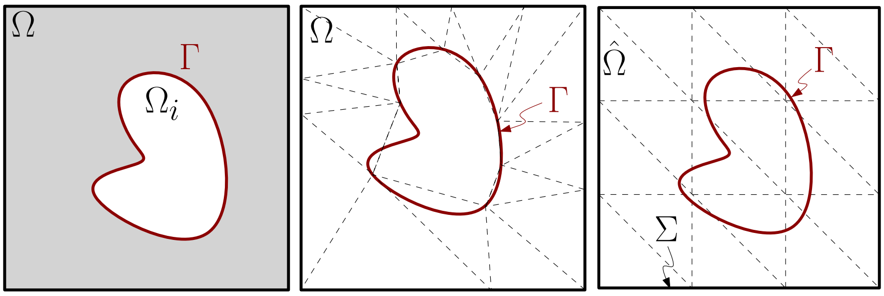

(a) Physical domain (b) Fitted grid (c) Unfitted grid

FIGURE 3.1. Fitted and unfitted discretizations of the physical region Ω: Ω_i is the interior (non physical) domain, Γ is the immersed boundary, $\Sigma = \partial\hat{\Omega}$ is the external boundary, and $\hat{\Omega} := \Omega \cup \Omega_i \cup \Gamma$ is the discretized domain.

with $\Omega \subset \hat{\Omega}$. The part of the boundary $\partial\Omega$ that is fitted by the triangulation of $\hat{\Omega}$ is denoted by Σ.

We illustrate the problem in Figure 1(c). To avoid the difficulties and the costs connected with the generation of fitted meshes in complicated situations, we propose to start with a regular unfitted mesh $\hat{\Omega}$ and to represent Γ by a linear reconstruction on such a triangulation, as illustrated in Figure 3.2. The reconstruction procedure is presented in detail in the next section.

3.2.1. Interface reconstruction

We assume that a regular triangulation $\hat{\mathcal{T}}$ of $\hat{\Omega}$ (named *background* mesh) and the interface Γ satisfy the conditions presented in [**54**], that is the boundary Γ crosses once two triangle edges. We note that there always exists a sufficiently fine triangulation of $\hat{\Omega}$ such that the conditions are fulfilled for any smooth immersed boundary. The reconstructed boundary of Γ is denoted Γ_h and it is the linear interpolation of all intersections with the background mesh edges. It follows that the reconstructed interface is a segment in each intersected element, and it defines a new domain Ω_h such that $\partial\Omega_h = \Sigma \cup \Gamma_h$ (cf. Figure 3.2). Domain Ω_h is referred to as integration domain. We point out that the linear reconstruction of Γ is not a limitation of the method we propose and that, in a case with a curved immersed boundary, isoparametric

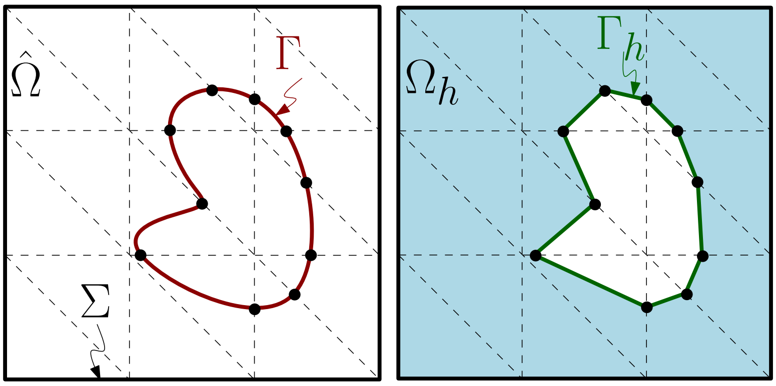

(a) Immersed boundary and a triangulation of $\hat{\Omega}$.

(b) Interface reconstruction (in green) and integration domain (in blue).

FIGURE 3.2. Description of the interface reconstruction process. The immersed boundary is denoted by Γ and the linear reconstruction of the immersed boundary, with respect to the background mesh, is denoted by Γ_h. In the remainder of the chapter we also consider the integration domain Ω_h (in blue), defined such that $\partial\Omega_h = \Sigma \cup \Gamma_h$.

elements may be used, as well as more complex algorithms, to describe the boundary.

We consider such types of methods as belonging to an "intersection class" of methods, since they require to compute intersection points between the immersed boundary and the mesh. On the contrary, for instance, the Finite Cell Method (see [**78**]) or the approach recently proposed by [**15**] does not belong to this class of methods. Knowing intersection points allows a subdivision of the mesh, which may be used for integration, construction of shape functions, etc. We point out that computing the intersection points is very demanding in terms of computational cost, and is a fundamental part of all codes using such an approach.

3.3. Model problem: Incompressible Stokes

Let $\Sigma = \Sigma_D \cup \Sigma_N$ where Σ_D denotes the part of the external boundary on which we impose a Dirichlet boundary condition and Σ_N the part on which we impose a Neumann boundary condition, whose value is assumed to be zero without loss of generality. On the other hand, on Γ, we consider homogeneous Dirichlet boundary conditions on Γ but non homogeneous Dirichlet boundary conditions can be applied as well. Neumann boundary conditions are not considered here because they can be enforced "naturally" in the variational formulation, and as a consequence, they are easier to tackle. The model problem we consider in this chapter is given by the following standard weak form of the incompressible Stokes equation:

Find $(\mathbf{u}, p) \in \boldsymbol{V}(\Omega) \times Q(\Omega)$ such that $\forall (\mathbf{v}, q) \in \boldsymbol{V}_0(\Omega) \times Q(\Omega)$:

$$\begin{cases} \displaystyle\int_\Omega \nabla \mathbf{u} : \nabla \mathbf{v} \, \mathrm{d}\Omega - \int_\Omega p \operatorname{div}(\mathbf{v}) \, \mathrm{d}\Omega = \int_\Omega \mathbf{f} \cdot \mathbf{v} \, \mathrm{d}\Omega, \\ \displaystyle\int_\Omega q \operatorname{div}(\mathbf{u}) \, \mathrm{d}\Omega = 0, \end{cases} \tag{3.1}$$

where

$$\begin{cases} \boldsymbol{V}(\Omega) := \{\mathbf{v} \in [H^1(\Omega)]^2;\ \mathbf{v}_{|\Sigma_D} = \mathbf{u}_D \text{ and } \mathbf{v}_{|\Gamma} = \mathbf{0}\}, \\ \boldsymbol{V}_0(\Omega) := \{\mathbf{v} \in [H^1(\Omega)]^2;\ \mathbf{v}_{|\Sigma_D} = \mathbf{0} \text{ and } \mathbf{v}_{|\Gamma} = \mathbf{0}\}, \\ Q(\Omega) := L^2(\Omega). \end{cases}$$

REMARK 14. *The constraint $\mathbf{u}_{|\Gamma} = \mathbf{0}$ is strongly enforced since it is imposed in the trial and test spaces. On the contrary, the incompressibility constraint is enforced weakly in the formulation and the pressure p is the corresponding Lagrange multiplier. We note, that since a weak imposition of a constraint with a Lagrange multiplier results in a saddle point problem, we have to choose a stable pair of elements for the velocity and the pressure satisfying an inf-sup condition (see* **[22]***). This issue is discussed further in Section 3.4. We note that in the case Σ_N is empty then $Q(\Omega) := L^2(\Omega)/\mathbb{R}$.*

3.3.1. A fundamental problem of immersed methods

In this Section we present a classical unfitted method (see the example in **[67]**) which consists in using the triangulation $\hat{\mathcal{T}}$ to build the finite element spaces and we point out its difficulties. We present the discretized problem with classical Hood-Taylor $\mathbf{P}_2/P_1$ finite elements (but the method may be generalized). The considered problem reads:

Find $(\mathbf{u}_h, p_h) \in \boldsymbol{V}^h \times Q^h$ such that $\forall(\mathbf{v}_h, q_h) \in \boldsymbol{V}_0^h \times Q^h$:

$$\left\{\begin{array}{l} \displaystyle\int_{\Omega_h} \nabla \mathbf{u}_h : \nabla \mathbf{v}_h \, \mathrm{d}\Omega_h - \int_{\Omega_h} p_h \operatorname{div}(\mathbf{v}_h) \, \mathrm{d}\Omega_h = \int_{\Omega_h} \mathbf{f} \cdot \mathbf{v}_h \, \mathrm{d}\Omega_h, \\ \displaystyle\int_{\Omega_h} q_h \operatorname{div}(\mathbf{u}_h) \, \mathrm{d}\Omega_h = 0, \end{array}\right. \tag{3.2}$$

where

$$\left\{\begin{array}{l} \mathbf{V}^h := \{\mathbf{v} \in C^0(\hat{\Omega}); \mathbf{v}_{|T} \in [\mathcal{P}_2]^2, \mathbf{v}_{|\Sigma_D^h} = \mathbf{u}_D \text{ and } \mathbf{v}_{|\Gamma^h} = \mathbf{0}, \forall T \in \hat{\mathcal{T}}\} \\ \quad \subset \mathbf{V}(\hat{\Omega}), \\ \mathbf{V}_0^h := \{\mathbf{v} \in C^0(\hat{\Omega}); \mathbf{v}_{|T} \in [\mathcal{P}_2]^2, \mathbf{v}_{|\Sigma_D^h} = \mathbf{0} \text{ and } \mathbf{v}_{|\Gamma^h} = \mathbf{0}, \forall T \in \hat{\mathcal{T}}\} \\ \quad \subset \mathbf{V}_0(\hat{\Omega}), \\ Q^h := \{q \in C^0(\hat{\Omega}); q_{|T} \in [\mathcal{P}_1], \forall T \in \hat{\mathcal{T}}\} \subset L^2(\hat{\Omega}), \end{array}\right.$$

where $\hat{\mathcal{T}}$ is a triangulation of $\hat{\Omega}$, $\mathcal{P}_k$ is the space of polynomials of degree k, and Σ_D^h is the discrete external Dirichlet boundary.

It is important to note that in Problem (3.2) the integration is performed on Ω_h and not on $\hat{\Omega}$ (see Section 3.3.2.1 for a subdivision strategy of $\hat{\Omega}$ to perform the quadrature). Indeed, as discussed in the work of **[75]** one cannot hope to obtain an optimal rate of convergence if the integration is performed on $\hat{\Omega}$. This result is independent of how the constraint $\boldsymbol{u} = \mathbf{0}$ on Γ is imposed.

For the considered problem, it is not possible to obtain optimal rate of convergence because the spaces $\boldsymbol{V}^h$ and $\boldsymbol{V}_0^h$ are not rich enough (see **[67]** for more details). We illustrate this issue in Figure 3.3. Indeed, for a general set of elements there are more constraints on the immersed boundary (i.e., at the intersection of the immersed boundary with the background mesh element edges) than nodes of the intersected elements that do not belong to the physical domain (named "free nodes"). As a consequence, the system is overconstrained and locking may occur. For example, in **[16]** an algorithm is presented such that two degrees of freedom are uniquely associated with an interface constraint. But, one of the drawbacks of the approach is that it

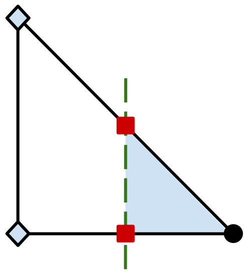

(a) Two internal constraints are satisfied since two "free" nodes are associated to it.

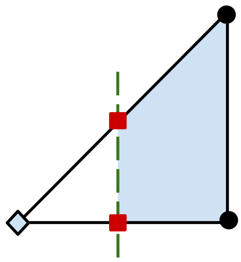

(b) The problem is over-constrained since only one "free" node is associated with the two internal constraints.

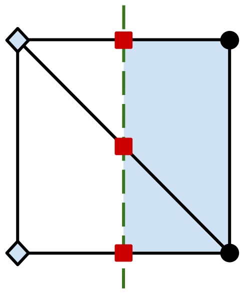

(c) This generic macro-element shows that the internal constraints cannot be imposed and thus locking occurs.

FIGURE 3.3. In this example we consider a single field problem. The elements are P_1 and the physical domain is depicted in blue. It follows that the diamonds are "free" nodes (i.e., their values have no physical relevance) while the dots are physical nodes. We want to illustrate the difficulty of imposing the internal constraint $\mathbf{u} = \mathbf{0}$ on the red squares. See also Appendix B for a discussion of locking issues using collocated Lagrange multipliers.

weakens the imposition of the Dirichlet boundary constraint on the immersed boundary.

We point out that since it is not possible to strongly impose the condition $\boldsymbol{u} = \mathbf{0}$ on Γ_h in order to obtain optimal rates of convergence, weak imposition of the Dirichlet condition is often used. A weak imposition can be performed, for instance, with a Lagrange multiplier (but checking the inf-sup condition for such a method is not an easy task, see [**16**] and references therein) or the Nitsche method which requires additional user parameters. Weak imposition of essential boundary conditions is still an active area of research (see for instance [**28**] for an example of the Nitsche method for the Stokes problem or alternative approaches in [**12**]) and [**33**]. The method we propose in the following avoids the use of complex strategies for weakly imposing essential boundary conditions. It consists in building a finite element basis that is interpolatory on the intersection points of the immersed boundary and the background mesh edges in order to impose Dirichlet boundary conditions strongly.

3.3.2. A method by a locally anisotropic remeshing

In the following, we propose a method that considers a special local refinement using a subdivision of elements cut by the immersed boundary. The method differs form the classical one presented in Problem (3.2), which uses the triangulation $\hat{\mathcal{T}}$ to build the finite elements. The proposed method consists in refining all elements cut by the immersed boundary such that a locally fitting mesh may be built. In particular, we show that such a subdivision process may not lead to a unique subdivision into triangles and we present a strategy to select the best subdivision.

3.3.2.1. *Subdivision*

For triangles cut by the immersed boundary we consider the two cases, depending if the subelement belonging to Ω_h is: a) a triangle, or b) a quadrilateral.

In the present work we consider finite elements only on triangles and thus in case b) we have to subdivide the quadrilateral into two triangles. As depicted in Figure 4(a), the subdivision into triangles of a quadrilateral is not unique, and therefore we propose a strategy to choose the best subdivision. The selection method for the subdivision of the quadrilateral into triangles is based on selecting the best element ratio pair, with the element ratio defined by

$$\sigma = \frac{h}{d},$$

where h and d are the diameters of the circumscribed and inscribed circles, respectively (see Figure 4(b)).

Remark 15. *It is clear that the subdivision may imply distorted elements. In two famous independent papers,* **[98]** *and* **[96]** *introduced the minimum angle condition for triangles. The condition requires that the smallest angle of a triangle has to be bounded from below by a strictly positive real. The*

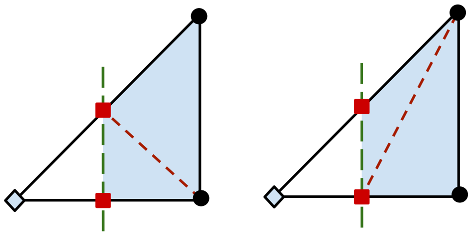

(a) Non unicity of the quadrilateral subdivision. The pair of triangles giving the smallest element ratios is selected (i.e., the pair on the left in this example).

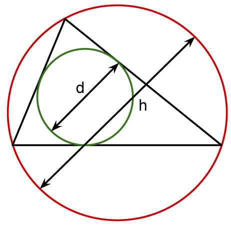

(b) The diameters of the circumscribed and inscribed circles are denoted h and d, respectively.

FIGURE 3.4. Selection of the quadrilateral subdivision in subtriangles and description of the element ratio.

minimum angle condition is a sufficient (but not necessary) condition to guarantee the convergence of the finite element method. In [**11**] *and* [**62**] *the maximum angle condition is introduced, which stipulates that the largest angle of a triangle has to be bounded above by a real strictly lower than* π*. Again the condition is sufficient to guarantee the optimal convergence of the finite element method. However, it has been noted in* [**53**] *that the maximum angle condition is not necessary and the finite element method for 2D problems may converge optimally without a maximum angle condition satisfied. Moreover, since we consider a saddle point problem, an inf-sup condition has to be satisfied as well, and finite element schemes that are stable on well shaped elements may not be stable on anisotropic ones. We discuss further this issue in Section 3.4.*

Accordingly, in the following sections, we consider a triangulation $\mathcal{T}_r$ built as follows. Given a shape regular triangulation $\hat{\mathcal{T}}$ of $\hat{\Omega}$ (i.e., the background mesh), we denote by $\mathcal{T}_\Gamma$ the triangulation of all elements that are crossed by Γ. As previously explained it is possible to build a subtriangulation $\mathcal{T}'_\Gamma|_T$ on every $T \in \mathcal{T}_\Gamma$ such that $\mathcal{T}'_\Gamma$ fits Γ, with respect to the linear reconstruction of Γ. Then, we consider the triangulation $\mathcal{T}_r$ made of all elements in $\hat{\mathcal{T}}$ that

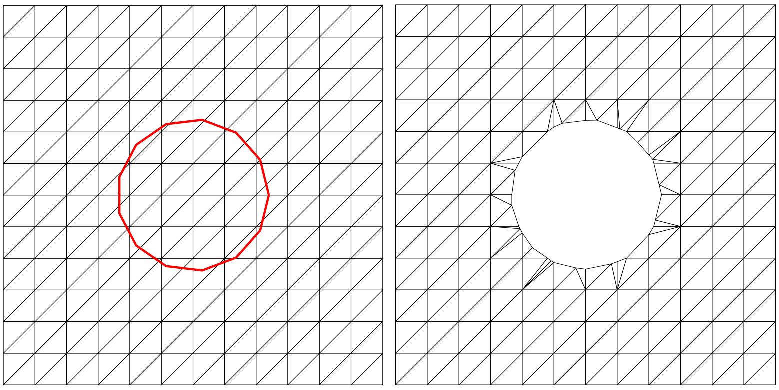

(a) Original mesh $\hat{\mathcal{T}}$.

(b) Refined mesh $\mathcal{T}_r$.

FIGURE 3.5. Subdivision operation of $\hat{\mathcal{T}}$ into $\mathcal{T}_r$.

are entirely in Ω_h and all elements of $\mathcal{T}'_\Gamma$ that are in Ω_h. The operation is illustrated in Figure 3.5 for the case of an immersed disk.

3.3.2.2. *Application to the incompressible Stokes problem*

In the following we give an example of the discretized Stokes problem using the locally refined method with the $\mathbf{P}_2/P_1$ finite element scheme:

Find $(\mathbf{u}_h, p_h) \in \boldsymbol{W}^h \times R^h$ such that $\forall (\mathbf{v}_h, q_h) \in \boldsymbol{W}_0^h \times R^h$:

$$
\left\{
\begin{aligned}
&\int_{\Omega_h} \nabla \mathbf{u}_h : \nabla \mathbf{v}_h \,\mathrm{d}\Omega_h - \int_{\Omega_h} p_h \,\mathrm{div}\,(\mathbf{v}_h)\,\mathrm{d}\Omega_h = \int_{\Omega_h} \mathbf{f}\cdot\mathbf{v}_h \,\mathrm{d}\Omega_h,\\
&\int_{\Omega_h} q_h \,\mathrm{div}\,(\mathbf{u}_h)\,\mathrm{d}\Omega_h = 0,
\end{aligned}
\right.
\tag{3.3}
$$

where

$$
\left\{
\begin{aligned}
&\mathbf{W}^h := \{\mathbf{v} \in C^0(\Omega_h); \mathbf{v}_{|T} \in [\mathcal{P}_2]^2, \mathbf{v}_{|\Sigma_D^h} = \mathbf{u}_D \text{ and } \mathbf{v}_{|\Gamma^h} = \mathbf{0}, \forall T \in \mathcal{T}_r\}\\
&\quad \subset \mathbf{V}(\Omega_h),\\
&\mathbf{W}_0^h := \{\mathbf{v} \in C^0(\Omega_h); \mathbf{v}_{|T} \in [\mathcal{P}_2]^2, \mathbf{v}_{|\Sigma_D^h} = \mathbf{0} \text{ and } \mathbf{v}_{|\Gamma^h} = \mathbf{0}, \forall T \in \mathcal{T}_r\}\\
&\quad \subset \mathbf{V}_0(\Omega_h),\\
&R^h := \{q \in C^0(\Omega_h); q_{|T} \in [\mathcal{P}_1], \forall T \in \mathcal{T}_r\} \subset L^2(\Omega_h).
\end{aligned}
\right.
$$

As we shall see later, such a scheme might not be a good choice for our method due to the instability of the Hood-Taylor element on distorted meshes. Therefore, we also consider the so-called $\mathbf{P}_2^+/P_1$ element, whose finite element space, for our application, is defined by

(3.4)
$$\begin{cases} \mathbf{W}^h := \{\mathbf{v} \in C^0(\Omega_h); \mathbf{v}_{|T} \in [\mathcal{P}_2 \oplus B_3]^2, \mathbf{v}_{|\Sigma_D^h} = \mathbf{u}_D,\ \mathbf{v}_{|\Gamma^h} = \mathbf{0}, \forall T \in \mathcal{T}_r\}, \\ \mathbf{W}_0^h := \{\mathbf{v} \in C^0(\Omega_h); \mathbf{v}_{|T} \in [\mathcal{P}_2 \oplus B_3]^2, \mathbf{v}_{|\Sigma_D^h} = \mathbf{0},\ \mathbf{v}_{|\Gamma^h} = \mathbf{0}, \forall T \in \mathcal{T}_r\}, \end{cases}$$

where B_3 denotes the space of cubic bubble functions (see **[22]** for more details).

REMARK 16. *As presented in Equation (3.4) the bubbles are used on all elements of the mesh $\mathcal{T}_r$. In practice, we add the bubble only on subtriangles.*

In Figure 3.6 we compare the methods presented with Problem (3.2) and Problem (3.3). We note that the present method has more degrees of freedom than the original described method. In **[61]**, which is based on a stabilized P_1/P_0 scheme, added discontinuous pressure degrees of freedom are eliminated by static condensation, while the new velocity degree of freedom are actually Dirichlet boundary nodes.

3.4. The inf-sup condition on anisotropic elements

Given the approximations $\mathbf{u}_h = \sum_{i=1}^n \mathbf{N}_i \hat{\mathbf{u}}_i$ and $p_h = \sum_{i=1}^m M_i \hat{p}_i$, where $\mathbf{N}_i$ and M_i are the finite element bases for $\mathbf{W}^h$ and R^h (with n and m the number of degrees of freedom, respectively) the discrete incompressible Stokes problem in matrix form reads

$$\begin{bmatrix} \mathbf{A} & \mathbf{B}^T \\ \mathbf{B} & \mathbf{0} \end{bmatrix} \begin{Bmatrix} \hat{\mathbf{u}} \\ \hat{\mathbf{p}} \end{Bmatrix} = \begin{Bmatrix} \hat{\mathbf{f}} \\ \hat{\mathbf{g}} \end{Bmatrix}, \tag{3.5}$$

where

$$\begin{cases} \mathbf{A}|_{ij} = \displaystyle\int_{\Omega_h} \nabla \mathbf{N}_i : \nabla \mathbf{N}_j \,\mathrm{d}\Omega_h & \forall (i,j) \in \{1,2,\dots,n\} \times \{1,2,\dots,n\}, \\ \mathbf{B}|_{ij} = -\displaystyle\int_{\Omega_h} M_i \,\mathrm{div}(\mathbf{N}_j) \,\mathrm{d}\Omega_h & \forall (i,j) \in \{1,2,\dots,m\} \times \{1,2,\dots,n\}. \end{cases}$$

Let $n+1, \dots, n+n_D$ be the eliminated degrees of freedom laying on Σ_D, the right hand side reads

$$\begin{cases} \hat{\mathbf{f}}|_i = \displaystyle\int_{\Omega_h} \mathbf{f}_h \cdot \mathbf{N}_i \,\mathrm{d}\Omega_h - (\bar{\mathbf{A}} \hat{\mathbf{u}}_D)|_i & \forall i \in \{1,2,\dots,n\}, \\ \hat{\mathbf{g}}|_i = -(\bar{\mathbf{B}} \hat{\mathbf{u}}_D)|_i & \forall i \in \{1,2,\dots,m\}, \end{cases}$$

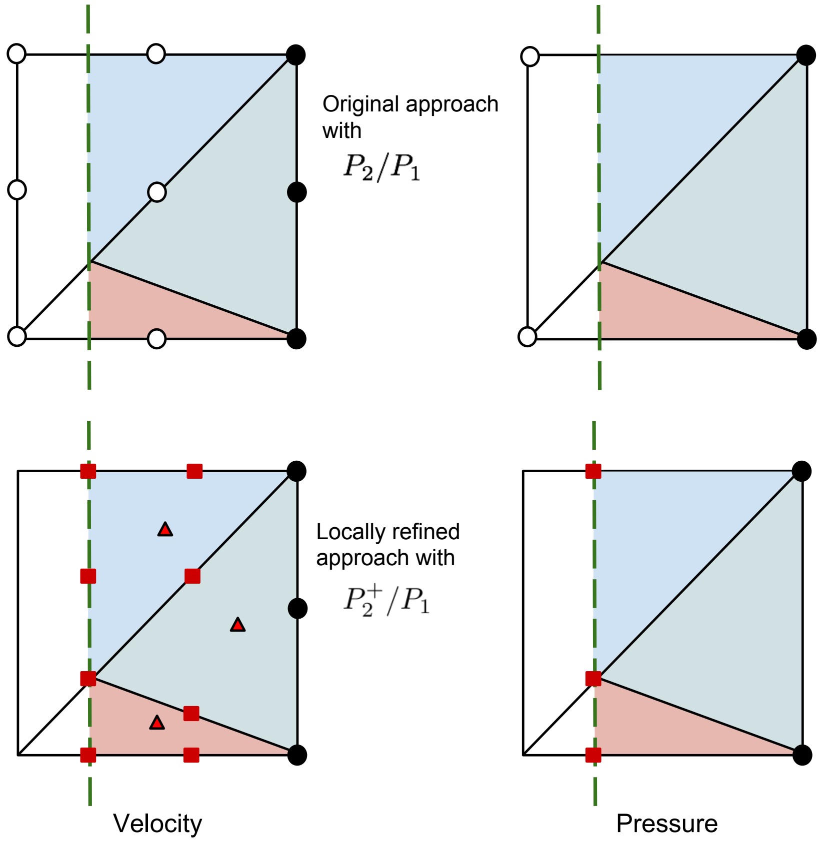

FIGURE 3.6. Comparison between original $\mathbf{P}_2/P_1$ (Problem (3.2)) and locally refined $\mathbf{P}_2^+/P_1$ (Problem (3.3)). The black dots are common degrees of freedom, white dots are eliminated degrees of freedom (i.e., the nodes that are present in the original method which are not present in the locally refined method), red squares are added degrees of freedom, and triangles are bubble degrees of freedom.

where

$$\begin{cases} \bar{\mathbf{A}}|_{ij} = \displaystyle\int_{\Omega_h} \nabla \mathbf{N}_i : \nabla \mathbf{N}_j \, \mathrm{d}\Omega_h, \\ \qquad \forall (i,j) \in \{1,2,\ldots,n\} \times \{n+1, n+2, \ldots, n+n_D\}, \\ \bar{\mathbf{B}}|_{ij} = -\displaystyle\int_{\Omega_h} M_i \operatorname{div}(\mathbf{N}_j) \, \mathrm{d}\Omega_h, \\ \qquad \forall (i,j) \in \{1,2,\ldots,m\} \times \{n+1, n+2, \ldots, n+n_D\}, \end{cases}$$

and $\hat{\mathbf{u}}_D$ are the nodal boundary values of $\mathbf{u}_D$.

In the following we also use the pressure mass matrix defined by

$$\mathbf{M}_{|ij} = \int_{\Omega_h} M_i M_j \mathrm{d}\Omega_h \qquad \forall (i,j) \in \{1,2,\ldots,m\} \times \{1,2,\ldots,m\}. \tag{3.6}$$

The euclidean norm is given by $||\hat{\mathbf{v}}||_0^2 = \hat{\mathbf{v}}^T\hat{\mathbf{v}}$ with $\hat{\mathbf{v}} \in \mathbb{R}^n$. We also consider the norm defined by the stiffness matrix $\mathbf{A}$, that is $||\hat{\mathbf{v}}||_A^2 = \hat{\mathbf{v}}^T\mathbf{A}^T\hat{\mathbf{v}}$ and its associated dual norm given by $||\hat{\mathbf{v}}||_{A'}^2 = \hat{\mathbf{v}}^T\mathbf{A}^{-T}\hat{\mathbf{v}}$. Let $\hat{\mathbf{q}} \in \mathbb{R}^m$, then the norm used for the pressure field is given by $||\hat{\mathbf{q}}||_M^2 = \hat{\mathbf{q}}^T\mathbf{M}^T\hat{\mathbf{q}}$ and its associated dual norm by $||\hat{\mathbf{q}}||_{M'}^2 = \hat{\mathbf{q}}^T\mathbf{M}^{-T}\hat{\mathbf{q}}$, where $\mathbf{M}$ is defined in Equation (3.6).

It is well known that a key component for Equation (3.5) to have a unique solution is the satisfaction of the following condition (see **[22]**):

Inf-sup: $\exists \beta_h > 0$ (independent of h) such that

$$\max_{\hat{\mathbf{v}} \in \mathbb{R}^n \setminus \{\mathbf{0}\}} \frac{\hat{\mathbf{v}}^T\mathbf{B}^T\hat{\mathbf{q}}}{||\hat{\mathbf{v}}||_A} \geq \beta_h ||\hat{\mathbf{q}}||_M \qquad \forall \hat{\mathbf{q}} \in \mathbb{R}^m \tag{3.7}$$

Being $\hat{\mathbf{u}}^I$ and $\hat{\mathbf{p}}^I$ the vectors of analytical solutions at the nodes for the velocity and the pressure, respectively, an error estimate is given by (see **[22]**):

$$||\hat{\mathbf{u}}^I - \hat{\mathbf{u}}||_A \leq C\left(||\hat{\mathbf{f}}||_{A'} + \beta_h^{-1}||\hat{\mathbf{g}}||_{M'}\right), \tag{3.8}$$

$$||\hat{\mathbf{p}}^I - \hat{\mathbf{p}}||_M \leq C\left(\beta_h^{-1}||\hat{\mathbf{f}}||_{A'} + \beta_h^{-2}||\hat{\mathbf{g}}||_{M'}\right), \tag{3.9}$$

where C denotes a general constant independent of h and β_h.

We clearly can see from Equations (3.8) and (3.9) that if $\beta_h \to 0$ as $\sigma \to \infty$ then the error for the pressure may not be bounded and it depends on $1/\beta_h^2$, while the velocity field may also not be bounded but it depends only on $1/\beta_h$.

We equip the space $\mathbf{V}$ and Q (see Equations (3.1)) with the norms

$$\begin{cases} ||\mathbf{v}||_V^2 &= \displaystyle\int_\Omega \nabla\mathbf{v} : \nabla\mathbf{v}\mathrm{d}\Omega, \\ ||q||_Q^2 &= \displaystyle\int_\Omega q^2 \mathrm{d}\Omega, \end{cases}$$

where $\mathbf{v} \in \mathbf{V}(\Omega)$ and $q \in Q(\Omega)$. Given that $\mathbf{u}^I = \sum_i \hat{\mathbf{u}}_i^I \mathbf{N}_i$ and $q^I = \sum_i \hat{q}_i^I M_i$ are the interpolant of the analytical solution using the finite element basis, it can be shown that (see [**9**])

$$||\hat{\mathbf{u}}^I - \hat{\mathbf{u}}||_A \leq C \left(\beta_h^{-1}||\mathbf{u}^I - \mathbf{u}_h||_V + ||p^I - p_h||_Q\right), \tag{3.10}$$

$$||\hat{\mathbf{p}}^I - \hat{\mathbf{p}}||_M \leq C \left(\beta_h^{-2}||\mathbf{u}^I - \mathbf{u}_h||_V + \beta_h^{-1}||p^I - p_h||_Q\right). \tag{3.11}$$

To conclude, it is very important that for the chosen finite element choice β_h remains bounded from below as σ increases. In other words, we would like to have β_h to be independent of σ.

3.4.1. Numerical methods to measure the inf-sup condition (a Smallest Generalized Eigenvalue test)

In order to test if our finite element scheme choice remains stable as σ increases, we compute numerically the inf-sup constant.

It can be proven that (see, e.g., [**40**]) the inf-sup constant β_h is given by the square root of the lowest positive eigenvalue of the following generalized eigensystem:

$$\mathbf{B}\mathbf{A}^{-1}\mathbf{B}^T\mathbf{q} = \lambda\mathbf{M}\mathbf{q}, \tag{3.12}$$

where $\mathbf{B}\mathbf{A}^{-1}\mathbf{B}^T$ is called the Schur complement.

Remark 17. *In the case of an enclosed flow, the first eigenvalue is zero, since it represents the constant pressure mode. In such a case β_h is estimated by the square root of the second lowest eigenvalue. On the contrary, if the problem admits a Neumann boundary condition then all eigenvalues are strictly positive.*

3.5. Numerical Tests

In this section we propose two kinds of numerical experiments, solved both with the $\mathbf{P}_2/P_1$ and $\mathbf{P}_2^+/P_1$ schemes described above. We recall that, when considering the $\mathbf{P}_2^+/P_1$ scheme, the bubbles are added only on the subtriangles. On all other elements the $\mathbf{P}_2/P_1$ scheme is used.

The first experiment is a test in which the “inflow” condition is applied on the immersed boundary. We then study the solution of the problem on very simple meshes as the position of the immersed boundary varies. We consider three cases for the SGE-test: a constant flow, a Poiseuille flow, and a colliding flow. Each SGE-test has an analytical solution, which is presented in subsequent sections.

The second set of experiments explores three applications. The first problem is a Stokes flow around a disk, with the disk boundary being the immersed boundary. The second problem is a flow against an “obstacle” that defines a part of the boundary of the fluid domain. The third problem is a “surface” flow problem, where the surface is described by an immersed boundary.

We also provide and discuss for some representative tests the condition number, denoted by κ, of Schur complement, see Equation (3.12)

REMARK 18. *We point out that in all presented tests integration was performed exactly. However, further numerical experiments showed that the use for* $\mathbf{P}_2^+/P_1$ *of the integration rule exact on* $\mathbf{P}_2/P_1$ *(clearly leading to an under-integration of the terms involving bubble shape functions) leads to practically identical results. This is in agreement with what is expected from a theoretical point of view. It thus follows that* $\mathbf{P}_2^+/P_1$ *at a cost similar to* $\mathbf{P}_2/P_1$.

3.5.1. Smallest Generalized Eigenvalue test problems

The Smallest Generalized Eigenvalue test (SGE-test) is presented in Figure 3.7. The background mesh is defined on $[-1,1] \times [-1,1]$ and the mesh used for the SGE-test is shown in Figure 3.8. The problem consists in varying the position of an "immersed" boundary (depicted in red in Figure 3.7) from -1 to 0, representing two tests:

- Test 1: $a \to 0$ with inflow positions described in Table 1(a) (examples are given in Figures 8(a)),
- Test 2: $b \to 0$ with inflow positions described in Table 1(b) (examples are given in Figure 8(d)).

The physical domain of the problem is on the right of the immersed boundary. We necessarily impose a Dirichlet boundary condition on the immersed boundary, which are different for each cases: the constant flow, the Poiseuille flow, and the colliding flow.

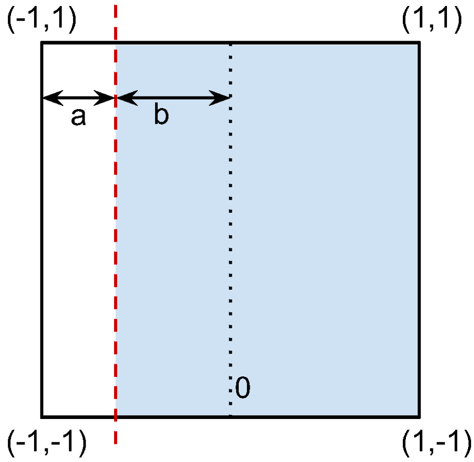

FIGURE 3.7. Immersed boundary (dotted red), physical domain (in blue) geometric data for an SGE-test problem.

a	$1e{-}1$	$1e{-}2$	$1e{-}3$	$1e{-}4$	$1e{-}5$
σ	9.6	99.6	$1.0e3$	$1.0e4$	$1.0e5$

(a) Test 1: $a \to 0$.

b	$1e{-}1$	$1e{-}2$	$1e{-}3$	$1e{-}4$	$1e{-}5$
σ	13.1	140	$1.4e3$	$1.4e4$	$1.4e5$

(b) Test 2: $b \to 0$.

TABLE 3.1. Geometric considerations for both tests. The highest element ratio is denoted by σ.

We note that in both tests the element ratio σ scales linearly. In the following, we report the numerical results relative to the different flow conditions considered.

For the first two SGE-test cases, we evaluate the results in terms of the discrete L^2-norm for both the velocity and the pressure fields. More precisely given $\hat{\mathbf{u}}_i^I = \mathbf{u}(\boldsymbol{x}_i)$ and $\hat{p}_i^I = p(\boldsymbol{x}_i)$ the analytical solution of the velocity and the pressure, respectively, at the node $\boldsymbol{x}_i$, the discrete L^2 velocity error is defined by

$$e_v = \sqrt{(\hat{\mathbf{u}}^I - \hat{\mathbf{u}})^T(\hat{\mathbf{u}}^I - \hat{\mathbf{u}})} = ||\hat{\mathbf{u}}^I - \hat{\mathbf{u}}||_0,$$

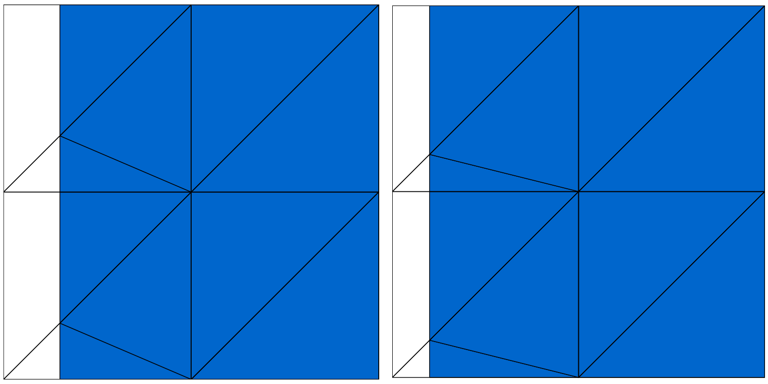

(b) a=0.3 (c) a=0.2

(c) Test 1: Deformation of the refined elements as a tends to 0.

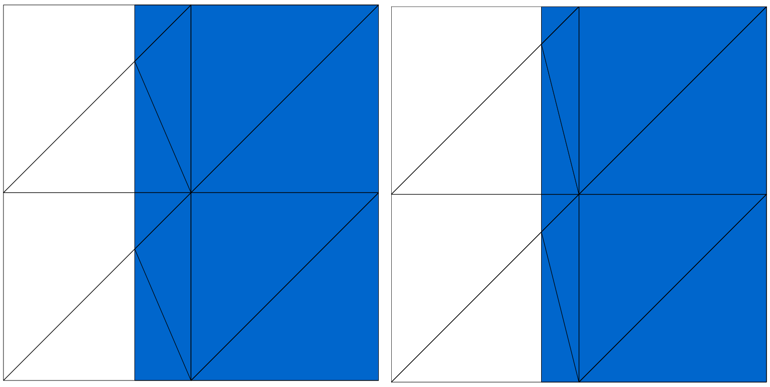

(e) b=0.3 (f) b=0.2

(f) Test 2: Deformation of the refined elements as b tends to 0.

FIGURE 3.8. Mesh under consideration for the SGE-tests with different immersed boundary positions. The background domain is defined on $[-1,1]\times[-1,1]$. Smallest element ratios for the considered values in the two tests are depicted in Table 3.1

and the discrete L^2 pressure error is defined by

$$e_p = \sqrt{(\hat{\mathbf{p}}^I - \hat{\mathbf{p}})^T(\hat{\mathbf{p}}^I - \hat{\mathbf{p}})} = ||\hat{\mathbf{p}}^I - \hat{\mathbf{p}}||_0.$$

3.5.1.1. *Constant flow*

The first case consists in imposing a constant inflow. The boundary conditions are $u_x = 1$ and $u_y = 0$ on $x = a - 1$ for Test 1 and on $x = -b$ for

Test 2, respectively. On $x = 1$ *and* $y \pm 1$ we apply the so-called "do-nothing" boundary condition, that is $\nabla \mathbf{u} \cdot \mathbf{n} - p\mathbf{n} = \mathbf{0}$, where $\mathbf{n}$ is the outward normal.

The analytical solution for the constant flow problem is given by

$$\begin{cases} u_x(x,y) & = 1, \\ u_y(x,y) & = 0, \\ p(x,y) & = 0. \end{cases}$$

For Tests 1 and 2, (see results in Table 3.2 and Table 3.3, respectively) it is clear that both elements are stable as the numerical inf-sup constant remains bounded from below. Moreover, as already pointed out, the element ratio increases linearly for both tests and thus the condition that the element ratio remains bounded from above is not a necessary condition for both finite element schemes.

The condition number of the Schur complement (see Equation (3.12)) is denoted by κ. We can observe in Table 3.2 that for Test 1 κ scales as a^{-1}, while we see from Table 3.3 that for Test 2 it scales as b^{-2}. We point out that for Test 1 the smallest area of the triangles scales as a while for Test 2 it scales as b^2, leading to the different conditioning rates of the Schur complement between Test 1 and Test 2. Bounds for the conditioning of the Schur complement are provided in, e.g., [**22**] or in Proposition 4.47 from [**42**] as function of the inf-sup constant and the condition number of the pressure mass matrix. A bound for the mass matrix with anisotropic elements is provided in, e.g., [**63**]. The results are consistent with the theory.

3.5.1.2. *Poiseuille flow*

The second case consists in a viscous flow between two infinite plates positioned respectively on $y \pm 1$. The boundary conditions are $u_x = (1 - y^2)$ and $u_y = 0$ on $x = a - 1$ for Test 1 and $x = -b$ for Test 2. On $y = \pm 1$ the so-called "no-slip" boundary condition is applied, that is $\mathbf{u} = \mathbf{0}$. On $x = 1$ the do-nothing boundary condition is applied. The analytical solution for

a	$1e{-}1$	$1e{-}2$	$1e{-}3$	$1e{-}4$	$1e{-}5$
β_h	0.505	0.500	0.500	0.500	0.500
κ	4.93e+02	5.01e+03	5.07e+04	5.02e+05	5.02e+06
e_v	7.172e-15	1.41e-14	4.99e-13	1.11e-12	1.48e-12
e_p	1.499e-14	8.42e-14	3.43e-12	7.71e-12	1.15e-11

(a) $\mathbf{P}_2/P_1$

a	$1e{-}1$	$1e{-}2$	$1e{-}3$	$1e{-}4$	$1e{-}5$
β_h	0.667	0.636	0.633	0.632	0.632
κ	2.91e+02	3.11e+03	3.14e+04	3.14e+05	3.14e+06
e_v	1.010e-14	8.38e-15	1.11e-13	3.27e-12	3.55e-11
e_p	2.337e-14	2.76e-14	7.66e-13	2.00e-11	2.30e-10

(b) $\mathbf{P}_2^+/P_1$

TABLE 3.2. Constant flow Test 1: $a \to 0$.

b	$1e{-}1$	$1e{-}2$	$1e{-}3$	$1e{-}4$	$1e{-}5$
β_h	0.548	0.509	0.501	0.500	0.500
κ	2.26e+03	2.65e+05	2.76e+07	2.76e+09	2.76e+11
e_v	1.792e-15	1.68e-15	1.55e-15	2.09e-15	1.73e-15
e_p	7.767e-14	2.36e-13	2.99e-12	8.47e-11	3.87e-10

(a) $\mathbf{P}_2/P_1$

b	$1e{-}1$	$1e{-}2$	$1e{-}3$	$1e{-}4$	$1e{-}5$
β_h	0.686	0.657	0.640	0.638	0.638
κ	1.23e+03	1.42e+05	1.46e+07	1.46e+09	1.47e+11
e_v	2.086e-15	2.49e-15	1.82e-15	2.72e-15	3.17e-15
e_p	2.440e-14	7.71e-13	5.76e-12	9.46e-11	1.35e-09

(b) $\mathbf{P}_2^+/P_1$

TABLE 3.3. Constant flow Test 2: $b \to 0$.

the Poiseuille flow problem is given by

$$\begin{cases} u_x(x,y) & = (1-y^2), \\ u_y(x,y) & = 0, \\ p(x,y) & = 2-2x. \end{cases} \tag{3.13}$$

a	$1e-1$	$1e-2$	$1e-3$	$1e-4$	$1e-5$
β_h	0.360	0.354	0.354	0.354	0.354
κ	2.24e+02	1.70e+03	1.65e+04	1.64e+05	1.64e+06
e_v	6.642e-16	2.66e-15	1.03e-13	2.20e-13	4.79e-12
e_v	8.058e-15	3.49e-14	1.63e-12	3.46e-12	7.56e-11

(a) $\mathbf{P}_2/P_1$

a	$1e-1$	$1e-2$	$1e-3$	$1e-4$	$1e-5$
β_h	0.405	0.393	0.392	0.392	0.392
κ	1.28e+02	1.06e+03	1.03e+04	1.03e+05	1.03e+06
e_v	1.122e-15	4.46e-15	2.77e-14	1.77e-12	6.08e-12
e_v	1.691e-14	4.29e-14	2.23e-13	1.46e-11	5.03e-11

(b) $\mathbf{P}_2^+/P_1$

TABLE 3.4. Poiseuille flow Test 1: $a \to 0$.

As for the constant flow, also in this case, both finite element schemes are stable for Test 1 (see Table 3.4).

However, for Test 2, the $\mathbf{P}_2/P_1$ finite element is not stable anymore (see Table 5(a)), as the inf-sup constant decreases sublinearly (with a rate of $\mathcal{O}(b^{1/2})$) as b tends to 0. We remark that in case one uses a geometric tolerance as employed in **[91]** or with the XFEM, this result points out the direct dependence of the inf-sup constant on such a geometrical tolerance. The $\mathbf{P}_2^+/P_1$ scheme is instead stable. The main difference with the constant flow SGE-test is the presence of Dirichlet boundary conditions on $y = \pm 1$. Further tests presented in Appendix C show that the instability appears from the upper left corner of the domain, where a small triangle, while well shaped, has an area that decreases as $\mathcal{O}(b^2)$. We point out that, to the best of the authors' knowledge, a proof of stability of $\mathbf{P}_2^+/P_1$ for distorted meshes has not been published.

We note that the solution for the constant flow and the Poiseuille flow is contained in the finite element spaces. Therefore, even if the numerical inf-sup constant tends to zero, the solution remains close to zero (see error estimates in Section 3.4).

b	$1e{-}1$	$1e{-}2$	$1e{-}3$	$1e{-}4$	$1e{-}5$
β_h	0.198	0.066	0.021	0.007	0.002
κ	8.51e+03	7.40e+06	7.27e+09	7.26e+12	7.26e+15
e_v	1.171e-15	8.58e-16	8.49e-16	8.64e-16	6.59e-16
e_v	1.459e-13	9.11e-13	4.39e-10	2.12e-08	2.61e-06

(a) $\mathbf{P}_2/P_1$

b	$1e{-}1$	$1e{-}2$	$1e{-}3$	$1e{-}4$	$1e{-}5$
β_h	0.435	0.380	0.370	0.369	0.368
κ	1.43e+03	2.00e+05	2.13e+07	2.15e+09	2.15e+11
e_v	9.710e-16	9.51e-16	1.01e-15	1.35e-15	7.23e-16
e_v	1.644e-14	2.80e-13	4.89e-12	6.00e-11	3.99e-10

(b) $\mathbf{P}_2^+/P_1$

Table 3.5. Poiseuille flow Test 2: $b \to 0$.

Regarding the conditioning of the Schur complement we can observe in Table 5(a), i.e., in the case P_2/P_1 is inf-sup unstable, that the condition number worsens since it does not scale as b^{-2} but as b^{-3}. This result is consistent with the theory.

3.5.1.3. *Colliding flow*

The third case is a colliding flow problem. In this case, we impose Dirichlet boundary condition everywhere, including the immersed boundary. They are given by the following, which is the analytical solution of the problem.

$$\begin{cases} u_x(x,y) &= 20xy^3, \\ u_y(x,y) &= 5x^4 - 5y^4, \\ p(x,y) &= 60x^2y - 20y^3 + \text{constant}. \end{cases}$$

Since it is an enclosed flow problem, the following constraint on the pressure is added:

$$\int_\Omega p \, \mathrm{d}\Omega = 0.$$

For SGE-test case 3, we use the relative error norm, that is

$$e_{v,r} = ||\hat{\mathbf{u}}^I - \hat{\mathbf{u}}||_0 / ||\hat{\mathbf{u}}^I||_0,$$

a	$1e{-}1$	$1e{-}2$	$1e{-}3$	$1e{-}4$	$1e{-}5$
β_h	0.369	0.367	0.366	0.366	0.367
re_v	3.90e-02	3.86e-02	3.86e-02	3.86e-02	3.86e-02
re_p	7.82e-01	7.74e-01	7.75e-01	7.75e-01	7.75e-01

(a) $\mathbf{P}_2/P_1$

a	$1e{-}1$	$1e{-}2$	$1e{-}3$	$1e{-}4$	$1e{-}5$
β_h	0.376	0.376	0.376	0.376	0.376
re_v	4.05e-02	3.84e-02	3.83e-02	3.82e-02	3.82e-02
re_p	7.58e-01	7.77e-01	7.80e-01	7.81e-01	7.81e-01

(b) $\mathbf{P}_2^+/P_1$

TABLE 3.6. Colliding flow Test 1: $a \to 0$.

and

$$e_{p,r} = ||\hat{\mathbf{p}}^I - \hat{\mathbf{p}}||_0/||\hat{\mathbf{p}}^I||_0,$$

for the velocity and the pressure, respectively.

Again for Test 1 (see Table 3.6) both finite element schemes are stable and for Test 2 (see Table 3.7) the $\mathbf{P}_2/P_1$ scheme is not stable, on the contrary to the $\mathbf{P}_2^+/P_1$ scheme. In this case, the analytical solution is not contained anymore in the finite element space and we can observe that, as the numerical inf-sup constant β_h tends to 0 as $b \to 0$ with a rate of $\mathcal{O}(b^{1/2})$, the relative pressure error explodes linearly, which is in accordance with the error estimates in Equation (3.9). On the contrary, the velocity error remains bounded, which is not expected from the error estimate in Equation (3.8). More precisely, we would expect the velocity error to increase with an order of $\mathcal{O}(b^{1/2})$. However, a good velocity field with a bad pressure field is often seen, for example with the $\mathbf{Q}_1/P_0$ mixed element.

3.5.2. Applications

In this section, we present various possible applications as described in Figure 3.9. For the first experiment (see Figure 9(a)), we compare a fitted and an unfitted solution. We also investigate some extreme cases, with very distorted elements that can occur during simulations. We show that the

b	$1e{-}1$	$1e{-}2$	$1e{-}3$	$1e{-}4$	$1e{-}5$
β_h	0.197	0.066	0.021	0.007	0.002
re_v	5.23e-02	6.23e-02	6.56e-02	6.60e-02	6.60e-02
re_p	3.66e+00	5.03e+01	5.33e+02	5.37e+03	5.37e+04

(a) $\mathbf{P}_2/P_1$

b	$1e{-}1$	$1e{-}2$	$1e{-}3$	$1e{-}4$	$1e{-}5$
β_h	0.360	0.335	0.328	0.327	0.327
re_v	5.22e-02	6.22e-02	6.56e-02	6.60e-02	6.60e-02
re_p	1.14	2.17	2.45	2.48	2.49

(b) $\mathbf{P}_2^+/P_1$

TABLE 3.7. Colliding flow Test 2: $b \to 0$.

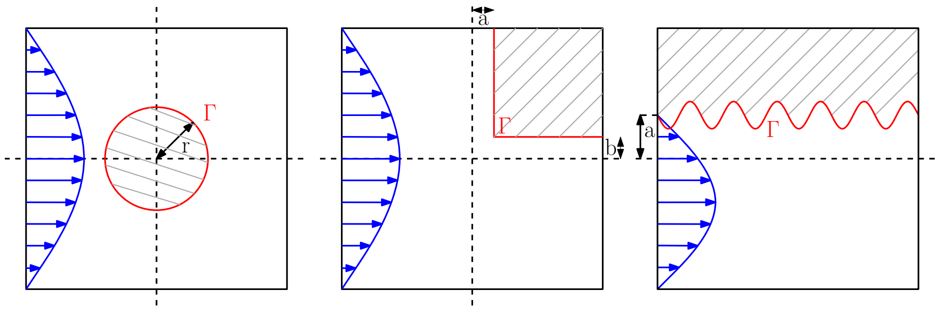

(a) Flow around a disk. (b) Flow against an obstacle. (c) surface flow.

FIGURE 3.9. Three flow problems. The striped zone is excluded from the fluid domain.

$\mathbf{P}_2/P_1$ is actually stable for that problem. Nevertheless, we show that the solution using the $\mathbf{P}_2^+/P_1$ is smoother. Then, we present two additional applications (described in Figures 9(b) and 9(c)) for which the $\mathbf{P}_2/P_1$ fails, while $\mathbf{P}_2^+/P_1$ is stable. For both failing cases, the culprit is a very small triangle in corners for which Dirichlet boundary conditions are applied on both boundary edges, as found in the SGE-tests. For all tests we do not present the results for the velocity field but the solution is in accordance with those obtained with the SGE-tests, i.e., the accuracy of the velocity field remains very good even when highly distorted elements are present.

3.5.2.1. *Flow around a disk*

We here consider a problem consisting of a flow around a cylinder between two plates. By symmetry, the problem reduces to a 2D flow around a disk, whose boundary is defined as an immersed boundary (see Figure 9(a)). The fluid domain is defined on $[-1,1] \times [-1,1]$. The inflow condition is a Poiseuille inflow and is given by Equation (3.13), no-slip boundary conditions are prescribed on $y = \pm 1$ and a do-nothing boundary condition is applied on $x = 1$. The disk has a radius of 0.3 and a no-slip boundary condition is applied on its surface. A comparison between a standard finite element solution and the proposed method is presented in Figure 3.10 with the $\mathbf{P}_2/P_1$ scheme for both methods. We can observe that the solution is similar to a standard finite element solution, and thus the presented method provides an accurate solution of the problem.

In the following we discuss in more details possible effects of distorted elements with the $\mathbf{P}_2/P_1$ and the $\mathbf{P}_2^+/P_1$ elements. We present two cases with highly distorted elements. The first one with a background mesh of 11×11 quadrilaterals and the second with a background mesh of 23×23 quadrilaterals, then divided into triangles with their diagonals such that $x - y =$ constant. The results are presented in Figure 3.11. We observe that the inf-sup constant is identical ($\beta_h \approx 0.18$) for both finite element schemes on meshes with distorted elements, and thus indicating stability of both schemes. However, we can see that the $\mathbf{P}_2^+/P_1$ solution is smoother than the pressure solution with the $\mathbf{P}_2/P_1$ element. Also, the oscillations appear to vanish as the mesh size is reduced. We point out that, in this problem, none of the distorted elements are recessed in a corner with Dirichlet boundary conditions applied on both corner sides. This situation occurs in the constant SGE-test problem for which both finite element schemes are stable for all tests. Therefore, it is possible that for many practical applications the $\mathbf{P}_2/P_1$ element is actually stable.

3.5.2.2. *Flow against an obstacle*

In this problem (depicted in Figure 9(b)) we consider a flow problem against an "obstacle". In this particular case the immersed boundary is not

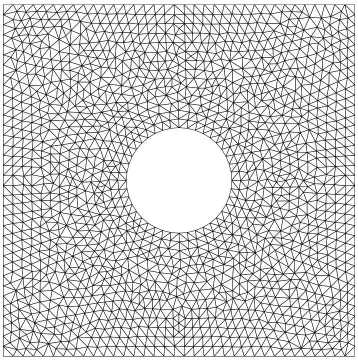

(a) Fitted mesh with 2884 elements.

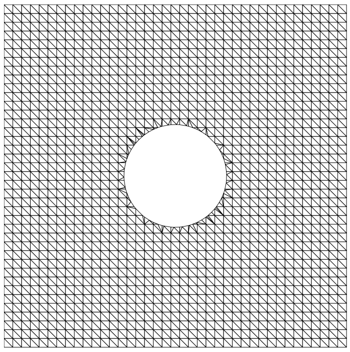

(b) Unfitted mesh with 2902 elements.

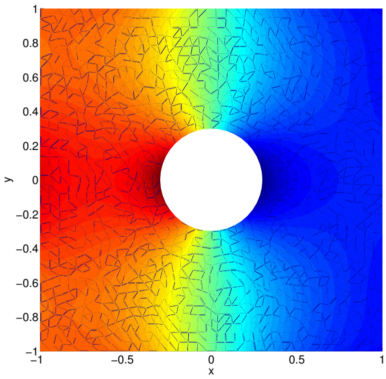

(c) Fitted pressure.

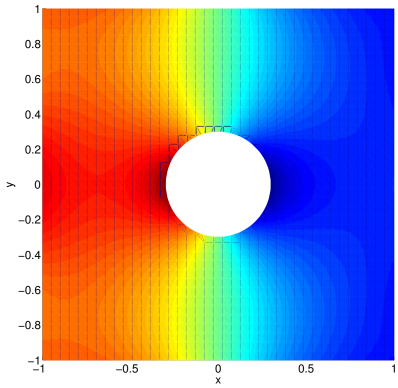

(d) Unfitted pressure.

FIGURE 3.10. Solution of the incompressible Stokes problem around a disk with the $\mathbf{P}_2/P_1$ and a Poiseuille inflow. The radius of the disk is 0.3.

closed and defines a part of the outer boundary of the fluid domain. The background fluid domain is defined on a $[-1,1] \times [-1,1]$ discretized by a mesh of 43×43 quadrilaterals subdivided into triangles with their diagonals such that $x + y =$ constant and the immersed boundary as described on Figure 9(b). For the present test we set $a = -0.333$ and $b = 0.3333$.

The boundary conditions are applied as follows. On $x = -1$ the Poiseuille inflow is applied (see Equation (3.13)). On $y = 1$, $x = 1$, and Γ, no-slip boundary conditions are applied. On $y = -1$ we impose the do-nothing boundary condition.

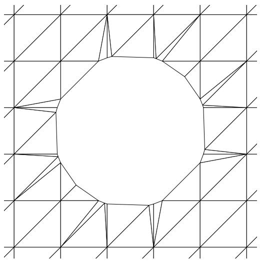

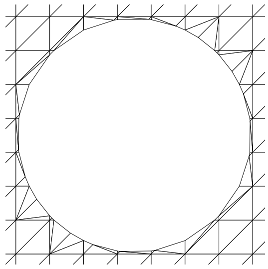

(a) Locally refined with a background mesh 11×11 (b) Locally refined with a background mesh 23×23

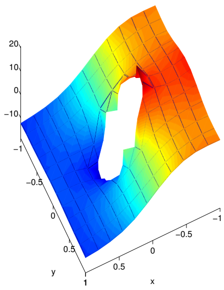

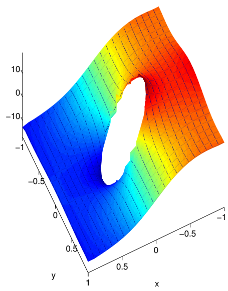

(c) Pressure field $\mathbf{P}_2/P_1$; $\beta_h \approx 0.183$ (d) Pressure field $\mathbf{P}_2/P_1$; $\beta_h \approx 0.182$

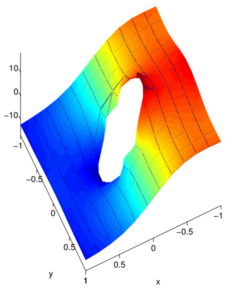

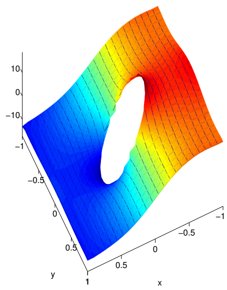

(e) Pressure field $\mathbf{P}_2^+/P_1$; $\beta_h \approx 0.183$ (f) Pressure field $\mathbf{P}_2^+/P_1$; $\beta_h \approx 0.182$

FIGURE 3.11. Effects of distorted elements for two different meshes (11×11) and (23×23). The immersed boundary has a radius of 0.3 and is discretized with 89 linear elements.

Computations show (see Figure 3.12) that the numerical inf-sup constant is smaller for the $\mathbf{P}_2/P_1$ element with $\beta_h \approx 0.054$ than for the $\mathbf{P}_2^+/P_1$ with $\beta_h \approx 0.265$. The numerical inf-sup constant for the $\mathbf{P}_2^+/P_1$ is in the range of the stable cases presented in the SGE-tests (see Section 3.5.1), while for the $\mathbf{P}_2/P_1$ scheme it is an order of magnitude smaller than stable values. We can observe the effect of locking in Figure 12(d) and absence of locking for the $\mathbf{P}_2^+/P_1$ element in Figure 12(f). The culprit is due to a small triangle recessed in the upper right corner (see Figures 12(a) and 12(b)). The locking effect is observed only on a triangle in a small corner with Dirichlet boundary conditions on both edges, thus reflecting the results obtained in the Poiseuille and colliding SGE-tests. In that situation the $\mathbf{P}_2/P_1$ element is unstable for the Poiseuille and colliding Test 2. However, the locking effects are quite small as it can be seen by comparing Figure 12(c) with Figure 12(e). We point out that the peak of pressure for both elements is due to the irregularity of the solution resulting from the L-shaped immersed boundary.

3.5.2.3. *A "surface" flow problem*

In this problem (represented in Figure 9(c)) we consider a "surface" flow, where the surface is described as an immersed boundary. The background mesh is defined on a $[-1,1]\times[-1,1]$ discretized by a mesh of 43×43 quadrilaterals subdivided in triangles with their diagonals such that $x+y=$ constant. The surface Γ is represented by $y = 0.03 - (1/11)\sin(4\pi x)$ and is discretized by 1001 segments. On $x = -1$ and $y = [-1, 0.03]$ we impose $\mathbf{u} = \{(0.03 - x)(1 + x), 0\}^T$. On $y = -1$ and Γ a no-slip boundary condition and on $x = 1$ and $y = [-1, 0.03]$ a do-nothing boundary condition are applied.

For this problem similar results as with the obstacle problem are obtained, that is, a much lower numerical inf-sup constant ($\beta_h \approx 0.064$) is obtained for the $\mathbf{P}_2/P_1$ element than for the $\mathbf{P}_2^+/P_1$ element ($\beta_h \approx 0.208$). The inf-sup values suggest a possible locking effect with the $\mathbf{P}_2/P_1$ element. Indeed, looking at Figure 13(c) a very low pressure value is present (around -80), while such a low pressure is absent in the pressure field with the $\mathbf{P}_2^+/P_1$ element (see Figure 13(e)). Looking at the zooms (Figures 13(d) and 13(f)), we can observe that the very low pressure value for the $\mathbf{P}_2/P_1$ element arises on the upper (small) triangle (see Figure 13(b)), for which, on two of its

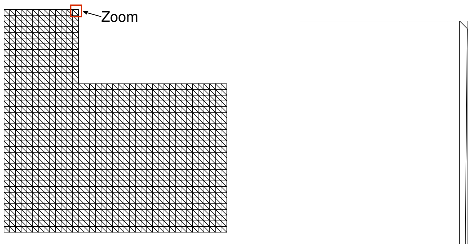

(a) Mesh of 43 × 43 on $[-1,1]^2$.

(b) Zoom.

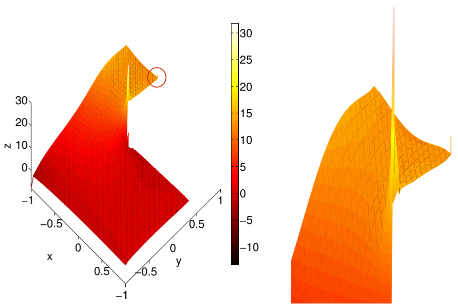

(c) Pressure solution for $\mathbf{P}_2/P_1$; $\beta_h \approx 0.054$.

(d) Zoom on locking effect for the $\mathbf{P}_2/P_1$ element.

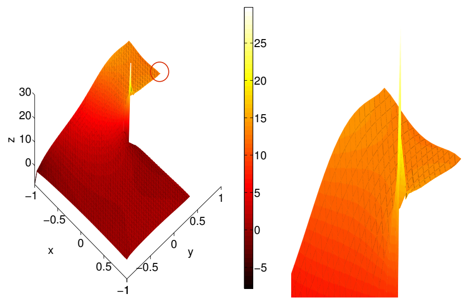

(e) Pressure solution for $\mathbf{P}_2^+/P_1$; $\beta_h \approx 0.265$.

(f) Zoom where no locking effects are visible with the $\mathbf{P}_2^+/P_1$ element.

FIGURE 3.12. Presentation of the "obstacle" problem and results. In particular, locking effects are present for the $\mathbf{P}_2/P_1$ element. We note that it occurs in a small triangle in the corner (see zoom 12(d)) with Dirichlet boundary condition, as in the Poiseuille SGE-test.

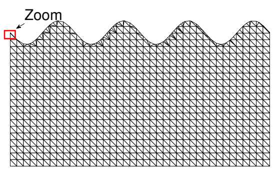

(a) Background mesh with subdivided elements defined by Γ.

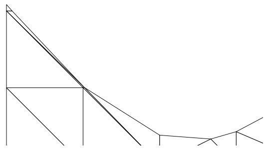

(b) Zoom: a small triangle in the corner with Dirichlet boundary as in the Poiseuille SGE-test.

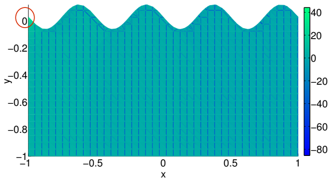

(c) Pressure solution for $\mathbf{P}_2/P_1$; $\beta_h \approx 0.064$.

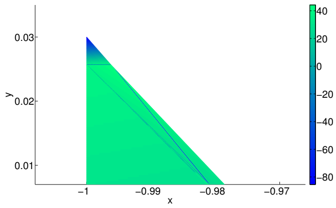

(d) Zoom on locking effect for the $\mathbf{P}_2/P_1$ element.

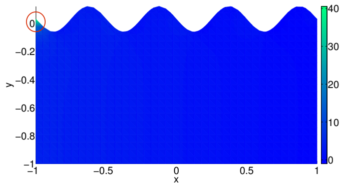

(e) Pressure solution for $\mathbf{P}_2^+/P_1$; $\beta_h \approx 0.208$.

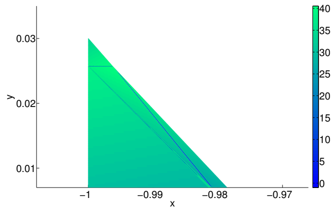

(f) Zoom where no locking effects are visible with the $\mathbf{P}_2^+/P_1$ element.

FIGURE 3.13. Presentation of the mesh and results for the "free surface" flow problem. Locking effects are visible (wrong value (-80) of the pressure on the upper left corner triangle) for the $\mathbf{P}_2/P_1$ scheme and absent for the $\mathbf{P}_2^+/P_1$ scheme.

edges we impose a Dirichlet boundary condition. On the contrary, for the $\mathbf{P}_2^+/P_1$ we obtain a satisfactory value.

3.6. Conclusive considerations for Chapter 3

In this chapter we presented an unfitted grid method, in which the immersed boundary was reconstructed linearly (but the linear reconstruction of the interface is not a restriction of the method). The reconstruction was performed locally (i.e., at the element level) which requires the computation of intersection points with the background mesh. The previously described steps are common to most *eXtended Finite Element Method* (XFEM) implementations. The presented method differs from XFEM since each element intersected by the immersed boundary were subdivided into subelements on which we reconstructed a finite element basis, as in a refined approach. The advantages are twofold. Firstly, we obtain an accurate representation of the immersed boundary. Secondly, it is very easy to impose Dirichlet boundary condition on the immersed boundary. But, that subdivision may induce highly distorted elements. In this chapter, we focused on the case of the $\mathbf{P}_2/P_1$ element and pointed out its defects; in particular, we show that for our application the $\mathbf{P}_2/P_1$ scheme may not be inf-sup stable when elements are highly distorted. Numerical investigations showed that locking effects may occur on distorted elements in corners for which Dirichlet boundary conditions are imposed on both sides. Therefore, the stability of the element may be guaranteed for a large class of problems, but not for all as showed. Nevertheless, we presented a solution which consists in enriching the velocity space with a bubble (named herein $\mathbf{P}_2^+/P_1$). It was shown numerically that such a finite element scheme is inf-sup stable in all presented tests.

CHAPTER 4

A locally anisotropic fluid-structure interaction remeshing strategy for thin structures with application to a hinged rigid leaflet

4.1. Introduction

A classical approach for the numerical simulation of fluid-structure interaction is the Arbitrary Lagrangian Eulerian (ALE) method (see, e.g., [**39**] and references therein). It is well known that this method may not be adequate when the structure undergoes large deformations. In this case, alternatives are provided by the so-called "immersed" approaches, also known under the name of Immersed Boundary Method (see, e.g., [**81**] or [**59**]), Fictitious Domain (see, e.g., [**52**]), embedded/unfitted (see, e.g., [**97**]), etc. In these methods, on the contrary to the ALE method, the fluid mesh is given *a-priori* and independently of the location of the structure.

Many immersed approaches are known for lacking of accuracy with respect to the ALE method (see, e.g., [**92**] and references therein). The loss of accuracy is in general due to the non conformity of the fluid/solid meshes and/or an inaccurate enforcement of the coupling constraints. Accordingly, many researches in the last decade have focused on developing accurate immersed approaches and today we may distinguish two types of accurate strategies: iterative ones (see, e.g., [**74**] and [**44**]) and direct strategies. Among the latter, we mention the Immersed Interface Method (see, e.g., [**70**]), the eXtended Finite Element Method (XFEM) (see, e.g., [**48**]), and a local refinement strategy (see, e.g., [**61**] or [**91**]). The present work collocates within the latter direct strategy, i.e., the local refinement.

In particular, the presented method shares similarities with the eXtended finite element method, which consists in constructing a finite element basis able to accurately resolve the singularities introduced by the structure. A major difficulty of the eXtended finite element method is to enforce the fluid/solid interface constraints. This issue has recently been an important field of research (see, e.g., **[55]** or **[33]** and references therein). Differently, the local refinement approach consists in locally refining the initial fluid mesh such that it conforms with the solid mesh. The method avoids a complex implementation and, thanks to conformity, the fluid/structure interface constraints may directly be enforced in the finite element spaces. In **[91]** a smoothing strategy is used to maintain a relative isotropy of the refined mesh. One of the drawbacks of this approach is that the more the isotropy of the refined mesh is guaranteed, the more the refined mesh is modified with respect to the original mesh. On the contrary, in **[61]** the original mesh is used without changing its topology (i.e., only elements cut by the immersed structure are modified). However, the present strategy employ anisotropic elements and, therefore, we talk of a *locally anisotropic remeshing* approach.

Since our problem consists of incompressible fluids and that our method of choice to solve them is the mixed finite elements, we have to deal at the same time with mixed finite elements and anisotropic elements. The combination of the two leads to two major issues: an ill-conditioned linear system (issue possibly already present in the standard finite element method with anisotropic elements) and a possible lack of inf-sup stability even for mixed elements that are inf-sup stable on isotropic meshes. We point out that in **[61]** a streamline upwind Petrov Galarkin scheme with low order elements is used and it is known to help circumventing the inf-sup condition on distorted meshes (see, e.g., **[73]** or **[76]**). In the present work we focus on solving the inf-sup stability issue with higher order elements. In addition, we also discuss the linear system ill-conditioning.

The present work takes inspiration from **[61]**, where: i) only the elements crossed by the solid are remeshed so to fit with the immersed boundary; ii) lower order elements are used to ensure that no additional degrees of freedom result from the remeshing strategy; and iii) the nodes lying on the immersed boundary are not considered as degrees of freedom, precluding strongly coupled strategies. Instead, we want to have the freedom of using high order elements, so to avoid stabilization of the inf-sup condition, and of using strongly coupled strategies; we thus do not eliminate the nodes on the internal boundary. In [**8**] it is investigated the use of the $\mathbf{P}_2/P_1$ element for a 2D steady incompressible Stokes problem using the locally anisotropic remeshing strategy and it was shown that $\mathbf{P}_2/P_1$ may not be inf-sup stable with triangles in corners with Dirichlet boundary conditions applied on both edges, but that adding a bubble to the velocity space stabilizes $\mathbf{P}_2/P_1$ with the present remeshing strategy. Furthermore, the gradient of the velocity and the pressure of the fluid are discontinuous across the structure, and thus it may be convenient to use mixed finite elements with element-wise discontinuous pressures, as used in [**91**] and for this reason we study two such elements: $\mathbf{P}_2/P_0$ and $\mathbf{P}_2^+/P_1^d$ with constant and linear pressures, respectively. However, as we shall see these two elements have inf-sup related issues on anisotropic meshes and thus we also use the mixed finite elements studied in [**8**] namely $\mathbf{P}_2/P_1$ and $\mathbf{P}_2^+/P_1$ but in such a way that the pressure is discontinuous across the solid.

Finally, in terms of the fluid-solid interaction scheme, we use a strongly coupled one within a time advancing implicit Euler scheme such that added mass effects are avoided (see, e.g., [**31**]).

4.2. Continuous problem

4.2.1. The fluid problem

For the fluid, a standard Newtonian model with constant density is adopted. Therefore, the set of equations governing the motion of the fluid is given by the classical incompressible Navier-Stokes equations:

$$\left\{ \begin{array}{l} \rho_f \left(\dfrac{\partial \mathbf{u}}{\partial t} + \mathbf{u} \cdot \nabla \mathbf{u} \right) - \mathbf{div}(\mu \nabla^s \mathbf{u}) + \nabla p - \mathbf{f} = \mathbf{0}, \\ \mathrm{div}\,(\mathbf{u}) = 0, \end{array} \right. \tag{4.1}$$

where ρ_f designates the density, μ the dynamic viscosity, $\mathbf{u}$ the velocity, p the pressure and $\nabla^s \mathbf{u}$ is defined as $\nabla^s \mathbf{u} = \nabla \mathbf{u} + (\nabla \mathbf{u})^T$.

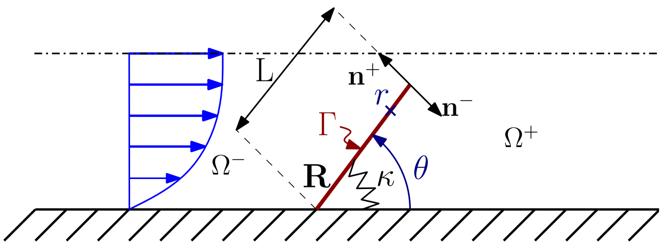

FIGURE 4.1. An example of a hinged rigid leaflet sets in motion by an unsteady fluid.

4.2.1.1. *Boundary and initial conditions*

We consider Eq. (4.1) in a fixed domain Ω with $\partial\Omega = \Sigma_D \cup \Sigma_N$ such that $\Sigma_D \cap \Sigma_N = \emptyset$, completed by the following boundary and initial conditions:

$$\begin{cases} \mathbf{u} = \mathbf{b}_D & \text{on } \Sigma_D, \\ -p\mathbf{n} + \mu(\nabla^s \mathbf{u})\mathbf{n} = \mathbf{b}_N & \text{on } \Sigma_N, \end{cases} \tag{4.2}$$

$$\mathbf{u}(\mathbf{x}, 0) = \mathbf{u}_i(\mathbf{x}) \qquad \text{on } \Omega, \tag{4.3}$$

where $\mathbf{n}$ designates the outward normal of $\partial\Omega$. We assume that Σ_N is not empty such that the pressure is uniquely defined.

4.2.2. The solid problem

For the solid we choose a hinged rigid leaflet of length L with negligible width, only one rotational degree of freedom, and a rotational spring to the leaflet (see Fig. 4.1).

For describing the motion of the leaflet we use a polar coordinate system with pole $\mathbf{R} \in \mathbb{R}^2$, the point of rotation of the leaflet. We denote by θ and r the angular and radial coordinates, respectively.

The leaflet is initially at θ_0 and has a constant mass distribution. The leaflet equation is thus given by

$$I\frac{d^2\theta}{dt^2} + \kappa\,(\theta - \theta_0) = \tau, \tag{4.4}$$

where τ is the torque exerted on the bar, defined as

$$\tau(t) = \int_\Gamma r f_s(r,t)\mathrm{d}r, \tag{4.5}$$

with f_s the net balance of the stress acting on the two sides of the bar (see Fig. 4.1), κ the spring torsional elastic modulus, and I the moment of inertia (for a bar) with a constant linear density ρ_s given by

$$I = \int_\Gamma \rho_s r^2 \mathrm{d}r = \frac{\rho_s L^3}{3}.$$

4.2.3. Fluid-structure interaction coupling

The coupling between the fluid and the solid is exerted by the fulfillment of the kinematic constraint

$$\mathbf{u} = r\frac{d\theta}{dt}\mathbf{n}^+, \tag{4.6}$$

and the conservation of momentum

$$f_s(\theta, t) = P^- - P^+,$$

where the right hand side is the drop of pressure across the solid. Defining

$$\begin{cases} P^+\mathbf{n}^+ & = -p^+\mathbf{n}^+ + \mu(\nabla^s\mathbf{u}^+)\mathbf{n}^+, \\ P^-\mathbf{n}^- & = -p^-\mathbf{n}^- + \mu(\nabla^s\mathbf{u}^-)\mathbf{n}^-, \end{cases}$$

we obtain that

$$f_s(\theta, t) = [\![p\mathbf{n}^+ - \mu(\nabla^s\mathbf{u})\mathbf{n}^+]\!]_\Gamma \cdot \mathbf{n}^+ \tag{4.7}$$

where symbol $[\![\cdot]\!]$ denotes the jump across Γ, i.e.,

$$[\![p\mathbf{n}^+ - \mu(\nabla^s\mathbf{u})\mathbf{n}^+]\!]_\Gamma = (p_{|\Gamma^+} - p_{|\Gamma^-})\mathbf{n}^+ - \mu(\nabla^s(\mathbf{u}_{|\Gamma^+} - \mathbf{u}_{|\Gamma^-}))\mathbf{n}^+,$$

with $v_{|\Gamma}$ the trace of v on Γ.

4.3. Time discretization and linearization

For the fluid we use the first order backward Euler scheme to discretize the velocity time derivative, that is

$$\left.\frac{\partial\mathbf{u}}{\partial t}\right|_{t^{n+1}} \approx \frac{\mathbf{u}^{n+1} - \mathbf{u}^n}{\delta t}, \tag{4.8}$$

where δt is the time step. We also choose the velocity at the previous time step as the convective velocity, according to the classical Picard approach such that the convective term in Eq. (4.1) is given by

$$(\mathbf{u}\cdot\nabla\mathbf{u})_{t^{n+1}} \approx \mathbf{u}^n \cdot \nabla\mathbf{u}^{n+1}, \tag{4.9}$$

leading to a first-order in time scheme.

For the solid we employ a centered scheme for the acceleration, that is

$$\left.\frac{d^2\theta}{dt^2}\right|_{t^{n+1}} \approx \frac{\theta^{n+1} - 2\theta^n + \theta^{n-1}}{\delta t^2}, \tag{4.10}$$

and for the velocity we use a backward Euler scheme, that is:

$$\left.\frac{d\theta}{dt}\right|_{t^{n+1}} \approx \frac{\theta^{n+1} - \theta^n}{\delta t}. \tag{4.11}$$

4.3.1. Strong formulation of the coupled problem

Using Eq. (4.8)-(4.11) in Eq. (4.1)-(4.7), the time discretized problem in strong form reads:

Problem 2: Given $\mathbf{f}^{n+1}$, $\mathbf{b}_D^{n+1}$, $\mathbf{b}_N^{n+1}$, $\mathbf{u}^n$, θ^n, and θ^{n-1}, find $\mathbf{u} = \mathbf{u}^{n+1}$, $p = p^{n+1}$, $\theta = \theta^{n+1}$ such that

$$\begin{cases} \rho_f \left(\dfrac{\mathbf{u}}{\delta t} + \mathbf{u}^n \cdot \nabla \mathbf{u}\right) - \mathbf{div}(\mu \nabla^s \mathbf{u}) + \nabla p \\ \qquad = \mathbf{f}^{n+1} + \rho_f \dfrac{\mathbf{u}^n}{\delta t} \end{cases} \quad \text{in } \Omega \backslash \Gamma^n \tag{4.12a}$$

$$\operatorname{div}(\mathbf{u}) = 0 \quad \text{in } \Omega \tag{4.12b}$$

$$\mathbf{u} = \mathbf{b}_D^{n+1} \quad \text{on } \Sigma_D \tag{4.12c}$$

$$-p\mathbf{n} + \mu(\nabla^s \mathbf{u})\mathbf{n} = \mathbf{b}_N^{n+1} \quad \text{on } \Sigma_N \tag{4.12d}$$

$$\mathbf{u} - r\frac{\theta}{\delta t}\mathbf{n}^+ = -r\frac{\theta^n}{\delta t}\mathbf{n}^+ \quad \text{on } \Gamma^n \tag{4.12e}$$

$$\tau^{n+1} = \int_{\Gamma^n} r[\![p\mathbf{n}^+ - \mu(\nabla^s \mathbf{u})\mathbf{n}^+]\!] \cdot \mathbf{n}^+ \mathrm{d}r, \tag{4.12f}$$

$$I\frac{\theta}{\delta t^2} + \kappa\theta - \tau^{n+1} = \kappa\theta_0 + 2I\frac{\theta^n}{\delta t^2} - I\frac{\theta^{n-1}}{\delta t^2}. \tag{4.12g}$$

Notice that we impose the coupling between the fluid and the solid on Γ at time n, denoted by Γ^n. Indeed, the position of the leaflet at time $n+1$ is an unknown of the problem and enforcing the coupling on Γ^n is coherent with our choice for the time stepping, i.e., a first-order in time scheme.

4.3.2. Weak formulation of the coupled problem

We consider the classical Sobolev spaces; accordingly $L^2(\Omega)$ denotes the space of square summable functions in Ω, $H^1(\Omega)$ is the space of functions that are in $L^2(\Omega)$ with first derivatives in $L^2(\Omega)$. The space $H^1_\Sigma(\Omega)$ denotes the space of functions in $H^1(\Omega)$ with vanishing traces on Σ_D and $H^{1,n}_{\Sigma,\Gamma}(\Omega)$ is the space of functions in $H^1(\Omega)$ with vanishing trace on $\Sigma_D \cup \Gamma^n$.

For simplicity and without loss of generality, let assume that $\mathbf{b}_D = \mathbf{0}$ (see Eq. (4.2)), and thus only the essential interfacial constraints are imposed on Γ^n such that we have the lifting of the interfacial constraints defined as $\mathbf{g}^{n+1} \in \left[H^1_\Sigma(\Omega)\right]^2$ and $\mathbf{u}_0^{n+1} \in \left[H^{1,n}_{\Sigma,\Gamma}(\Omega)\right]^2$ has a null trace on Γ^n with

$$\mathbf{u}^{n+1} = \mathbf{u}_0^{n+1} + \mathbf{g}^{n+1}, \tag{4.13}$$

where $\mathbf{g}^{n+1}_{|\Gamma^n} = (r(\theta^{n+1} - \theta^n)/\delta t)\mathbf{n}^+$ (see Eq. 4.12e). Then our weak formulation for Problem 2 reads:

Problem 3: Given $\mathbf{f}^{n+1}$, $\mathbf{b}_N^{n+1}$, $\mathbf{u}^n$, θ^n, θ^{n-1}, find $\mathbf{u}_0 = \mathbf{u}_0^{n+1} \in [H^{1,n}_{\Sigma,\Gamma}(\Omega)]^2$, $p = p^{n+1} \in L^2(\Omega)$, and $\theta = \theta^{n+1} \in \mathbb{R}$, such that $\forall(\mathbf{v}, q, \gamma) \in [H^{1,n}_{\Sigma,\Gamma}(\Omega)]^2 \times L^2(\Omega) \times \mathbb{R}$ we have

$$\begin{cases} \displaystyle\int_\Omega \rho_f \left(\frac{\mathbf{u}_0}{\delta t} + \mathbf{u}^n \cdot \nabla \mathbf{u}_0\right) \cdot \mathbf{v} + \int_\Omega \mu \nabla^s \mathbf{u}_0 : \nabla \mathbf{v} - \int_\Omega p \operatorname{div}(\mathbf{v}) \\ \displaystyle\qquad + \int_\Omega \rho_f \left(\frac{\mathbf{g}}{\delta t} \mathbf{u}^n \cdot \nabla \mathbf{g}\right) \cdot \mathbf{v} + \int_\Omega \mu \nabla^s \mathbf{g} : \nabla \mathbf{v} \\ \displaystyle\qquad = \int_\Omega \mathbf{f}^{n+1} \cdot \mathbf{v} + \int_\Omega \rho_f \frac{\mathbf{u}^n}{\delta t} \cdot \mathbf{v} + \int_{\Sigma_N} \mathbf{b}_N^{n+1} \cdot \mathbf{v} \end{cases} \tag{4.14a}$$

$$-\int_\Omega q \operatorname{div}(\mathbf{u}_0) - \int_\Omega q \operatorname{div}(\mathbf{g}) = 0 \tag{4.14b}$$

$$\tau^{n+1} = \int_{\Gamma^n} r \left(\llbracket p\mathbf{n}^+ - \mu(\nabla^s \mathbf{g})\mathbf{n}^+ \rrbracket\right) \cdot \mathbf{n}^+ \mathrm{d}r \tag{4.14c}$$

$$\mathbf{g}_{|\Gamma^n} = (r(\theta - \theta^n)/\delta t)\mathbf{n}^+, \tag{4.14d}$$

$$\left(I\frac{\theta}{\delta t^2} + \kappa\theta - \tau^{n+1}\right)\gamma = \left(\kappa\theta_0 + 2I\frac{\theta^n}{\delta t^2} - I\frac{\theta^{n-1}}{\delta t^2}\right)\gamma. \tag{4.14e}$$

4.4. Locally anisotropic remeshing strategy and finite elements

This section is devoted to the construction of a partition $\mathcal{T}^n$ of Ω based on an initial partition $\mathcal{T}$ of Ω, which is given independently of the position of the leaflet, as well as the associated finite element spaces. The construction of $\mathcal{T}^n$ is built upon a locally anisotropic remeshing. A more detailed presentation of the locally anisotropic remeshing strategy is given in Chapter 3 but we give here a short presentation of the remeshing with additional considerations for the tip of the leaflet. Furthermore, for the problem in mind the partition $\mathcal{T}^n$ is built in such a way that it is fairly easy to:

(1) enforce the kinematic constraint between the fluid and the solid, and
(2) construct finite element spaces with discontinuous pressures and velocity derivatives across the solid.

Moreover, since we use high order finite elements for the velocity field and a local remeshing we explain how we interpolate the values of the velocity field computed at previous time steps on several nodes of the remeshed mesh. We then give a discrete formulation of Problem 3. Moreover, since we use high order finite elements and a local remeshing strategy, some nodal values of the velocity field, on the initial mesh, are not directly known from computation at time $n+1$, and thus we have to interpolate, which we explain. Finally, we summarize in the form of an algorithm all previously discussed steps. Next section, Section 4.5 is then devoted to the algebraic formulation of the problem.

4.4.1. Locally anisotropic remeshing

We start by an isotropic triangulation $\mathcal{T}$ of Ω given independently of the position of the leaflet at time n (see, e.g., [**40**] for a definition of an isotropic mesh (named there a shape regular mesh) and [**65**] for a discussion on shape assumptions for triangular meshes). The strategy employed is to refine the initial mesh solely on elements crossed by the solid. As often requested in the literature (see, e.g., [**54**]), we assume that Γ^n intersects twice the boundary of a triangle from $\mathcal{T}$ and that it crosses two of the triangle edges. We call it a *full-cut*. As pointed out in [**54**], given any solid geometry, there always exists a sufficiently fine fluid mesh such that the assumptions previously discussed are satisfied. Importantly, we add to the full-cut assumptions that we also accept Γ^n to cut only once a triangle boundary for the tip of the leaflet, called a *tip-cut* (see Fig. 4.2).

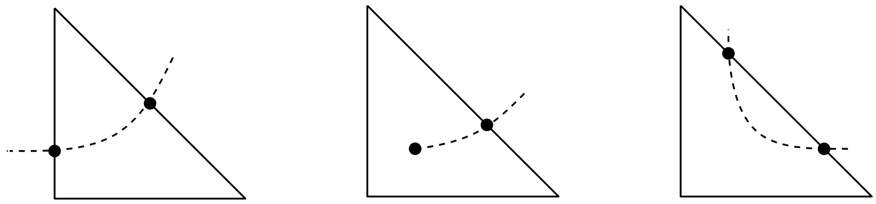

Full-cut Tip-cut Invalid-cut

FIGURE 4.2. Mesh assumptions with respect to Γ^n (dashed).
Full and tip cuts are the only two admissible ones.

Now that we have the intersection points of Γ^n with the edges of the elements of $\mathcal{T}$ we can remesh. We recall that by hypothesis Γ^n crosses a triangle boundary of $\mathcal{T}$ on two points for a full-cut, each point belonging to a distinct edge, or only once for a tip-cute. For each element of $\mathcal{T}$ crossed by Γ^n we consider a Delaunay triangulation of the set of points composed by the vertices of the triangle and the two intersection points for a full-cut or the single intersection point and the tip of the leaflet for a tip-cut (see Fig. 4.3). We call this remeshing a *sub-triangulation*. We point out that a Delaunay triangulation maximizes the minimal angles (see, e.g., [**18**]).

We now can construct a new partition denominated $\mathcal{T}^n$ that consists of all triangles of $\mathcal{T}$ that are not crossed by Γ^n and the triangles of the sub-triangulation of all the elements cut by Γ^n. We define the remeshed partition by $\Omega_h^n = \bigcup_k T_k$ where T_k is a triangle of $\mathcal{T}^n$. As opposed to $\mathcal{T}$, notice that $\mathcal{T}^n$ is not in general isotropic. It has been noted in [**11**] that an isotropic partition is not a necessary assumption for the optimal convergence of the finite element method. However, the distortion of the mesh affects the conditioning of the system (see, e.g., [**63**]). In Section 4.6 we will discuss these topics in more details.

It is interesting to observe that using the partition $\mathcal{T}^n$ we can easily enforce the kinematic constraints on Γ^n since we have nodes of $\mathcal{T}^n$ lying on Γ^n. Furthermore, across Γ^n the stress may jump, which means that we have a discontinuous pressure and a discontinuity in the derivatives of the velocity that have to be properly taken into account. With $\mathcal{T}^n$ a pressure

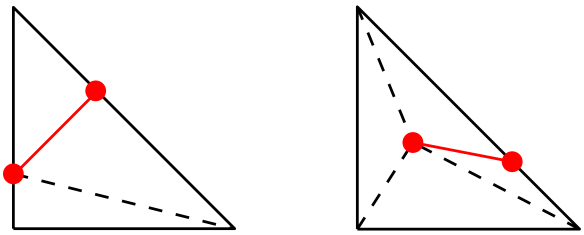

(a) Full-cut sub-triangulation: subdivided into 3 subtriangles.

(b) Tip-cut sub-triangulation: subdivided into 4 subtriangles

FIGURE 4.3. Spatial discretization: full and tip triangle subdivisions.

basis that allows a jump across Γ_h^n is promptly constructed, while the jump in the derivatives of the velocity is automatically managed by standard nodal C^0-Lagrange basis.

4.4.2. Choice of the finite element spaces

Anisotropic partitions may impact adversely inf-sup stability of mixed finite elements. In this section we introduce the various mixed finite elements used in the numerical tests and we discuss their inf-sup stability in the context of the present method. More details are given in the numerical tests section.

We use two pressure implementations:

(1) Element-wise discontinuous pressure that intrinsically allows jumps in the pressure across element edges. Indeed, the pressure is in L^2 and thus discontinuous elements are allowed;
(2) "Continuous" pressure that are continuous everywhere in the fluid domain, except across the immersed boundary since we wish to allow the pressure to jump across the leaflet. Obviously, such an element is harder to implement and it requires additional degrees of freedom along the structure and thus in the pressure finite element space.

Accordingly to the previous discussion, in the present work we consider the following mixed approximation schemes:

a. $\mathbf{P}_2/P_0$: continuous piecewise quadratic velocity and piecewise constant pressure:

$$\begin{cases} \mathbf{V}_{h,\Gamma}^{n+1} & = \{\mathbf{v} : \mathbf{v}_{|T} \in (\mathcal{P}_2)^2, \forall T \in \mathcal{T}^n\} \cap [H_{\Sigma,\Gamma}^{1,n}(\Omega)]^2, \\ Q_h^{n+1} & = \{q : q_{|T} \in \mathcal{P}_0, \forall T \in \mathcal{T}^n\} \cap L^2(\Omega). \end{cases}$$

Here $\mathcal{P}_k$ denotes the space of polynomials of order k.

b. $\mathbf{P}_2^+/P_1^d$: continuous piecewise quadratic with a cubic bubble velocity and discontinuous piecewise linear pressure:

$$\begin{cases} \mathbf{V}_{h,\Gamma}^{n+1} & = \{\mathbf{v} : \mathbf{v}_{|T} = \mathbf{v}_{|T}^2 + \mathbf{v}_{|T}^+;\ \mathbf{v}_{|T}^1 \in (\mathcal{P}_2)^2, \\ & \qquad \mathbf{v}_{|T}^+ \in (\mathcal{P}_3)^2, \mathbf{v}_{|\partial T}^+ = \mathbf{0}, \forall T \in \mathcal{T}^n\} \cap [H_{\Sigma,\Gamma}^{1,n}(\Omega)]^2 \\ Q_h^{n+1} & = \{q : q_{|T} \in \mathcal{P}_1, \forall T \in \mathcal{T}^n\} \cap L^2(\Omega), \end{cases}$$

c. $\mathbf{P}_2/P_1$: (Hood-Taylor) continuous piecewise quadratic velocity and continuous piecewise linear pressure but discontinuous across the structure:

$$\begin{cases} \mathbf{V}_{h,\Gamma}^{n+1} & = \{\mathbf{v} : \mathbf{v}_{|T} \in (\mathcal{P}_2)^2, \forall T \in \mathcal{T}^n\} \cap [H_{\Gamma,\Sigma}^{1,n}(\Omega)]^2 \\ Q_h^{n+1} & = \{q : q_{|T} \in \mathcal{P}_1, \forall T \in \mathcal{T}^n\} \cap \{H^1(\Omega \backslash \Gamma^n) \cap L^2(\Omega)\}. \end{cases}$$

d. $\mathbf{P}_2^+/P_1$: continuous piecewise quadratic with a cubic bubble velocity and continuous piecewise linear pressure but discontinuous across the structure:

$$\begin{cases} \mathbf{V}_{h,\Gamma}^{n+1} & = \{\mathbf{v} : \mathbf{v}_{|T} = \mathbf{v}_{|T}^2 + \mathbf{v}_{|T}^+;\ \mathbf{v}_{|T}^1 \in (\mathcal{P}_2)^2, \\ & \qquad \mathbf{v}_{|T}^+ \in (\mathcal{P}_3)^2, \mathbf{v}_{|\partial T}^+ = \mathbf{0}, \forall T \in \mathcal{T}^n\} \cap [H_{\Sigma,\Gamma}^{1,n}(\Omega)]^2 \\ Q_h^{n+1} & = \{q : q_{|T} \in \mathcal{P}_1, \forall T \in \mathcal{T}^n\} \cap \{H^1(\Omega \backslash \Gamma^n) \cap L^2(\Omega)\}. \end{cases}$$

For a general and detailed presentation of the previously presented finite element spaces and an extensive presentation of the theory on mixed finite elements see [**22**].

One of the major issues for mixed elements on anisotropic mesh is that the inf-sup constant, indicated in the following with β, may degenerate to zero for highly anisotropic elements. The effects of a very low inf-sup constant are twofold. Firstly, the velocity and the pressure fields may have a very large bound, of $\mathcal{O}(\beta^{-1})$ and $\mathcal{O}(\beta^{-2})$, respectively. Secondly, the conditioning of the system is affected since dependence of the condition number of the Schur complement for the steady incompressible Stokes problem on β is $\mathcal{O}(\beta^{-2})$ (see, e.g., [**22**] or [**40**]). We point out that the conditioning of the Schur complement is also affected by the distortion of the elements even for inf-sup stable elements on anisotropic meshes (see Proposition 4.47 in [**42**]) since the conditioning of the pressure mass matrix worsens as the elements are more distorted.

We now provide the various results on distorted meshes regarding the mixed finite elements used in this work.

a. $\mathbf{P}_2/P_0$: We know from [**4**] that $\mathbf{P}_2/P_0$ is stable on a large class of distorted meshes. Despite these results, using a similar study as performed in Chapter 3, it may be shown that $\mathbf{P}_2/P_0$ can be unstable with anisotropic elements and not only in corners (see Appendix C).
b. $\mathbf{P}_2^+/P_1^d$: To the best knowledge of the authors there are no results for this element. Nevertheless, we show that $\mathbf{P}_2^+/P_1^d$ (which is used in [**91**]) is highly unstable on anisotropic elements, as we shall see in the numerical tests (see Appendix C).
c. $\mathbf{P}_2/P_1$: It has been shown numerically in [**5**] that $\mathbf{P}_2/P_1$ may fail on distorted meshes while $\mathbf{P}_2^+/P_1$ passes all proposed tests. In Chapter 3 it has been shown numerically that, for a similar method as proposed in the present document but for the steady 2D incompressible Stokes problem, $\mathbf{P}_2/P_1$ may fail on triangles in corners for which Dirichlet boundary conditions are applied on both boundary edges. Actually such a situation is unlikely to occur for our FSI problem, except perhaps for refined elements near the point of rotation of the leaflet. Nevertheless, no spurious modes are seen in our numerical tests with that element.

d. $\mathbf{P}_2^+/P_1$: On the contrary to $\mathbf{P}_2/P_1$, and as suggested from the results in [**5**], the $\mathbf{P}_2^+/P_1$ element passes all tests. For that reason, $\mathbf{P}_2^+/P_1$ is our element of choice. However, no formal proof of the stability of $\mathbf{P}_2^+/P_1$ on anisotropic meshes is known to the authors.

We point out that, when a mixed element is inf-sup unstable, the effect of the spurious modes are only local and on very small elements, which may have a limited impact on the motion of the leaflet, as obtained in the numerical tests. The rigidity of the leaflet may also play an important role in this. However, among all tested mixed elements, the best and safest is $\mathbf{P}_2^+/P_1$ (see also implementation considerations in Remark 19).

REMARK 19. *In the current implementation we add the bubble over the whole mesh. However, a more computationally efficient approach would be to add the bubble only on the distorted elements. Furthermore, for* $\mathbf{P}_2^+/P_1$ *it is not necessary to integrate exactly all polynomial degrees higher than those present using* $\mathbf{P}_2/P_1$ *(i.e., terms involving the bubble shape functions), making it a competitive alternative to* $\mathbf{P}_2/P_1$ *(see Chapter 3).*

4.4.3. Previous time step velocity interpolation

In Problem 3 (see Eq. (4.14)), two velocity terms at time n are required, but some nodal values in the neighborhood of the structure are unknown with respect to the velocity solution over the initial mesh $\mathcal{T}$ (see Fig. 4.4).

In order to compute the missing values we build the quadratic interpolator $\mathbf{\Pi}$ over $\mathcal{T}$, i.e., over the initial mesh. Let $\mathbf{V}_h$ be the finite dimensional subspace of $[H^1(\Omega)]^2$ built over $\mathcal{T}$ using piecewise quadratic Lagrange shape functions (each shape function is denoted by $\mathbf{N}_i$) such that $\mathbf{V}_h = \text{span}(\mathbf{N})$. More precisely, we assume that we know $\hat{\mathbf{u}}^n$, i.e., the velocity nodal values at time t^n over the mesh Ω_h, and thus the interpolation $\mathbf{\Pi}\mathbf{u}^n$ is defined by $\mathbf{\Pi}\mathbf{u}^n(\mathbf{x}) = \sum_i \hat{\mathbf{u}}_i^n \mathbf{N}_i(\mathbf{x})$.

REMARK 20. *The use of the interpolant introduces an error. In particular,* $\mathbf{\Pi}\mathbf{u}^n(\mathbf{x}^n)$ *is not divergence free in general. Such an issue is well known. However, as pointed out in* [**91**]*, the error introduced is found to be small. We point out that the issue could be avoided for the convective term resorting to*

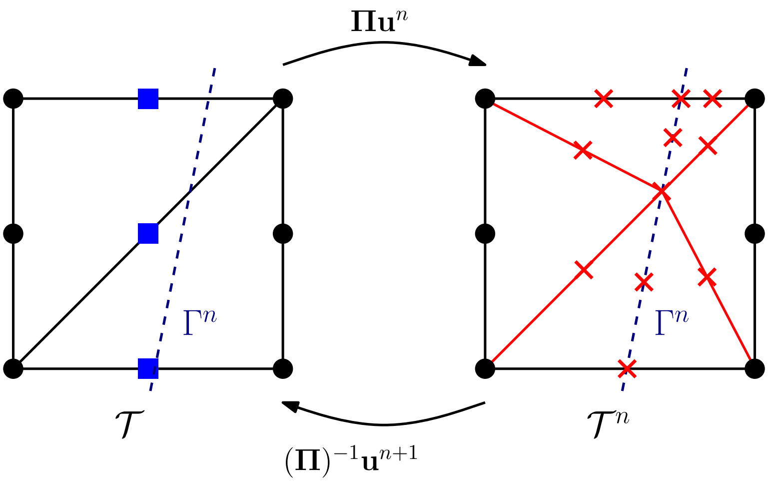

FIGURE 4.4. The solution $\mathbf{u}^n$ is required for computing $\mathbf{u}^{n+1}$ but some nodal values are unknown on $\mathcal{T}^n$. They are depicted by red crosses. Hence interpolation is necessary using $\mathbf{\Pi}$ assuming that we know $\mathbf{u}^n$ on $\mathcal{T}$ (discussed in Sec. 4.4.3). In the same manner from the mesh $\mathcal{T}$ some nodal values of the solution $\mathbf{u}^{n+1}$ are unknown (depicted with a blue square), and thus interpolation using $(\mathbf{\Pi})^{-1}$ is required (discussed in Sec. 4.4.5) in order to obtain all nodal values on $\mathcal{T}$ of $\mathbf{u}^{n+1}$.

a full implicit strategy by using $\mathbf{u}_h^{n+1} \cdot \nabla \mathbf{u}_h^{n+1}$ instead of $\mathbf{\Pi u}_h^n(\mathbf{x}^{n+1}) \cdot \nabla \mathbf{u}_h^{n+1}$. However, such a strategy has not been tested here.

4.4.4. Discrete problem

Now using the elements defined in Sec. 4.4.2, we build finite dimensional spaces $\mathbf{V}_{h,\Gamma}^{n+1}$ and $\mathbf{Q}_h^{n+1}$ such that $\mathbf{V}_{h,\Gamma}^{n+1} \subset [H_{\Sigma,\Gamma}^{1,n}(\Omega)]^2$ and $\mathbf{Q}_h^{n+1} \subset L^2(\Omega)$. It follows that the discretized problem is given by:

Problem 4: Given $\mathbf{f}^{n+1}$, $\mathbf{b}_N^{n+1}$, $\mathbf{u}_h^n$, θ^n, θ^{n-1}, find $\mathbf{u}_{0,h} = \mathbf{u}_{0,h}^{n+1} \in \mathbf{V}_{h,\Gamma}^{n+1}$, $p_h = p_h^{n+1} \in Q_h^{n+1}$, and $\theta = \theta^{n+1} \in \mathbb{R}$, such that $\forall(\mathbf{v}_h, q_h, \gamma) \in \mathbf{V}_{h,\Gamma}^{n+1} \times Q_h^{n+1} \times \mathbb{R}$ we have

$$\begin{cases} \displaystyle\int_{\Omega_h^n} \rho_f \left\{ (\mathbf{u}_{0,h} + \mathbf{g}_h)/\delta t + \mathbf{\Pi}\mathbf{u}^n \cdot \nabla (\mathbf{u}_{0,h} + \mathbf{g}_h) \right\} \cdot \mathbf{v}_h \\ \displaystyle + \int_{\Omega_h^n} \mu \nabla^s (\mathbf{u}_{0,h} + \mathbf{g}_h) : \nabla \mathbf{v}_h - \int_{\Omega_h^n} p_h \operatorname{div}(\mathbf{v}_h) \\ \displaystyle = \int_{\Omega_h^n} \left(\mathbf{f}^{n+1} + \rho_f \mathbf{\Pi}\mathbf{u}^n/\delta t \right) \cdot \mathbf{v}_h + \int_{\Sigma_N} \mathbf{b}_N^{n+1} \cdot \mathbf{v}_h \end{cases} \tag{4.15a}$$

$$- \int_{\Omega_h^n} q_h \operatorname{div}(\mathbf{u}_{0,h}) - \int_{\Omega_h^n} q_h \operatorname{div}(\mathbf{g}_h) = 0 \tag{4.15b}$$

$$\tau^{n+1} = \int_{\Gamma^n} r \left([\![p_h \mathbf{n}^+ + \mu(\nabla^s \mathbf{g}_h)\mathbf{n}^+]\!] \right) \cdot \mathbf{n}^+ \mathrm{d}r \tag{4.15c}$$

$$\mathbf{g}_{h|\Gamma^n} = (r(\theta - \theta^n)/\delta t)\mathbf{n}^+. \tag{4.15d}$$

$$\left(I \frac{\theta}{\delta t^2} + \kappa\theta - \tau^{n+1} \right) \gamma = \left(\kappa\theta_0 + 2I\frac{\theta^n}{\delta t^2} - I\frac{\theta^{n-1}}{\delta t^2} \right) \gamma \tag{4.15e}$$

4.4.5. Velocity "re"-interpolation for the initial mesh

When using a linear interpolant, all nodal values required to construct the interpolant are directly available from all computed time steps, while with a higher order interpolant such as $\mathbf{P}_2$, this is no longer true (see Fig. 4.4). Indeed, for a $\mathbf{P}_2$ interpolant the mid edge nodes of the elements cut by the solid are not known directly from the computation at time $n+1$. Therefore, we need to interpolate them using an interpolant built upon $\mathcal{T}^n$. We point out that the "re"-interpolation strategy requires to interpolate on distorted elements. However, for Lagrange-L^2 interpolation the maximal angle condition is not even necessary (see, e.g., [**3**]) for the interpolant to be bounded.

4.4.6. Fluid-structure interaction algorithm

To conclude this section, the fluid solver algorithm reads:

Algorithm 1:
Data: Given $\mathbf{u}_i$, Γ^0, $\mathcal{T}$, loads and BCs
for n **do**
- Build $\mathcal{T}^{n+1}$ from Γ^n and $\mathcal{T}$ (see Sec. 4.4)
- Solve Problem 4 (see Sec. 4.4.4 and 4.4.3)
- Store velocity results on $\mathcal{T}$ solution with reinterpolation of unknown velocity nodal values (see Sec. 4.4.5)
- Update leaflet position, that is $\Gamma^n \leftarrow \Gamma^{n+1}$
- $n \leftarrow n+1$

end

4.5. Algebraic formulation of the coupled problem

Considering the finite element spaces described in Sec. 4.4.2 we can construct (see Eq. (4.13))

$$\mathbf{u}_h = \sum_{j=1}^{n_u} \mathbf{N}_j \hat{\mathbf{u}}_j + \sum_{j=n_u+1}^{n_u+n_\Gamma} \mathbf{N}_j \hat{\mathbf{g}}_j, \tag{4.16}$$

where $\hat{\mathbf{u}}_j$ are the fluid velocity nodal values in the fluid domain, i.e., nodes in $\Omega_h^n \backslash \Gamma^n$, and $\hat{\mathbf{g}}_j$ are the fluid velocity nodal values on the leaflet, i.e., nodes lying Γ^n. Furthermore, in Eq. (4.16) we have $\hat{\mathbf{u}} \in \mathbb{R}^{n_u}$ and $\hat{\mathbf{g}} \in \mathbb{R}^{n_\Gamma}$ (where n_u and n_Γ are the number of velocity degrees of freedom in $\Omega_h^n \backslash \Gamma^n$ and on Γ^n, respectively) and we define $\mathbf{V}_{h,0}^{n+1} = \text{span}(\mathbf{N}^n)$ such that $\mathbf{V}_{h,0}^{n+1} \subset [H_0^1(\Omega)]^2$ and thus $\mathbf{u}_h \in \mathbf{V}_{h,0}^{n+1}$; while

$$p_h = \sum_{j=1}^{m} M_j^n \hat{p}_j \tag{4.17}$$

with $\hat{p} \in \mathbb{R}^m$ (where m is the number of degrees of freedom for the pressure) and $Q_h^{n+1} = \text{span}(\mathbf{M}^n)$ implying that $p_h \in Q_h^{n+1}$. We point out that from here on we do not explicitly state time dependence of $\mathbf{N}^n$ and $\mathbf{M}^n$ for ease of notation since no references are made in what follows to the shape function defined on $\mathcal{T}$.

Now, by employing (4.16) and (4.17) in (4.15) with a suitable construction of $\mathbf{N}$ and using the Bubnov-Galerkin method we can obtain the following algebraic representation of the coupled problem

$$
\begin{bmatrix} \mathbf{A} & \mathbf{A}_l & \mathbf{D}^T & \mathbf{0} \\ \mathbf{0} & \mathbf{C} & \mathbf{0} & \mathbf{l}_\theta \\ \mathbf{D} & \mathbf{D}_l & \mathbf{0} & \mathbf{0} \\ \mathbf{l}_u & \mathbf{l}_l & \mathbf{l}_p & s \end{bmatrix} \begin{Bmatrix} \hat{\mathbf{u}} \\ \hat{\mathbf{g}} \\ \hat{p} \\ \theta \end{Bmatrix} = \begin{Bmatrix} \hat{\mathbf{b}}_u \\ \hat{\mathbf{b}}_g \\ \hat{0} \\ \lambda \end{Bmatrix}. \tag{4.18}
$$

Indeed, in the following we associate the velocity nodal values in the fluid domain by the index set $\mathcal{I}_u = \{1, 2, \ldots, n_u\}$, and the velocity nodal values on the leaflet by the index set $\mathcal{I}_g = \{n_u + 1, n_u + 2, \ldots, n_u + n_\Gamma\}$, and $\mathcal{I}_p = \{1, 2, \ldots, m\}$ the set of pressure degrees of freedom, then the system of equation (4.18) is constructed as follows.

4.5.1. The algebraic fluid part

In (4.18) we have:

$$
\mathbf{A} = \mathbf{M}/\delta t + \mathbf{O} + \mathbf{K}
$$

with

$$
\begin{cases} \mathbf{M}_{|ij} &= \int_{\Omega_h^n} \rho_f \mathbf{N}_j \cdot \mathbf{N}_i \\ \mathbf{K}_{|ij} &= \int_{\Omega_h^n} \mu \nabla^s \mathbf{N}_j : \nabla \mathbf{N}_i \\ \mathbf{O}_{|ij} &= \int_{\Omega_h^n} \rho_f \left(\mathbf{\Pi u}^n \cdot \nabla \mathbf{N}_j \right) \cdot \mathbf{N}_i \end{cases} \qquad \forall (i,j) \in \mathcal{I}_u \times \mathcal{I}_u. \tag{4.19}
$$

We then have

$$
\mathbf{A}_l = \mathbf{M}_l/\delta t + \mathbf{O}_l + \mathbf{K}_l
$$

with the matrices defined as in Eq. (4.19) but for all $(i, j) \in \mathcal{I}_u \times \mathcal{I}_g$. Then the divergence terms are given by

$$
\begin{cases} \mathbf{D}_{|ij} = -\int_{\Omega_h^n} M_i \operatorname{div}(\mathbf{N}_j) \qquad \forall (i,j) \in \mathcal{I}_p \times \mathcal{I}_u \\ \mathbf{D}_{l|ij} = -\int_{\Omega_h^n} M_i \operatorname{div}(\mathbf{N}_j) \qquad \forall (i,j) \in \mathcal{I}_p \times \mathcal{I}_g \end{cases},
$$

and the right hand side is given

$$\hat{\mathbf{b}}_{u|i} = \int_{\Omega_h^n} (\mathbf{f}^{n+1} + \mathbf{\Pi}\mathbf{u}^n/\delta t) \cdot \mathbf{N}_i \qquad \forall i \in \mathcal{I}_u. \tag{4.20}$$

4.5.2. The algebraic coupling part

We first deal with the kinematic constraint (i.e., Eq. (4.15d)) which is represented by the matrix $\mathbf{C}$ and the vectors $\hat{\mathbf{b}}_g$ and $\mathbf{l}_\theta$.

Let $\mathbf{x}_i$ be the set of points of intersection of the fluid mesh $\mathcal{T}$ with Γ^n and the mid points between two intersection points (since we use a Lagrange $\mathcal{P}_2$ basis), and let $\mathbf{R}$ be the axis of rotation, then

$$\hat{r}_i = \sqrt{(\mathbf{x}_i - \mathbf{R})^T(\mathbf{x}_i - \mathbf{R})} \tag{4.21}$$

is the discrete counterpart of the radial coordinate r of the leaflet. Then the discrete counterpart of Eq. (4.15d) is given by

$$\mathbf{C}_{|ij} = \delta_{ij} \qquad \forall (i,j) \in \mathcal{I}_g, \tag{4.22}$$

and $\mathbf{l}_\theta = \{\hat{l}_\theta^x, \hat{l}_\theta^y\}^T$ (where upper-script x and y denote the x and y components) with

$$\begin{cases} \hat{l}^x_{\theta|i} & = -(\hat{r}_i/\delta t) n_x^+ \\ \hat{l}^y_{\theta|i} & = -(\hat{r}_i/\delta t) n_y^+ \end{cases}$$

where $\mathbf{n}^+ = \{n_x^+, n_y^+\}^T$ (see Fig. 4.5). The right hand side is given by $\hat{\mathbf{b}}_g = \{\hat{b}_g^x, \hat{b}_g^y\}^T$ with

$$\begin{cases} \hat{b}^x_{g|i} & = -(\hat{r}_i \theta^n/\delta t) n_x^+ \\ \hat{b}^y_{g|i} & = -(\hat{r}_i \theta^n/\delta t) n_y^+ \end{cases}. \tag{4.23}$$

To construct the discrete counterpart of the torque acting on the solid (see Eq. (4.5) or Eq. (4.15c)) we use a residual approach implemented as follows.

Following **[32]**, we prolong Γ_h^n into $\Gamma_h^{n,e}$ (see Fig. 4.5) such that it divides Ω_h^n into two domains: $\Omega_h^{n,-}$ and $\Omega_h^{n,+}$ with $\Omega_h^n = \Omega_h^{n,-} \cup \Omega_h^{n,+} \cup (\Gamma_h^n \cup \Gamma_h^{n,e})$. Because we use a conforming method we can multiply the first equation of the system of equations (4.12) by test functions $\mathbf{N}_i$ with support on Γ_h^n.

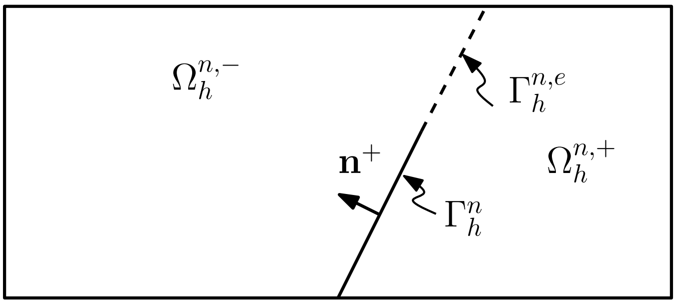

FIGURE 4.5. The leaflet can be virtually extended by $\Gamma_h^{n,e}$ such that $\Omega_h = \Omega_h^{n,+} \cup \Omega_h^{n,-}$.

Then, by integrating by parts on each subdomain $\Omega_h^{n,-}$ and $\Omega_h^{n,+}$ and finally summing both equations we obtain that

$$
(4.24) \quad \begin{cases} \displaystyle\int_{\Omega_h^n} \rho_f \left(\mathbf{u}_h^{n+1}/\delta t + \mathbf{\Pi u}^n \cdot \nabla \mathbf{u}_h^{n+1}\right) \cdot \mathbf{N}_i + \int_{\Omega_h^n} \mu \nabla^s \mathbf{u}_h^{n+1} : \nabla \mathbf{N}_i \\ \quad \displaystyle - \int_{\Omega_h^n} \operatorname{div}(\mathbf{N}_i)\, p_h^{n+1} - \int_{\Omega_h^n} \left(\mathbf{f}^{n+1} + \rho_f \mathbf{\Pi u}^n/\delta t\right) \cdot \mathbf{N}_i \\ \quad \displaystyle = \int_{\Gamma_h^n \cup \Gamma_h^{n,e}} [\![p_h^{n+1}\mathbf{n}^+ - \mu(\nabla^s \mathbf{u}_h^{n+1})\mathbf{n}^+]\!] \cdot \mathbf{N}_i. \end{cases}
$$

Assuming the stress to be continuous over $\Gamma_h^{n,e}$, that is $[\![p_h^{n+1}\mathbf{n}^+ - \mu(\nabla^s \mathbf{u}^{n+1})\mathbf{n}^+]\!]_{\Gamma_h^{n,e}} = \mathbf{0}$ and using the velocity and pressure definition in Eq. (4.16) and (4.17) in Eq. (4.24) with the notation of Eq. (4.18) we deduce that the nodal hydrodynamic force on the leaflet is given by

$$
(4.25) \qquad \hat{\mathbf{f}}_f = \bar{\mathbf{A}}_u \hat{\mathbf{u}} + \bar{\mathbf{A}}_l \hat{\mathbf{g}} + \bar{\mathbf{D}}_l^T \hat{p} - \hat{\mathbf{b}}_l
$$

where the matrices are given as in Eq. (4.19) but for all $(i,j) \in \mathcal{I}_g \times \mathcal{I}_u$, $(i,j) \in \mathcal{I}_g \times \mathcal{I}_g$, $(i,j) \in \mathcal{I}_g \times \mathcal{I}_p$, respectively, and $\hat{\mathbf{b}}_l$ is given as in Eq. (4.20) but for all $i \in \mathcal{I}_g$.

Now, using Eq. (4.7), we obtain the nodal load coupling:

$$
(4.26) \qquad \hat{f}_s = \left(\bar{\mathbf{A}}_u \hat{\mathbf{u}} + \bar{\mathbf{A}}_l \hat{\mathbf{g}} + \bar{\mathbf{D}}_l^T \hat{p} - \hat{\mathbf{b}}_l\right) \cdot \mathbf{n}^+.
$$

Writing the radial coordinate of the leaflet (i.e., r) defined in Section 4.2.2 (see Fig. 4.1) as an isoparametric representation based on the nodal values $\hat{r}_i$ (see Eq. (4.21)) and the finite element basis $\mathbf{N}$ we have

$$
(4.27) \qquad r = \sum_{i \in \mathcal{I}_g} \hat{r}_i N_i.
$$

Then, using Eq. (4.27) in Eq. (4.5) and we obtain

$$\tau = \sum_{i \in \mathcal{I}_g} \hat{r}_i \int_\Gamma f_s N_i, \tag{4.28}$$

with

$$\int_\Gamma f_s N_i = \hat{f}_{s|i}. \tag{4.29}$$

By using (4.26) with (4.29) in (4.28), we conclude that

$$\tau^{n+1} = \hat{r}^T [(\bar{\mathbf{A}}_u \hat{\mathbf{u}} + \bar{\mathbf{A}}_l \hat{\mathbf{g}} + \bar{\mathbf{D}}_l^T \hat{p} - \hat{\mathbf{b}}_l) \cdot \mathbf{n}^+]. \tag{4.30}$$

Now, using (4.30) with (4.15e) and the matrices as defined in (4.18), we deduce that

$$\begin{cases} \mathbf{l}_u & = -\hat{r}^T (\bar{\mathbf{A}}_u \cdot \mathbf{n}^+) \\ \mathbf{l}_g & = -\hat{r}^T (\bar{\mathbf{A}}_l \cdot \mathbf{n}^+) \\ \mathbf{l}_p & = -\hat{r}^T (\bar{\mathbf{D}}_l^T \cdot \mathbf{n}^+) \end{cases} .$$

4.5.3. The algebraic solid part

Using Eq. (4.15e) we have in (4.18)

$$s = I/\delta t^2 + \kappa, \tag{4.31}$$

and, for the right hand side using the notation in (4.30), we have

$$\lambda = -\hat{r}^T (\hat{\mathbf{b}}_l \cdot \mathbf{n}^+) + I/\delta t^2 \left(2\theta^n - \theta^{n-1}\right) + \kappa\theta_0. \tag{4.32}$$

4.6. Numerical experiments

In this section we perform four numerical tests:

- *Test 1: validation.* We consider a test performed in References [**32**]-[**37**] with $\mathbf{P}_2^+/P_1$. We solve this test for stability reasons, as explained in Sec. 4.4.2. We focus on the inf-sup stability issues in Test 2. Unfortunately, due to the fact that we do not have access to the numerical solution proposed in [**32**] or [**37**] we can perform only a qualitative comparison.
- *Test 2: massless leaflet without a rotational spring and effects of the triangles anisotropy on the mixed elements.* The leaflet is massless and there is no rotational spring attached, i.e., $\rho_s = 0$ $\mathsf{g.cm}^{-1}$ and $\kappa = 0$ $\mathsf{dyn.cm.rad}^{-1}$ and we compare the results with the approximated asymptotic solution provided in [**79**]. We perform the test with all four finite element schemes and we discuss the effects of the distortion of the elements on the inf-sup constant, as well as on the conditioning of the linear system. We also show the smallest and largest angles during the simulation for the $\mathbf{P}_2^+/P_1$ element and we compare the results with the condition number of the linear system.
- *Test 3: massive leaflet without a rotational spring.* We take into account the inertial effects by setting various values of the moment of inertia of the leaflet: $I = 0.1, 0.2, 1, 2, 10$ $\mathsf{g.cm}^2$ and without a rotational spring, that is by setting $\kappa = 0$ $\mathsf{dyn.cm.rad}^{-1}$. Because we now focus on the motion of the leaflet that test is only performed with the $\mathbf{P}_2^+/P_1$ element.
- *Test 4: massive leaflet with a rotational spring.* We take into account the inertial effects and the effects of a rotational spring. We set $I = 0.51$ $\mathsf{g.cm}^2$ and three values for κ. For the same reason as with Test 3, we perform the test only with the $\mathbf{P}_2^+/P_1$ element.

It is interesting to observe that in general only few benchmarks exist in the literature for the fluid-structure interaction problems with a rigid leaflet. For instance, we recall [**32**] with the velocity-pressure Navier-Stokes formulation, and [**80**] and [**95**] using the streamfunction vorticity formulation of the Navier-Stokes equations. Therefore, it is difficult to perform a comparison, since different formulations came with different boundary conditions. However, we think that even a qualitative comparison is important to assess reliability of the results in absence of analytical solutions.

4.6.1. Test 1: validation

The present test is mutated from test case 1 of [**32**]. The mesh is defined on the rectangular domain $[-3\ \mathsf{cm}, 3\ \mathsf{cm}] \times [0, 1\ \mathsf{cm}]$. The leaflet has a length of 0.8 cm with an initial angle of $\pi/2$ and $(0,0)^T$ is its point of rotation. The momentum of inertia of the leaflet is $I = 0.51\ \mathsf{g.cm}^2$. The fluid density and viscosity are $\rho_f = 1\ \mathsf{g.cm}^{-2}$ and $\mu = 0.03\ \mathsf{g.s}^{-1}$, respectively. The simulation is performed from 0 s to 4 s with a $\delta t = 4/500\ \mathsf{s}$. The problem is pressure driven, where the boundary condition on $x = 3$ is a "do-nothing" condition (that is $p\mathbf{n} - \mu(\nabla\mathbf{u})\mathbf{n} = \mathbf{0}$), and the pressure (in $\mathsf{g.s}^{-2}$) on $x = -3$ is by the periodic function of period 0.8 defined in Eq. 4.33 (see also Fig. 4.6.1).

$$p_{in}(t) = \begin{cases} 500 & 0 \leq t < 0.3, \\ 5000\,(0.7 - 2t) & 0.3 \leq t < 0.4, \\ -500 & 0.4 \leq t < 0.7, \\ 5000\,(2t - 1.5) & 0.7 \leq t < 0.8. \end{cases} \tag{4.33}$$

On the wall, i.e., at $y = \{0, 1\}$, a no-slip condition is enforced (i.e.,$\mathbf{u} = \mathbf{0}$).

The fluid mesh is a 139×57 union jack discretization of the domain. We point out that the high number of elements is not driven by the fluid-structure problem but rather by stability issues due to Neumann boundary conditions at the inflows. In addition it is well known that using $\nabla^s\mathbf{u}$ with do-nothing boundary conditions induces some undesired spurious effects (see, e.g., [**60**] or [**93**]) so we retain $\nabla\mathbf{u}$ for this test, i.e., the Cauchy tensor for the viscous term.

The results are provided in Fig. 4.7, where a good qualitative behavior is clearly observed.

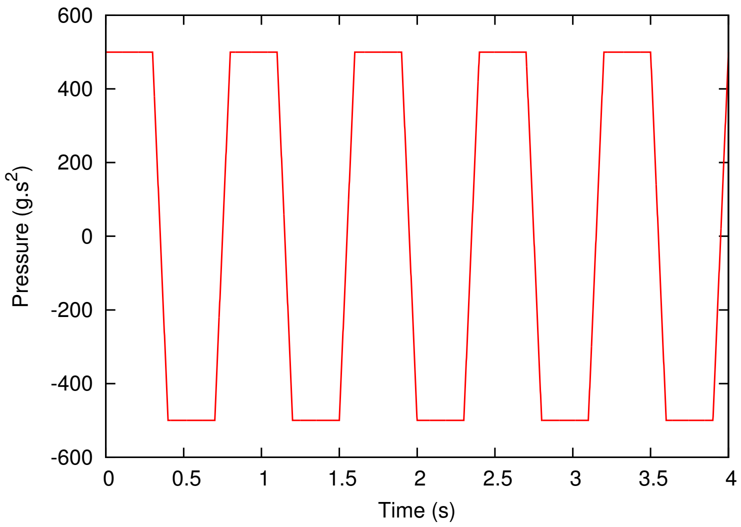

FIGURE 4.6. Test 1: Pressure inflow condition defined in Eq. 4.33

4.6.2. Test 2: massless leaflet without a rotational spring and effects of the triangles anisotropy on the mixed elements

In this problem the leaflet has no mass and no spring is attached, and thus Eq. (4.4) reduces to

$$\tau(t) = 0.$$

That problem has been studied in [**79**] and where an asymptotic analysis of the valve opening without vortex shedding is presented.

The computational domain is the rectangle $[-1\ \mathsf{cm}, 6\ \mathsf{cm}] \times [0, 1\ \mathsf{cm}]$. At the inflow $x = -1$, the velocity is given by Eq. (4.34) (see also Fig. 4.6.2).

$$\mathbf{u}(x, y, t) = \{(1 - \cos(\pi t/T))/2, 0\}^T . \tag{4.34}$$

The length of the leaflet is $L = 0.999\ \mathsf{cm}$. The no-slip boundary condition on $y = 0$ is applied. The do-nothing (or "stress-free") boundary condition is applied on $x = 6$ (that is $p\mathbf{n} - \mu(\nabla^s \mathbf{u})\mathbf{n} = \mathbf{0}$). A symmetry boundary condition is imposed on $y = 1$, i.e., only normal velocity components are set to zero and tangential ones are set to do-nothing (see, e.g., [**36**]). The initial condition is $\mathbf{u}_i = \mathbf{0}$. The time period is set to $T = 10\ \mathsf{s}$. The viscosity is set to $\mu = 0.001\ \mathsf{g.cm}^{-2}$. We use a 127×19 discretization of the fluid domain, the time step is set to $\delta t = 10/128\ \mathsf{s}$ and the simulation is performed from 0 to 10 seconds.

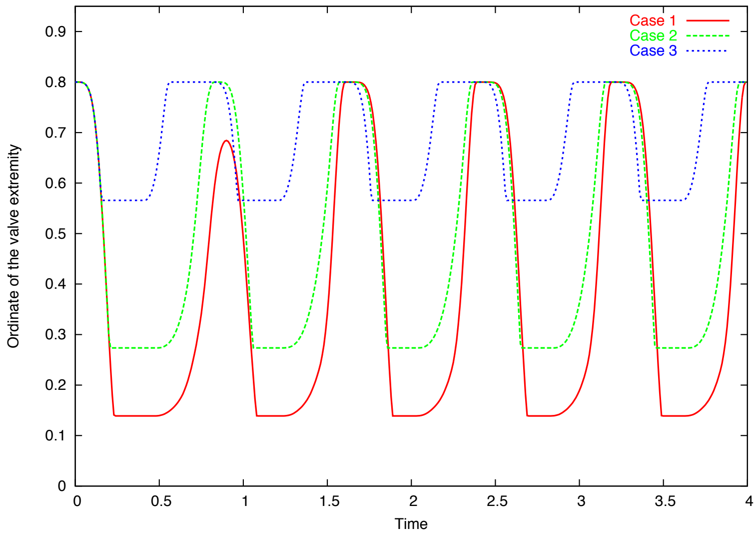

(a) Results extracted from [**37**].

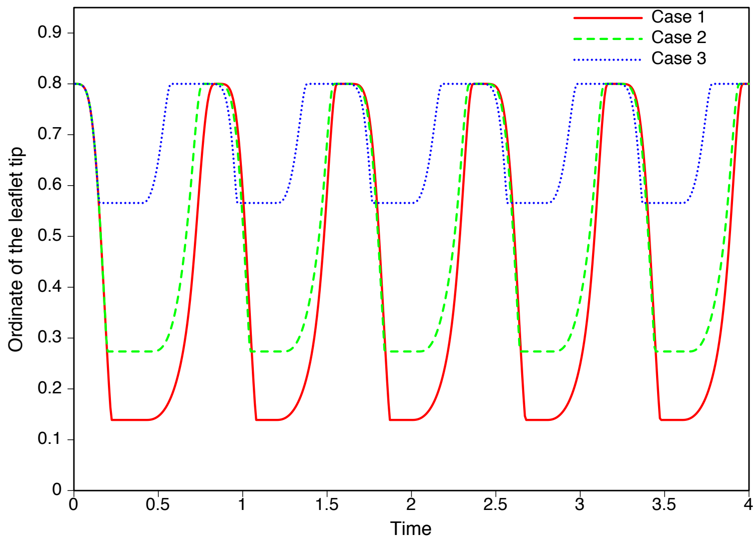

(b) Results from the present method using $\mathbf{P}_2^+/P_1$.

FIGURE 4.7. Test 1: Comparison of the ordinates of the leaflet tip between [**32**] or [**37**] and the present method. Case 1, Case 2, and Case 3, denote the motion of leaflet such that $\theta \in [10°, 90°]$, $\theta \in [20°, 90°]$, and $\theta \in [45°, 90°]$, respectively.

An approximation of the asymptotic solution for the motion of the rigid leaflet problem assuming that no vortex are generated behind the leaflet is

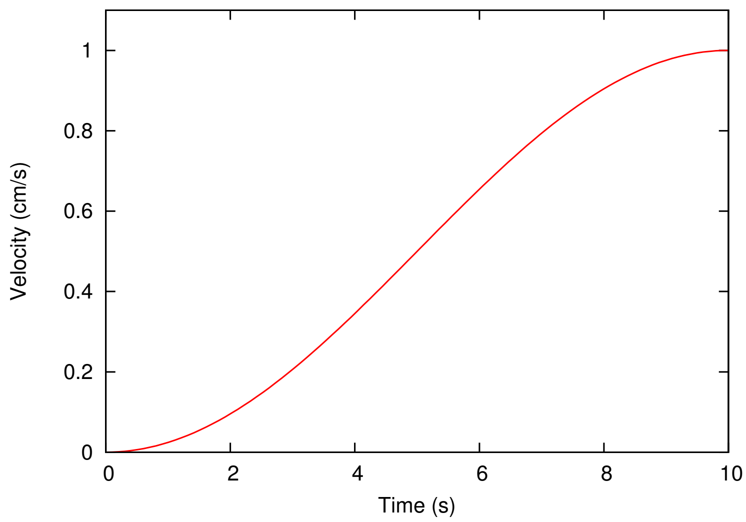

FIGURE 4.8. Test 2: Velocity inflow condition defined in Eq. 4.34

given by (see [**79**]):

$$\frac{d\theta}{dt} = \frac{2u_x(t)\sin(\theta)}{(\sin(\theta) - 2)}, \tag{4.35}$$

with $u_x(t) = (1 - \cos(\pi t/T))/2$. On Fig. 4.9 we can observe that no vortex shedding is present. We deduce that the solution proposed in [**79**] is suitable for our problem. Indeed, as shown on Fig. 4.10 the motion of the leaflet is in accordance with the asymptotic analysis. We recall that Eq. (4.35) is only an approximation of the asymptotic solution. We can see that all four finite element schemes provide a similar displacement of the leaflet. As we pointed out in Sec. 4.4 the mesh is not isotropic, as it can be seen on Fig. 4.11, leading to possible issues with the inf-sup stability and condition number issues. In Fig. 4.12 we report the condition number of the linear system (see Eq. (4.18)) for the four finite element schemes. The condition number of the linear system is affected by the inf-sup constant β. We recall that for the steady incompressible Stokes problem, the conditioning of its Schur complement scales as β^{-2}. Since β is affected by the distortion of the elements, the condition number of the linear system will also be affected. Inf-sup unstable finite elements are expected to show a much worse conditioning than stable elements. This is precisely what we observe. We also recall that

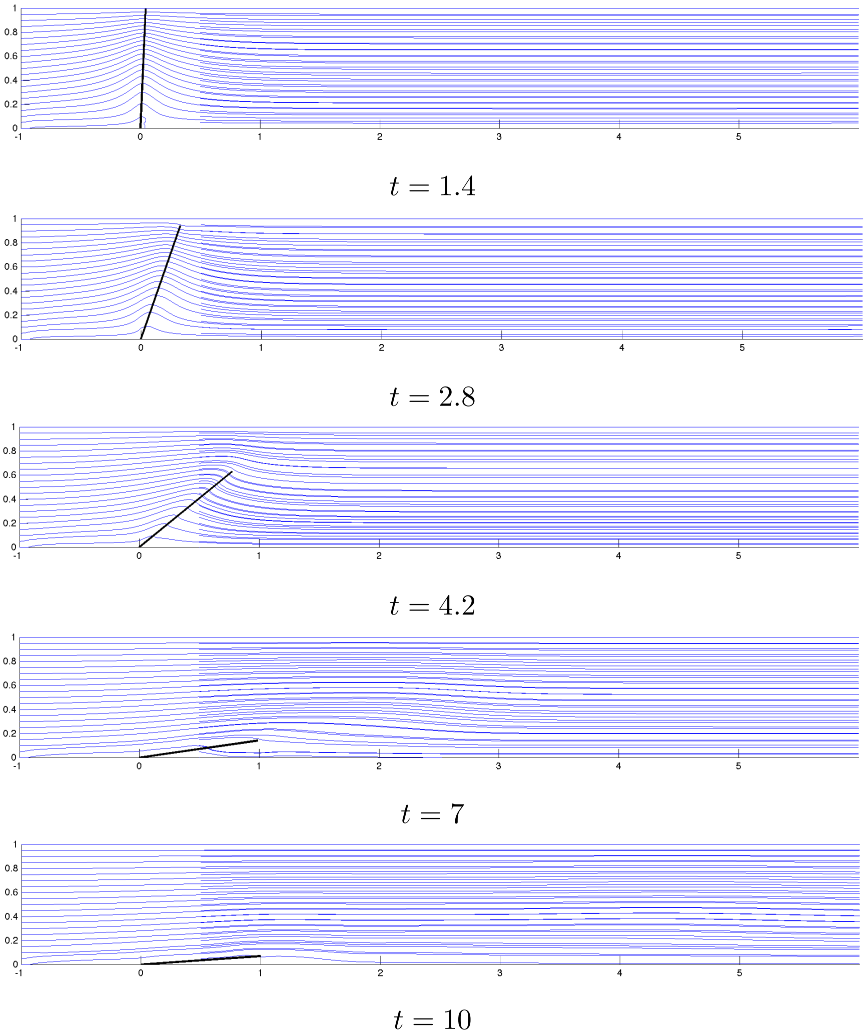

FIGURE 4.9. Test 2: Streamlines snapshots, for a massless leaflet without a spring attached and using $\mathbf{P}_2^+/P_1$. It can be observed that no vortex shedding is present.

the conditioning of the Schur complement is also affected by the conditioning of the pressure mass matrix (see Proposition 4.47 in [**42**]).

(1) For the $\mathbf{P}_2/P_0$ element we see on Fig. 4.12 two peaks indicating ill-conditioning, of one order of magnitude higher than the highest peaks using $\mathbf{P}_2/P_1$ and $\mathbf{P}_2^+/P_1$. Indeed, we can observe on Fig. 4.14, which represents the pressure field at the time of the first peak, spurious modes (a zoom on the culprit is showed on Fig. 4.15).

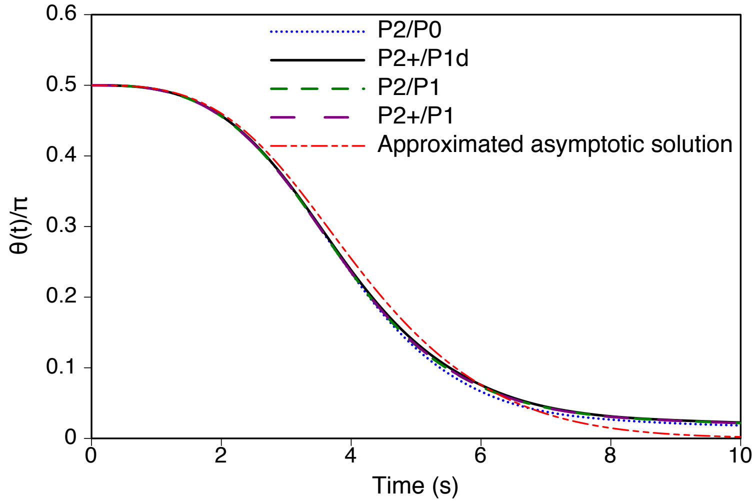

FIGURE 4.10. Test 2: Confrontation of the leaflet motion for the various elements with respect to the solution of Eq. (4.35). P2b/P1d and P2b/P1 denote the $\mathbf{P}_2^+/P_1^d$ and $\mathbf{P}_2^+/P_1$ elements, respectively.

(2) For the $\mathbf{P}_2^+/P_1^d$ element, the associated linear system is very ill-conditioned with respect to the other elements, indicating that the inf-sup constant is much more sensitive to mesh distortion (or the conditioning of the associated pressure mass matrix). On Fig. 4.14 we can observe some spurious modes on the pressure field at the time of one of the peaks present on Fig. 4.12. A zoom on the spurious modes is presented on Fig. 4.15.

(3) For the $\mathbf{P}_2/P_1$ (Hood-Taylor) element, as pointed out in Sec. 4.4.2, the inf-sup constant may be very small on small elements in recessed corners with Dirichlet boundary conditions enforced on both boundary edges but such a situation is very unlikely to occur here, leading to a stable scheme. Indeed no spurious modes are visible on Fig. 4.14.

(4) The $\mathbf{P}_2^+/P_1$ element is stable, as discussed in Chapter 3 and no spurious modes are visible on Fig. 4.14. Globally the conditioning is of the same order as with $\mathbf{P}_2/P_1$.

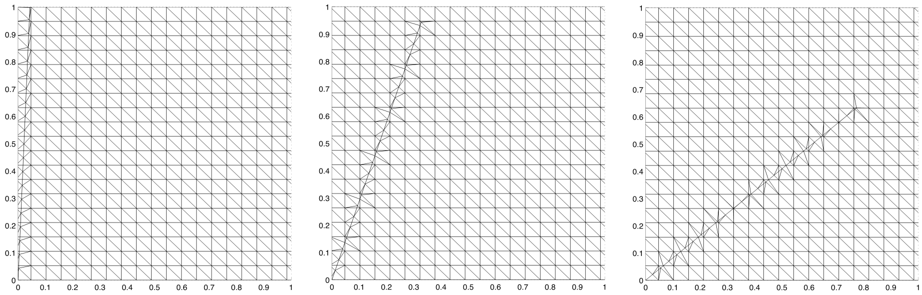

$t = 1.4$ $\quad$ $t = 2.8$ $\quad$ $t = 4.2$

FIGURE 4.11. Test 2: Distortion of the mesh with the $\mathbf{P}_2^+/P_1$ element.

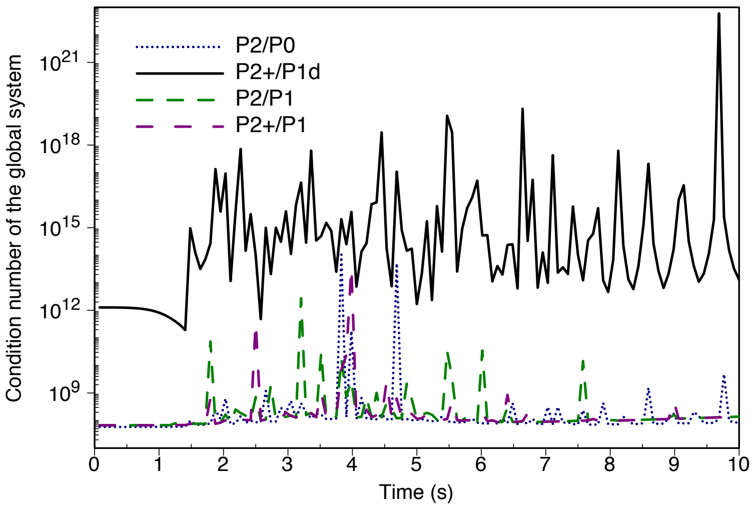

FIGURE 4.12. Test 2: Condition number of the linear system and all elements.

The stable schemes $\mathbf{P}_2/P_1$ and $\mathbf{P}_2^+/P_1$ show a much better conditioning than the inf-sup unstable schemes pointing out the importance of having inf-sup stable elements on distorted meshes.

REMARK 21. *In* [**91**] *the method employed uses the* $\mathbf{P}_2^+/P_1^d$ *element with a similar approach for the local refinement as performed here but maintaining good element ratios by a smoothing procedure. However, our results show that extending the method presented in* [**91**] *to very stretched elements is not straightforward since inf-sup stability issues occur with* $\mathbf{P}_2^+/P_1^d$*. We thus show the necessity of the smoothing procedure with* $\mathbf{P}_2^+/P_1^d$*.*

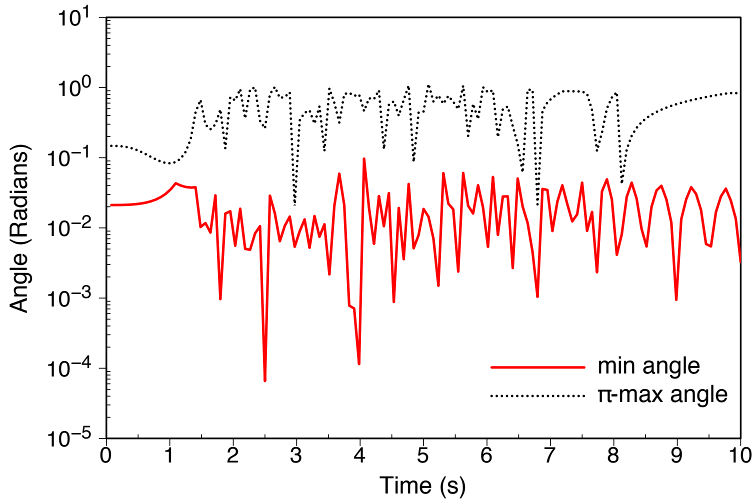

FIGURE 4.13. Test 2: Min and π-max angles when using $\mathbf{P}_2^+/P_1$.

In Remark 15 in Chapter 3, we discuss implications of the minimal and maximal angles conditions with the finite element method. On Fig. 4.13 we report the min and π-max angles during the simulation for Test 1 using the $\mathbf{P}_2^+/P_1$ element. It clearly appears that the largest angle has a much larger bound away from π than the smallest angle away from 0. The difference between the min and π-max angles is roughly of an order of magnitude. The largest difference between the min and π-max angles is of two orders of magnitude. By comparing the conditioning of the linear system associated to $\mathbf{P}_2^+/P_1$ (on Fig. 4.12) and the minimal and maximal angles we observe that only the minimal angle has an impact on the conditioning of the system, as we can observe that the two highest condition numbers correspond to two very small angles, at time $t = 2.5$ s and $t = 3.98$ s.

$\mathbf{P}_2/P_0$ at $t = 3.83$

$\mathbf{P}_2^+/P_1^d$ at $t = 3.13$

$\mathbf{P}_2/P_1$ at $t = 3.2$

$\mathbf{P}_2^+/P_1$ at $t = 3.9$

FIGURE 4.14. Test 2: Pressure field of the elements for Test 2, at times corresponding to ill conditioned linear systems. It shows the inf-sup stability issue for the $\mathbf{P}_2^+/P_0$ and $\mathbf{P}_2/P_1^d$ elements.

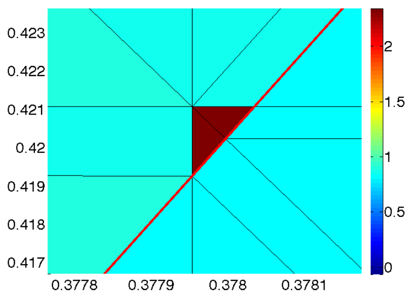

$\mathbf{P}_2/P_0$ at $t = 3.83$

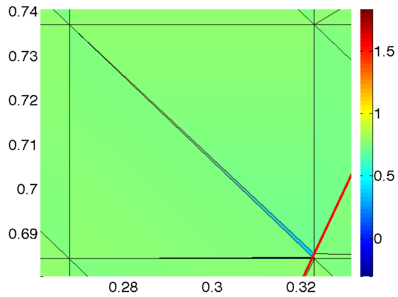

$\mathbf{P}_2^+/P_1^d$ at $t = 3.13$

FIGURE 4.15. Test 2: Zoom on effects of elements distortion: presence of spurious modes. The leaflet is depicted in red.

4.6.3. Test 3: massive leaflet without a rotational spring

In this problem, inspired by **[95]**, we study the sole effect of inertia. The domain under consideration is $[-3\ \mathsf{cm}, 3\ \mathsf{cm}] \times [0, 4\ \mathsf{cm}]$. A no-slip boundary

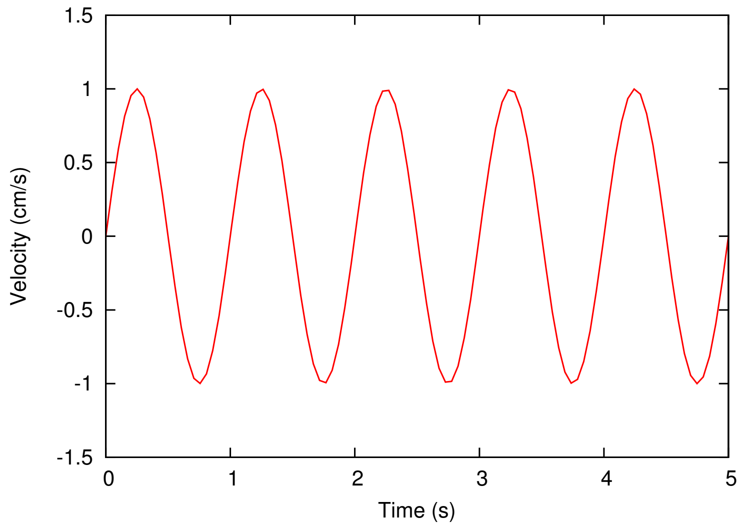

FIGURE 4.16. Test 3: Velocity inflow condition defined in Eq. 4.36

condition on $y = 0$ cm and a symmetric boundary condition on $y = 4$ cm are applied, while the inflow boundary condition is imposed on $x = \pm 3$ cm and it is given by (see also Fig. 4.6.3)

$$\mathbf{u}(x, y, t) = \{\sin(2\pi t), 0\}^T . \tag{4.36}$$

The fluid density is set to $\rho_f = 1.0$ g.cm^{-2} and the viscosity to $\mu = 0.005$ g.s^{-1}. The length of the leaflet is $L = 1$ cm. The initial condition is set by $\mathbf{u}_i = \mathbf{0}$. The mesh size is 113×63 and the time step is set at $\delta t = 0.001$ s with a time range from 0 to 5 seconds. Various values for the mass of the leaflet are considered, as we vary the moment of inertia of the leaflet (see Eq. (4.4)) with $I = 0.1, 0.5, 1, 2, 10$ g.cm^2.

We can observe from Fig. 4.17 that it is more difficult to set in motion the leaflet as it is heavier. We may also see that the average angle of the leaflet over a period is not constant in time, in particular when the leaflet is light.

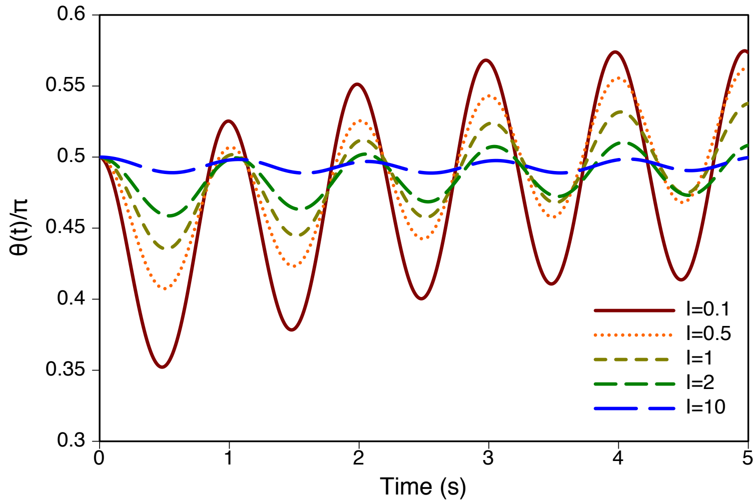

FIGURE 4.17. Test 3: Test for five values of I. No rotational spring is attached to the leaflet.

4.6.4. Test 4: massive leaflet with a rotational spring

In this problem, we propose to test the complete system, with different values for κ, the stiffness of the spring. We choose $\kappa = 0, 1, 5, 10$ dyn.cm.rad^{-1}. The moment of inertia of the leaflet is $I = 0.51$ g.cm^2. For the parameters of the fluid we choose $\mu = 0.03$ g.s^{-1} and $\rho_f = 1.0$ g.cm^{-2}. The fluid domain has the following dimensions: $[-2 \text{ cm}, 6 \text{ cm}] \times [0 \text{ cm}, 1.61 \text{ cm}]$, over which we use a 179×33 discretization. The length of the leaflet is $L = 0.8$ cm. The time step is set at $\delta t = 1/100$ s and time range is from 0 to 1 second. The inflow boundary condition on $x = -2$ is given by the following equation:

$$\mathbf{u}(x, y, t) = \{5(\sin(2\pi t) + 1.1), 0\}^T . \tag{4.37}$$

We impose the no-slip boundary condition on $y = 0$ and $y = 1.61$, and a do-nothing outflow on $y = 6$. The initial condition is $\mathbf{u}_i = \mathbf{0}$. The parameters for this problem are inspired from [**49**] and [**32**].

As a consistency check with expectations form physics, we can observe from Fig. 4.19 that, for a light stiffness, the spring is pushed much further than for the case with a higher stiffness. We may notice that when the flow slows down (after $t = 0.25$), for the case with $\kappa = 5$ and $\kappa = 10$ the spring is pushed back by the energy accumulated in the spring during the spring

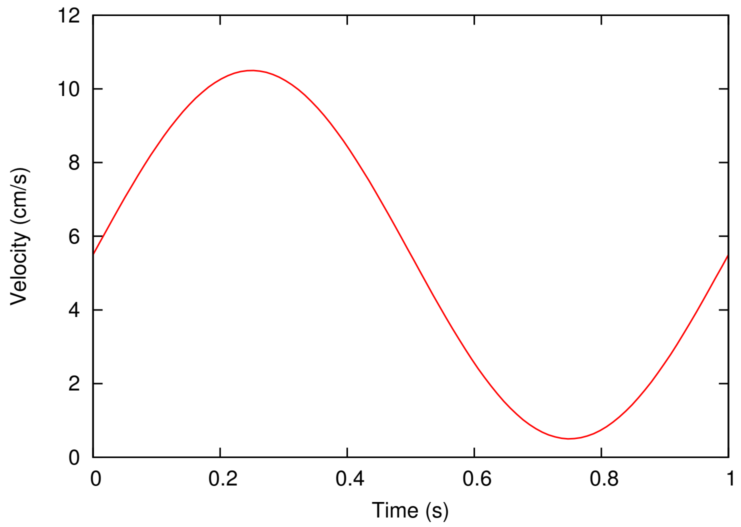

FIGURE 4.18. Test 4: Velocity inflow condition defined in Eq. 4.37

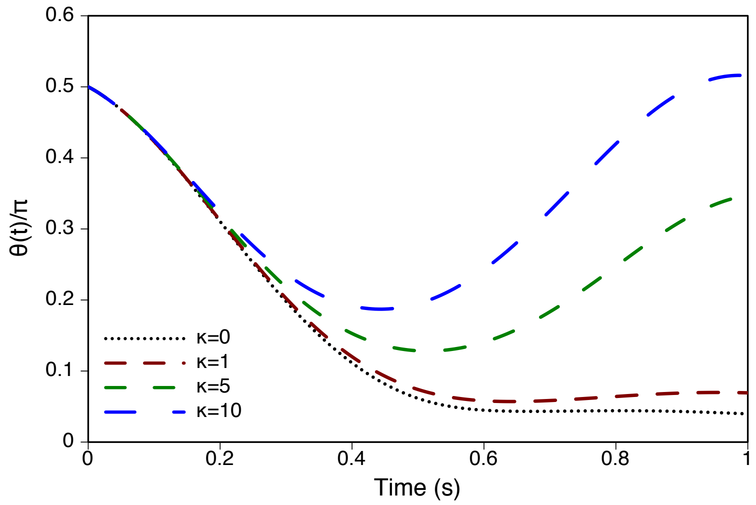

FIGURE 4.19. Test 4: Different values of κ.

compression phase, while for $\kappa = 1$ only a slight return is observed, and none for the case $\kappa = 0$.

We may observe from Figs. 4.20 and 4.21 that at time $t = 0.25$ (i.e, at the inflow velocity peak) a large pressure jump is present across the leaflet, stressing the importance of allowing the pressure to be discontinuous across the leaflet. At times $t = 0.25$ and $t = 0.75$ a clear pressure jump across the leaflet is visible, without any spurious oscillations that may have resulted from continuous pressure and/or continuous velocity derivatives across the

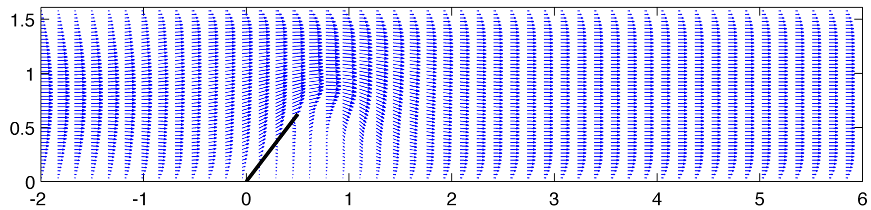

$t = 0.25$

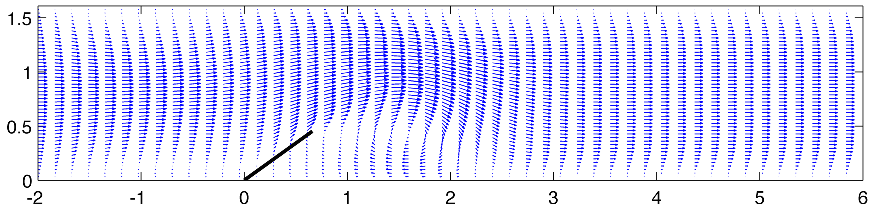

$t = 0.5$

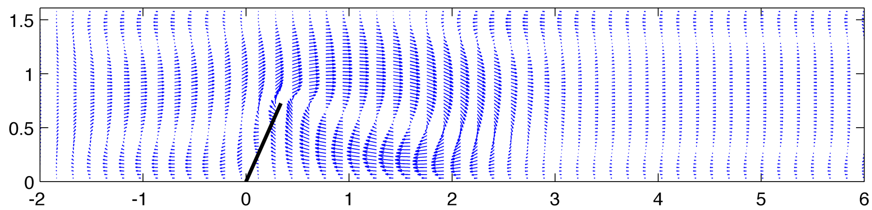

$t = 0.75$

FIGURE 4.20. Test 4: Normalized velocity field of using the $\mathbf{P}_2^+/P_1$ with $\kappa = 10$ at various time snapshots.

structure. At that time the inflow velocity decelerates and the leaflet starts to push back. This effect is particularly visible for $\kappa = 5$ and $\kappa = 10$. At time $t = 0.75$ (i.e., lowest velocity inflow) we can observe that a second vortex has been generated from the push back of the leaflet by the rotational spring.

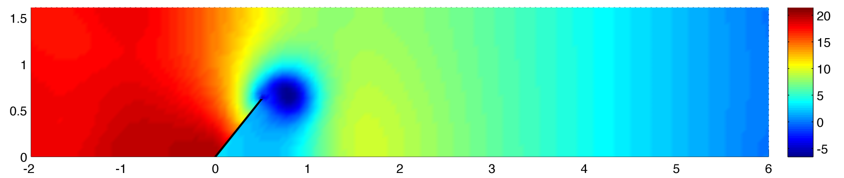

$t = 0.25$

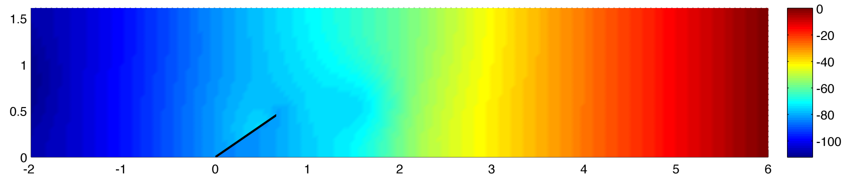

$t = 0.5$

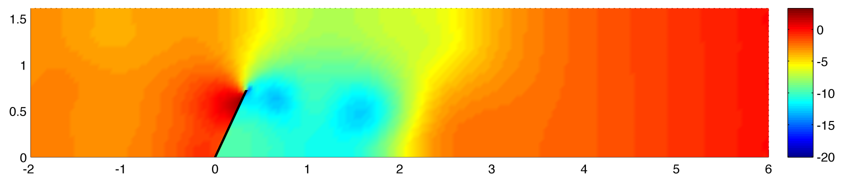

$t = 0.75$

FIGURE 4.21. Test 4: Pressure field of using the $\mathbf{P}_2^+/P_1$ element with $\kappa = 10$ at various time snapshots.

4.7. Conclusive considerations for Chapter 4

In this chapter we have presented an "immersed" type method based on a locally anisotropic remeshing strategy for thin structures, with an application to the case of a hinged rigid leaflet. The results are presented for two-dimensional problems. The method relies on remeshing only elements that are cut by the immersed structure such that the vertices of the triangles of the original mesh remain fixed during the simulation. Furthermore, it is possible to impose the kinematic constraints strongly and to build finite element spaces with a discontinuous pressure and discontinuous velocity derivatives across the leaflet in a fairly easy way.

The main feature of the method is the presence of distorted elements near the structure. It is well known that anisotropic elements are allowed within the finite element method. However, since our method uses incompressible fluids we employ the mixed finite element method, whose finite elements require the fulfillment of an inf-sup condition, which even if satisfied for isotropic meshes may not be for anisotropic ones.

In the present chapter we used different mixed finite element schemes, using both continuous (but discontinuous across the leaflet) and element-wise discontinuous pressures with C^0-elements for the velocity field. More precisely, we tested the $\mathbf{P}_2/P_0$, the $\mathbf{P}_2^+/P_1^d$, the $\mathbf{P}_2/P_1$, and the $\mathbf{P}_2^+/P_1$, mixed finite elements. We first validated the fluid-structure algorithm with results from the literature. We then compared the various mixed finite elements emphasizing on the inf-sup stability and the conditioning of the linear system.

We showed inf-sup issues and strong conditioning issues for the $\mathbf{P}_2/P_0$ element and in particular for the $\mathbf{P}_2^+/P_1^d$ element, but inf-sup stability for the $\mathbf{P}_2/P_1$ and $\mathbf{P}_2^+/P_1$ elements. Because some elements are distorted all finite elements have conditioning issues but stable elements show a much better conditioning than unstable ones, as expected from the theory. However, we observed that the inf-sup condition issue does not have a major impact on the behavior of the leaflet, since spurious modes are localized on very small elements.

The rigidity of the leaflet may have an important role in that result. It was also observed the importance of having a discontinuous pressure field across the leaflet.

CHAPTER 5

Conclusions and future works

Initiated in the 70's, immersed approaches remain an active topic of research, emphasizing the difficulty of the problem. In particular, the trade-off "accuracy versus computational time" is acutely observed within such approaches. We deliberately chose an approach that sharpens accuracy. The focus of the work was on the use of anisotropic elements. Even if the method is not new we found few results on the inf-sup stability of mixed finite elements in such a framework. In this work we provided simple numerical tests to analyze such an issue as well as an application to a fluid-structure interaction problem.

In Chapter 2 we reviewed four "immersed" methods found in the literature. This chapter emphasized on several important notions such as the construction of the finite elements and how to enforce interface constraints in the context of an immersed approach. Two key concepts arose in order to obtain an accurate solution of the problem: the necessity for the finite element space to allow for discontinuities when necessary and the necessity of an accurate quadrature. Chapter 3 provides a method that satisfies both requirements.

In Chapter 3 we proposed a 2D method to accurately solve immersed boundary problems by solely remeshing elements crossed by the immersed boundary. A notable feature of the method is the presence of anisotropic elements. The focus of the chapter was on the inf-sup stability of $\mathbf{P}_2/P_1$ on such elements. It was found that this scheme may be unstable in corners were Dirichlet boundary conditions are imposed on two edges of the element. However, if Dirichlet boundary conditions are imposed on only one edge then the method was showed to be stable, implying that $\mathbf{P}_2/P_1$ might be stable for a large range of applications. Nevertheless, we presented an element that passes all proposed tests, namely $\mathbf{P}_2^+/P_1$, where $+$ designates a cubic bubble with null trace on the edges of the element.

In the last chapter, an application of the results of Chapter 3 was provided to a fluid-structure interaction problem with a thin hinged rigid leaflet. In this chapter, we used several mixed finite elements on distorted meshes, which we tested within the proposed FSI framework. In particular, we found out that the elements using discontinuous pressures (namely, $\mathbf{P}_2/P_0$ and $\mathbf{P}_2^+/P_1^d$) might not be adapted, even if they are a natural choice for such a problem because the pressure is likely to be discontinuous across the thin structure. The inf-sup instabilities have impacts primarily on the pressure field and on the conditioning of the system to solve, especially for $\mathbf{P}_2^+/P_1^d$. Nevertheless, inf-sup unstable elements had a negligible impact on the motion of the rigid leaflet with respect to stable elements. Further studies are required for instance on flexible leaflets to assess this result. On the contrary, the elements with continuous pressures were shown to be up to be inf-sup stable, especially $\mathbf{P}_2^+/P_1$.

Future works may deal with two important issues not discussed in-depth in the present work: the conditioning of the various matrices with anisotropic elements and the extension to 3D of the refinement strategy. For the first problem, specific preconditioning may reduce the effects of anisotropic elements on both mass and stiffness matrices (see, e.g., [**63**]) or using a "multiscale" approach as in [**45**]). For the second problem, a newly numerical method named the Virtual Element Method (VEM) (see, e.g., [**35**] and [**34**]) has two very nice properties that could be employed in the framework discussed in this thesis: it allows elements to be arbitrary polytopes and it is very robust when elements are highly distorted.

APPENDIX A

Additional results to Chapter 2

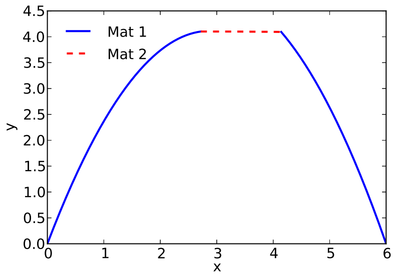

(a) Test with $\alpha_1/\alpha_2 = 1/100$

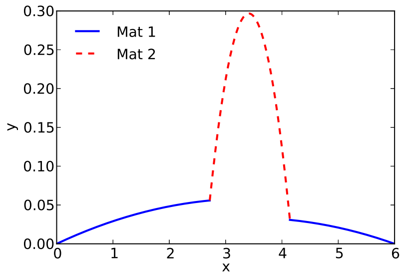

(b) Test with $\alpha_1/\alpha_2 = 100$

FIGURE A.1. Analytical solutions for the numerical test with $f_1 = 1$ on $]A,B[\cup]C,D[$, $f_2 = 1$ on $]B,C[$, for the different material parameters.

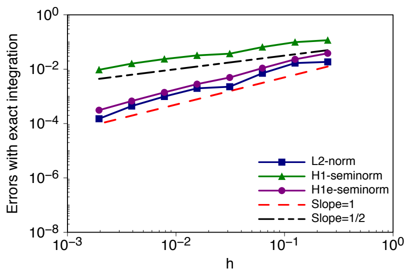

(a) Exact with $\alpha_1/\alpha_2 = 1/100$.

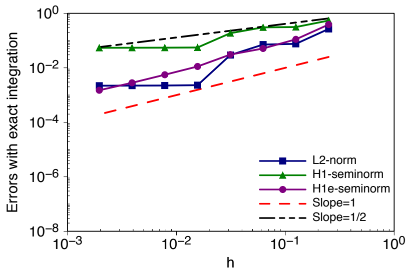

(b) Exact with $\alpha_1/\alpha_2 = 100$.

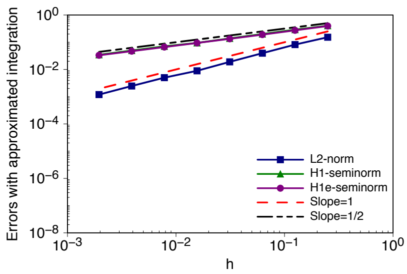

(c) Approximated with $\alpha_1/\alpha_2 = 1/100$.

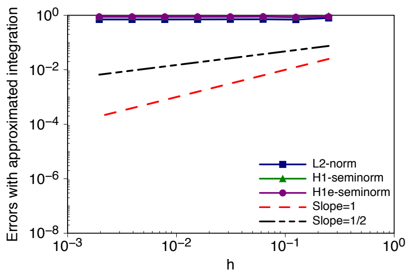

(d) Approximated with $\alpha_1/\alpha_2 = 100$.

FIGURE A.2. The one-field FD method.

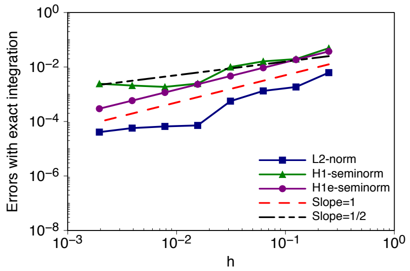

(a) Exact with $\alpha_1/\alpha_2 = 1/100$.

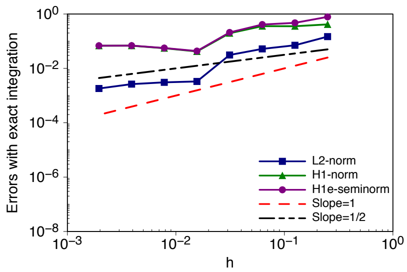

(b) Exact with $\alpha_1/\alpha_2 = 100$.

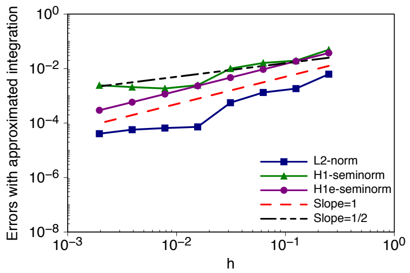

(c) Approximated with $\alpha_1/\alpha_2 = 1/100$.

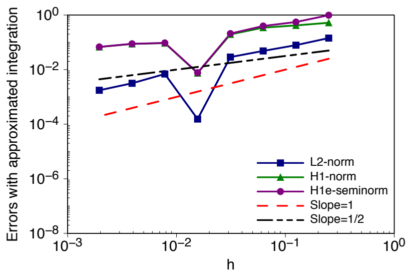

(d) Approximated with $\alpha_1/\alpha_2 = 100$.

FIGURE A.3. The two-field FD/BLM method.

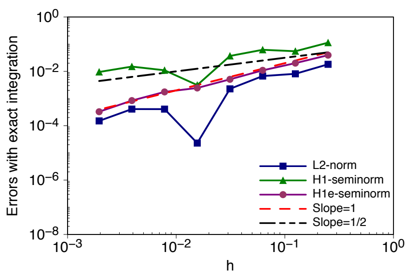

(a) Exact with $\alpha_1/\alpha_2 = 1/100$.

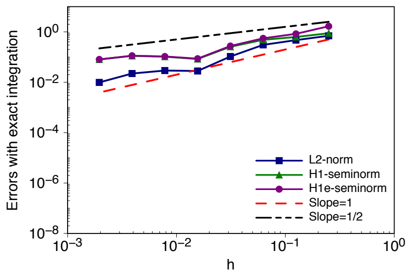

(b) Exact with $\alpha_1/\alpha_2 = 100$.

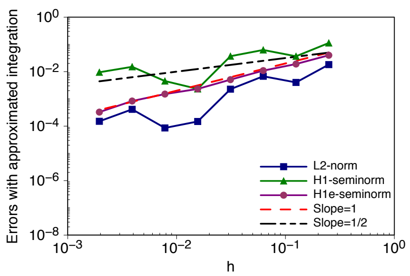

(c) Approximated with $\alpha_1/\alpha_2 = 1/100$.

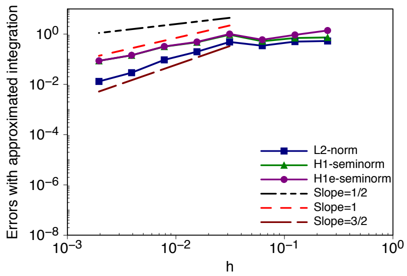

(d) Approximated with $\alpha_1/\alpha_2 = 100$.

FIGURE A.4. The two-field FD/DLM method with $h_r \approx 2$.

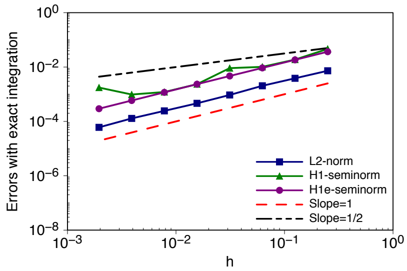

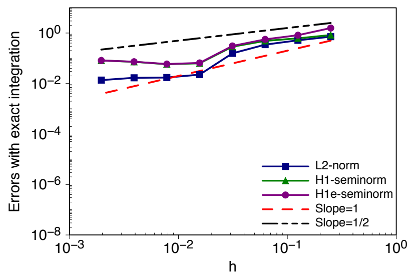

(a) Exact with $\alpha_1/\alpha_2 = 1/100$. (b) Exact with $\alpha_1/\alpha_2 = 100$.

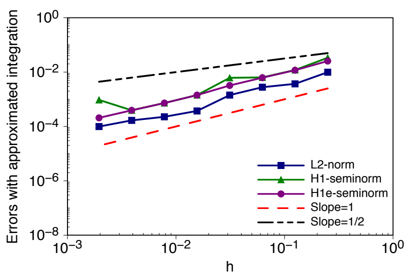

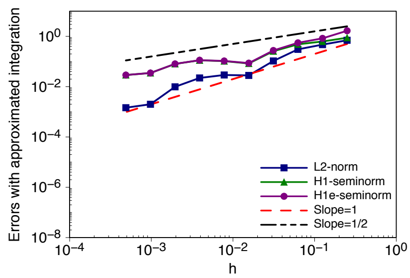

(c) Approximated with $\alpha_1/\alpha_2 = 1/100$. (d) Approximated with $\alpha_1/\alpha_2 = 100$.

FIGURE A.5. The two-field FD/DLM method with $h_r \approx 1/2$.

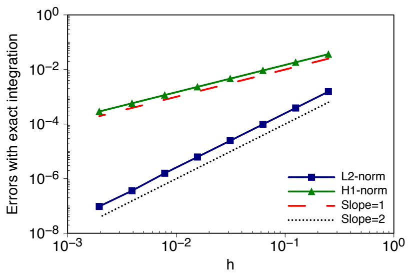

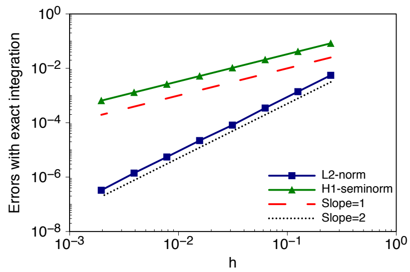

(a) Exact with $\alpha_1/\alpha_2 = 1/100$. (b) Exact with $\alpha_1/\alpha_2 = 100$.

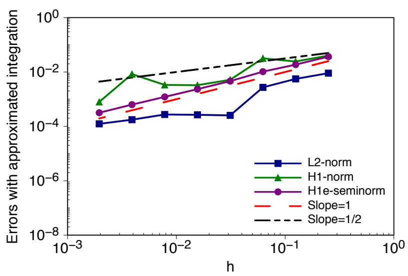

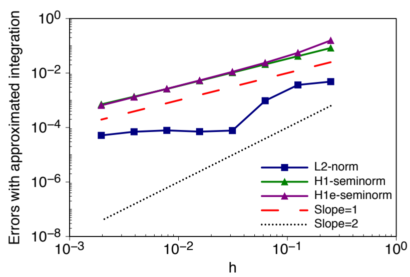

(c) Approximated with $\alpha_1/\alpha_2 = 1/100$. (d) Approximated with $\alpha_1/\alpha_2 = 100$.

FIGURE A.6. The two-field DFD/BLM method.

APPENDIX B

A collocated Lagrange multiplier method for embedded Dirichlet boundary conditions

B.1. Introduction

We consider the problem of imposing an essential conditions on a boundary that is not fitted by a mesh, as in Chapter 3. As explained in that chapter, two questions arise in order to obtain the optimal order of convergence:

(1) How to integrate only in the physical domain?
(2) How to impose correctly the essential boundary condition?

In this appendix we focus on the second question using the Lagrange multiplier method. The first question was already discussed in Chapter 3.

In the finite element method there exists two strategies to impose essential boundary conditions: strongly or weakly. A strong imposition means that the condition is enforced directly into the finite element space. Such an approach is particularly appealing when the mesh does fit the boundary because the elements are interpolatory at the nodes lying on the boundary. Therefore, it is enough to impose the constraint at each node directly in the finite element space. On the contrary, a weak enforcement of the Dirichlet boundary condition does not require any specific shape functions on the boundary. Such an approach is interesting when the boundary does not fit the mesh. In the literature two strategies are generally employed: with a Lagrange multiplier, which introduces a new unknown but is parameter free or with a "stabilization" such as penalty or Nitsche that modifies the original weak formulation but in general it introduces a "user" parameter. We note that a combined strategy is often used. It appears that the construction of such a method is far from trivial since care has to be taken for selecting the Lagrange multiplier finite element space. Otherwise, boundary locking occurs.. This issue is well described in **[84]** with the Mortar method. The

Mortar method in [**84**] consists in computing every intersection points between the mesh and the embedded boundary to use them as grid points for the Lagrange multiplier. However, it is known that with piecewise linear or piecewise constant elements for the Lagrange multiplier the method locks. At least with piecewise linear elements for the primary field. Nevertheless, in this appendix we investigate this issue with a collocated Lagrange multiplier on a piecewise linear reconstruction of the embedded boundary for a Stokes problem using $\mathbf{P}_2/P_0$. We consider two strategies for the Lagrange multiplier. The first strategy consists in imposing the constraint at the intersection points between the embedded boundary and the mesh and the second strategy consists in imposing the constraint at the center of each element-wise linear reconstruction of the embedded boundary.

B.2. The model problem

We recall the problem under consideration. Given $\Omega \subset \hat{\Omega} \subset \mathbb{R}^2$ (see Figure B.1) we solve:

$$\begin{cases} -\Delta \mathbf{u} + \nabla p = \mathbf{0} & \text{in } \Omega, \\ \operatorname{div}(\mathbf{u}) = 0 & \text{in } \Omega, \\ \dfrac{\partial \mathbf{u}}{\partial \mathbf{n}} - p\mathbf{n} = \mathbf{0} & \text{on } \Sigma_N, \\ \mathbf{u} = \mathbf{g} & \text{on } \Sigma_D, \\ \mathbf{u} = \mathbf{0} & \text{on } \Gamma := \partial\Omega / \partial\hat{\Omega}, \end{cases} \tag{B.1}$$

where $\mathbf{g}$ is a suitable given function, while $\overline{\Sigma_D \cup \Sigma_N} = \partial\hat{\Omega}$ and $\Sigma_D \cap \Sigma_N = \emptyset$. We denote Σ_D and Σ_N as external Dirichlet and Neumann boundary conditions, respectively. The outward normal is denoted $\mathbf{n}$.

Remark 22. *For simplicity we impose homogeneous Dirichlet conditions on Γ, vanishing Neumann boundary conditions on Σ_N and a null body-load but an extension is straightforward.*

Its classical weak formulation reads:

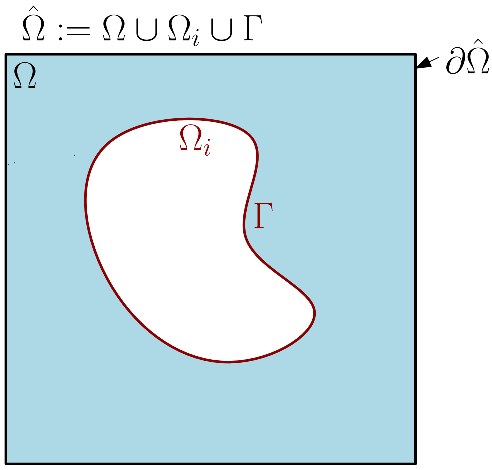

FIGURE B.1. Description of the domains and boundaries.

Find $(\mathbf{u}, p) \in (V \times Q)$ such that for all $(v, q) \in (V_0 \times Q)$

$$
\text{(B.2)} \qquad \begin{cases} \displaystyle\int_\Omega \nabla\mathbf{u} : \nabla\mathbf{v} \mathrm{d}\Omega - \int_\Omega p \operatorname{div}(\mathbf{v}) \mathrm{d}\Omega - \int_\Gamma \left(\frac{\partial\mathbf{u}}{\partial\mathbf{n}} - p\mathbf{n}\right) \cdot \mathbf{v} \mathrm{d}\Gamma = \mathbf{0}, \\ \displaystyle\int_\Omega q \operatorname{div}(\mathbf{u}) \mathrm{d}\Omega = 0, \end{cases}
$$

where

$$
\begin{cases} V := \{\mathbf{v} \in [H^1(\Omega)]^2 | \ \mathbf{v}_{|\Sigma_D} = \mathbf{g} \text{ and } \mathbf{v}_{|\Gamma} = \mathbf{0}\}, \\ V_0 =:= \{\mathbf{v} \in [H^1(\Omega)]^2 | \ \mathbf{v}_{|\Sigma_D} = \mathbf{0} \text{ and } \mathbf{v}_{|\Gamma} = \mathbf{0}\}, \\ Q := L^2(\Omega). \end{cases}
$$

REMARK 23. *In Equation* (B.2) *the term* $\int_\Gamma (\frac{\partial\mathbf{u}}{\partial\mathbf{n}} - p\mathbf{n}) \mathrm{d}\Gamma$ *is equal to zero because* $\mathbf{v}$ *vanishes on* Γ *but we keep this term for a later use.*

In the following we do not impose the condition $\mathbf{u}_{|\Gamma} = \mathbf{0}$ directly in the finite element space but by introducing a Lagrange multiplier $\boldsymbol{\lambda} = (p\mathbf{n} - \partial\mathbf{u}/\partial\mathbf{n})$ such that Problem (B.2) reads:

Find $(\mathbf{u}, p, \boldsymbol{\lambda}) \in W \times Q \times \Lambda$ such that for all $(\mathbf{w}, q, \boldsymbol{\xi}) \in W_0 \times Q \times \Lambda$

$$
\text{(B.3)} \qquad \begin{cases} \displaystyle\int_\Omega \nabla\mathbf{u} : \nabla\mathbf{v} \mathrm{d}\Omega - \int_\Omega p \operatorname{div}(\mathbf{v}) \mathrm{d}\Omega + \int_\Gamma \boldsymbol{\lambda} \cdot \mathbf{v} \mathrm{d}\Gamma = \mathbf{0}, \\ \displaystyle\int_\Omega q \operatorname{div}(\mathbf{u}) \mathrm{d}\Omega = 0, \\ \displaystyle\int_\Gamma \boldsymbol{\xi} \cdot \mathbf{u} \mathrm{d}\Gamma = \mathbf{0}, \end{cases}
$$

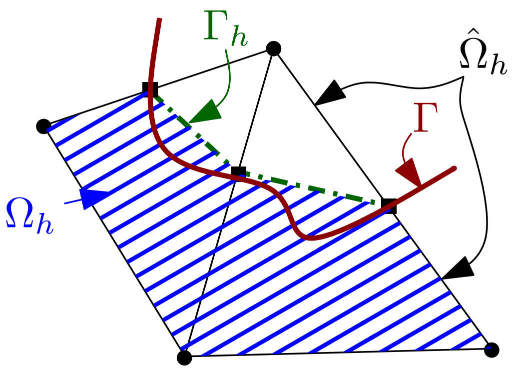

FIGURE B.2. Linear reconstruction of the embedded boundary and the reconstructed domain of integration.

where

$$
\text{(B.4)} \qquad \begin{cases} W := \{\mathbf{w} \in [H^1(\Omega)]^2 |\ \mathbf{w}_{|\Sigma_D} = \mathbf{g}\}, \\ W_0 := \{\mathbf{w} \in [H^1(\Omega)]^2 |\ \mathbf{w}_{|\Sigma_D} = \mathbf{0}\}, \\ \Lambda := [L^2(\Gamma)]^2. \end{cases}
$$

B.3. The unfitted discretize problem

In the classical finite element method we look for a discrete solution on a grid of Ω but in the unfitted formulation the discrete solution is on a mesh of $\hat{\Omega}$, denoted $\hat{\Omega}_h$. In this method we consider a linear reconstruction on each element of the embedded boundary (denoted Γ_h) (see Figure B.2) such that the domain of integration Ω_h satisfy $\Gamma_h = \partial\Omega_h / \partial\hat{\Omega}_h$.

The discrete problem reads: Find $(\mathbf{u}_h, p_h, \boldsymbol{\lambda}_h) \in (\hat{W}^h \times \hat{Q}^h \times \Lambda^h)$ such that, for all $(\mathbf{v}_h, q_h, \boldsymbol{\xi}_h) \in (\hat{W}^h_0, \hat{Q}^h, \Lambda^h)$:

$$
\text{(B.5)} \qquad \begin{cases} \displaystyle\int_{\Omega_h} \nabla\mathbf{u}_h : \nabla\mathbf{v}_h \mathrm{d}\Omega_h - \int_{\Omega_h} p_h \,\mathrm{div}\,(\mathbf{v}_h)\,\mathrm{d}\Omega_h + \int_{\Gamma_h} \boldsymbol{\lambda}_h \cdot \mathbf{v}_h \mathrm{d}\Gamma_h = \mathbf{0}, \\ \displaystyle\int_{\Omega_h} q_h \,\mathrm{div}\,(\mathbf{u}_h)\,\mathrm{d}\Omega_h = 0, \\ \displaystyle\int_{\Gamma_h} \boldsymbol{\xi}_h \cdot \mathbf{u}_h \mathrm{d}\Gamma_h = \mathbf{0}, \end{cases}
$$

where

$$
\begin{cases}
\hat{W}^h \subset \hat{W} := \{\mathbf{w} \in [H^1(\hat{\Omega})]^2, \mathbf{w}_{|\Sigma_D} = \mathbf{g}\} \\
\hat{W}_0^h \subset \hat{W}_0 := \{\mathbf{w} \in [H^1(\hat{\Omega})]^2, \mathbf{w}_{|\Sigma_D} = \mathbf{0}\} \\
\hat{Q}^h \subset \hat{Q} := L^2(\hat{\Omega}) \\
\Lambda_h \subset [L^2(\Gamma_h)]^2.
\end{cases}
$$

REMARK 24. *Notice that we do perform the integration of Problem* (B.5) *on* Ω_h. *Furthermore, we have* $W \subset \hat{W}$ *and* $Q \subset \hat{Q}$. *We also slightly change the problem as we consider* $\Lambda_h \subset [L^2(\Gamma_h)]^2$ *and not* $\Lambda_h \subset \Lambda$ *since we linearize* Γ *into* Γ_h. *However, we have* $\lim_{h\to 0} \Gamma_h = \Gamma$.

In the following we give a precise definition of Λ_h. The space we consider is (see, e.g., [**20**] or [**52**])

$$
\Lambda_h := \left\{ \boldsymbol{\lambda}_h(\mathbf{x}) = \sum_{k=1}^{N_\lambda} \boldsymbol{\lambda}^k \delta(\mathbf{x} - \mathbf{x}_k) \right\}, \tag{B.6}
$$

where $\delta(\cdot)$ is the Dirac delta function and N_λ is the number of Lagrange multiplier nodes. Such a choice corresponds to a collocation type method. Indeed, we impose the boundary condition on an arbitrary set of $\mathbf{x}_k$. In the numerical tests we present two choices for the set of $\mathbf{x}_k$.

B.4. Numerical tests

We propose to solve the Stokes problem in $\hat{\Omega} := [0,1]^2$ with boundary conditions: $\mathbf{u}_{|\Sigma_1} = (1-y^2)$, $\mathbf{u}_{|\Sigma_2} = \mathbf{0}$ and free stress on Σ_3 (see Figure 3(a)). The radius of the circle described by Γ is 0.4.

We propose two different strategies for the Lagrange multiplier. The first strategy denoted "Edge" is the set of all the intersection points of the embedded boundary with the edges of the elements. The second strategy denoted "Mid" is the set of all mid-points of the piecewise linear reconstruction with the intersection points of the embedded boundary and the edges of the elements. The two strategies are depicted in Figure 3(b). The code uses piecewise quadratic and piecewise discontinuous elements for the velocity and the pressure, respectively. The solution is compared to a simulation

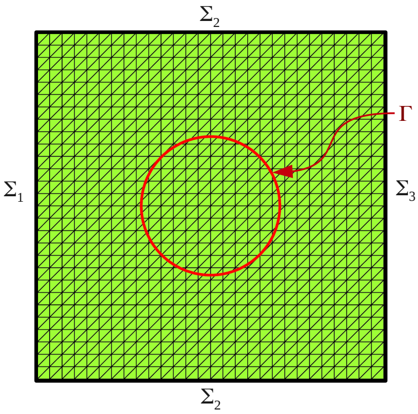

(a) Mesh description: 1568 elements, embedded boundary radius of 0.4 with 607 elements; performed with FreeFem++ (see [**82**]). The number of elements on Γ_h is kept constant for all simulations and is of the same order than the fitted discretization of Γ (i.e., 600 elements).

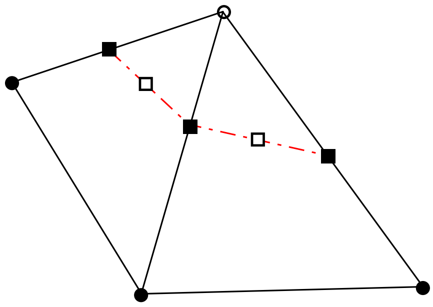

(b) Strategies of a collocated Lagrange Multiplier over a linearized embedded boundary: 1) at the edge (denoted "Edge" - black squares) and 2) at the middle (denoted "Mid" - white squares). We note that the black disks are physical nodes and the white circle is a free node.

FIGURE B.3. Description of the discretization of the problem and the Lagrange multiplier strategies.

with a discretization of 500×500 for $\hat{\Omega}$ and discretization of 600 elements for Γ. The meshes are performed with FreeFem++ (see [**82**]). The error is computed by interpolating the solution of the unfitted mesh on the fitted mesh and then compared to the fitted solution. We use a trapezoidal rule on each element to perform the integration. In order to test the method we first consider a problem with a free stress condition on Γ such that no Lagrange multipliers are used. The results show (see Figure B.4) that the method has a quadratic and a linear rate of convergence for the velocity and the pressure, respectively. The method is optimal with embedded natural conditions for a $\mathbf{P}_2/P_0$ scheme.

On the contrary, for essential boundary conditions, the method is sub-optimal in velocity and even only first order with the Edge strategy. Nevertheless, the Mid strategy performs better in all cases. We note that the rate of convergence of the pressure is almost optimal but we can see from Fig. B.5

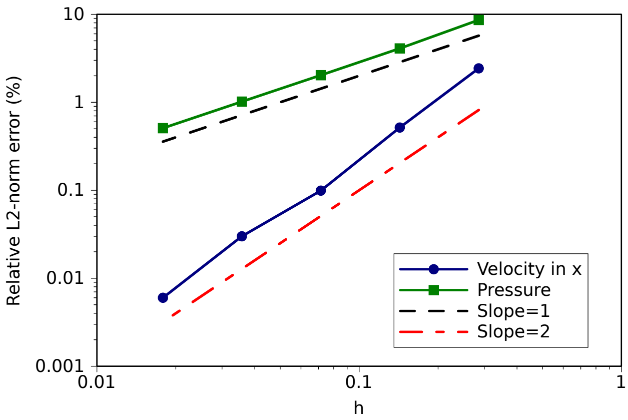

FIGURE B.4. Optimal rate of convergence for a $\mathbf{P}_2/P_0$ scheme with a free stress condition on Γ.

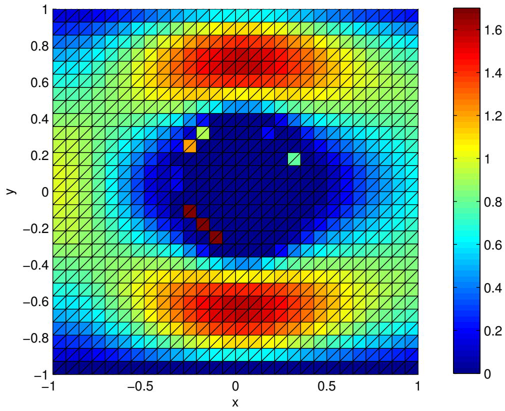

FIGURE B.5. Spurious oscillations of velocity field in x with the Mid Lagrange multiplier strategy for a 1568 elements uniform mesh.

that oscillations occur in elements crossed by Γ. Such an issue can be understood from Fig. 3(b). Indeed, the Edge and the Mid strategies have 3 and 2 constraints, respectively, for one free degree of freedom (the white circle). As a consequence, assuming the primary field is a piecewise linear element, it is expected that both methods lock. However, the Mid strategy behave better than the Edge strategy (see Fig. 6(a)). Notice that the pressure field converges with the optimal rate of convergence (see Fig. 6(b)).

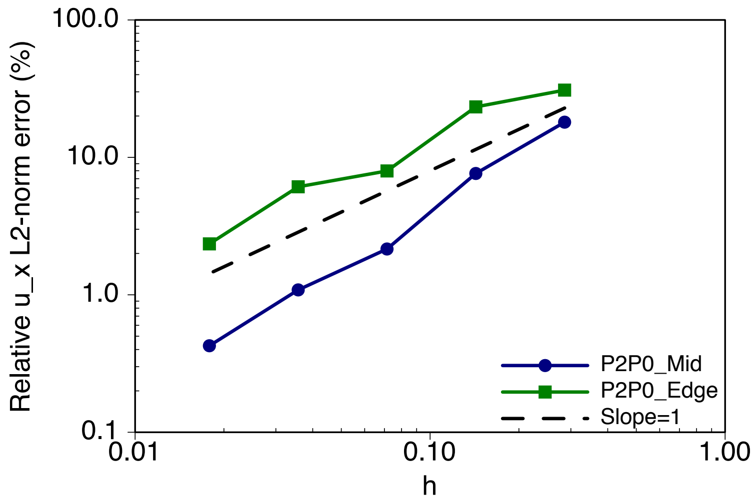

(a) Sub optimal rate of convergence in velocity for a $\mathbf{P}_2/P_0$ scheme: coefficient after a regression analysis: 0.94 for Edge LM and 1.34 for Mid LM, respectively.

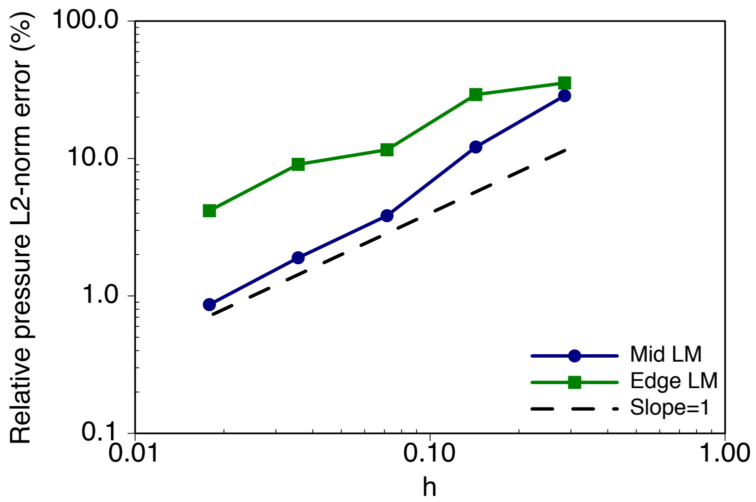

(b) Almost optimal convergence in pressure.

FIGURE B.6. Rate of convergence of a $\mathbf{P}_2/P_0$ scheme in L2-norm of the velocity and pressure for the Stokes problem with homogeneous Dirichlet conditions on Γ.

B.5. Conclusive considerations for Appendix B

We introduced an unfitted finite element method with a collocated Lagrange multiplier with an application to the Stokes problem. We performed a linear reconstruction of the embedded boundary with respect to the mesh. As a consequence, the method requires to integrate over domains crossing the support of the shape functions. In this appendix we chose to integrate over sub-elements.

In the numerical analysis we proposed two strategies for the collocated Lagrange multiplier. The first strategy consisted in imposing the constraints on the intersection of the embedded boundary with the mesh element edges and the second strategy on the mid distance between these intersection points. The results with a $\mathbf{P}_2/P_0$ code show that both methods lead to boundary locking and thus in a sub-optimal rate of convergence for the velocity. Nevertheless, the pressure converge almost optimally. We also showed that the second strategy, even if not optimal is a much better choice than the first.

APPENDIX C

A numerical evaluation of the inf-sup stability of mixed finite elements on anisotropic triangles for the incompressible Stokes problem

In this appendix we give extended results to Chapter 3 for mixed finite elements on anisotropic triangles. We analyze the eigenvalues and eigenvectors of the elements $\mathbf{P}_2/P_0$, $\mathbf{P}_2/P_1$, $\mathbf{P}_2^+/P_1$ and $\mathbf{P}_2^+/P_1^d$ on the simple test developed in Chapter 3. We then determine the number of spurious modes for each elements and their locations.

C.1. Introduction

Many proofs of convergence for the finite element method rely on a *shape-regularity* constraint of the mesh, i.e., that for a triangle the smallest angle is bounded below (a similar assumption can be generalized to quadrilaterals using the element mesh ratio). This condition is sufficient for the finite element method to converge (see, e.g., [**98**]). However, it is also known from, e.g., [**11**] and [**62**] that the shape regularity assumption is not necessary. Indeed, a less stringent constraint, often called *shape semi-regularity*, requires for a triangle that its maximal angle be strictly bounded away from π. This condition is sufficient for the finite element method to converge.

There is a large range of applications for which shape semi-regular meshes are useful, in particular for fluid problems: from boundary layer meshes to immersed boundary methods, just to name a few applications. A classical model for incompressible fluid dynamics is the Stokes problem, which is the focus of the present appendix, and many researches for the Stokes problem appear to be oriented toward the use of boundary layer meshes and in the literature two types of shape semi-regular meshes are often considered: edge (or layer) meshes (see Figure 1(a)), and corner meshes (see Figure 1(b)).

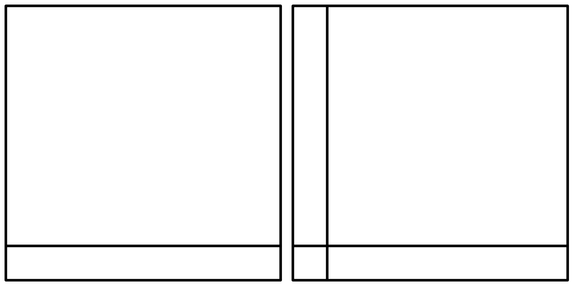

(a) An edge (or layer) mesh. (b) A corner mesh.

FIGURE C.1. Two types of shape semi-regular meshes.

We first quickly recall the reasons for the present study. The mixed finite element method is widely used to treat incompressible flow problems. The shape regularity assumption is in general assumed and its necessity appears to be an open problem for many mixed finite elements. The present appendix discusses that issue.

One of the main requirement for convergence of the mixed finite element method is inf-sup stability. More precisely, for the incompressible Stokes problem, there exists a strictly positive constant (independent of the mesh size) that bounds the divergence operator. The question for anisotropic meshes is to know if the inf-sup constant is also independent of the shape of the elements.

In this appendix we only focus on conforming finite element pairs for the steady incompressible Stokes problem.

It is shown in [**17**] that a stabilized $\mathbf{Q}_1/Q_1$ (with a continuous pressure) and a stabilized $\mathbf{Q}_1/P_0$ are stable on layer meshes with a bounded *grading factor*, i.e., there cannot be a large difference of size between adjacent elements. In this paper, the authors claim that the result can be extended to general affine 2D and 3D elements. For all the cited works that follows, no grading factor are required. In [**85**] it is proved that the $\mathbf{Q}_k/P_{k-2}^d$ ($k \geq 2$, for discontinuous pressures) is stable on layer meshes but no proof is given for corner meshes. Indeed, it is shown in [**86**] that the $\mathbf{Q}_2/P_0$ element fails on corner meshes. It is shown in [**1**] that the $\mathbf{Q}_k/P_{k-1}^d$ element fails on edge meshes, and that the dependence of the inf-sup constant is on the inverse of the mesh ratio. They also show that the $\mathbf{Q}_{k+1}/P^d_{k-1}$ element is stable on edge meshes, but with some dependence on k. For corner meshes, they confirm the numerical result in [**86**], that is $\mathbf{Q}_{k+1}/P^d_{k-1}$ is unstable for such meshes. They give a lower bound for the inf-sup constant showing a dependence on the inverse of the square root of the mesh ratio. More importantly, it is proved that adding an extra polynomial on the velocity space stabilizes the element on corner meshes, but the order of the polynomial depends on the mesh ratio. In [**71**] a proof of stability of the $\mathbf{Q}_1/P_0$ element stabilized with a pressure jump strategy is given. It is proved that the inf-sup constant is independent of the element mesh ratio on both edge and corner meshes. We point out that for all previously cited papers, proofs are given only for quadrilaterals and the tensorial structure of quadrilateral meshes is in general usually used, precluding a straightforward extension to affine mappings and thus triangles. Most of the results only apply for affine mappings on quadrilaterals. Other results for stabilized quadrilaterals are given in, e.g., [**26**], [**73**], or [**25**].

Regarding triangles, in [**5**] it is showed numerically that the $\mathbf{P}_2/P_1$ is stable on triangular edge meshes but that it fails on triangular corner meshes. More importantly, it is shown that $\mathbf{P}_2^+/P_1$ (i.e., $\mathbf{P}_2/P_1$ with an added cubic bubble) passed all proposed tests. No proof of stability of the $\mathbf{P}_2^+/P_1$ is given and up to now, to the best authors' knowledge, no proof is known. In the work of [**4**] a proof of the stability of the $\mathbf{P}_2/P_0$ element for both edge and corner meshes is given but with some restriction on corner meshes. In [**76**] a residual-free-bubble stabilized formulation for the $\mathbf{P}_1/P_1$ is proposed on general triangular meshes. The element is proven stable but under some restrictions on the orientation of the mesh with respect to the solution of the problem. We point out that in the work [**71**] the authors claim that their results can be extended to triangles but no formal proof is given.

In this appendix we present new numerical results following the work performed in Chapter 3. Indeed, only few results for triangles have been found in the literature. In particular, we show a test case for which the $\mathbf{P}_2/P_0$ element fails and not only in corners with Dirichlet boundary conditions.

This result shows that shape semi-regularity of the mesh is not a sufficient condition for this element. We also recover the results of [**5**] and Chapter 3 for $\mathbf{P}_2/P_1$ and $\mathbf{P}_2^+/P_1$. With respect to Chapter 3, in this appendix, we provide additional results for $\mathbf{P}_2/P_1$ on the order of degeneracy of the spurious modes and their locations. Another new result concerns the $\mathbf{P}_2^+/P_1^d$ element (i.e., Crouzeix-Raviart) which fails for both "edge" and "corner" meshes. Moreover, on the contrary to the other elements, the $\mathbf{P}_2^+/P_1^d$ element shows two kinds of pressure spurious modes: the first one with a dependence on $\sigma^{1/2}$, where σ is the aspect ratio, as the other unstable elements, and the second one with a dependence on σ. This result is similar to those found in [**1**] for the $\mathbf{Q}_2/P_1^d$ element.

C.2. Problem

We recall that (see Chapter 3) the algebraic Stokes problem using the Finite Element Method reads: Find $(\hat{\mathbf{v}}, \hat{\mathbf{q}}) \in \mathbb{R}^n \times \mathbb{R}^m$ such that

$$\begin{bmatrix} \mathbf{A} & \mathbf{B}^T \\ \mathbf{B} & \mathbf{0} \end{bmatrix} \begin{Bmatrix} \hat{\mathbf{u}} \\ \hat{\mathbf{p}} \end{Bmatrix} = \begin{Bmatrix} \hat{\mathbf{f}} \\ \hat{\mathbf{g}} \end{Bmatrix} \tag{C.1}$$

In Problem (C.1), $\mathbf{A}$ is the Laplacian operator matrix (or stiffness matrix), $\mathbf{B}$ is the divergence operator matrix.

It is well known that in order to have a unique and stable solution to Problem (C.1), the following condition is required (known as the inf-sup condition see, e.g., [**22**]): $\exists \beta_h > 0$ (independent of h) such that

$$\max_{\hat{\mathbf{v}} \in \mathbb{R}^n \setminus \{\mathbf{0}\}} \frac{\hat{\mathbf{v}}^T \mathbf{B}^T \hat{\mathbf{q}}}{||\hat{\mathbf{v}}||_A} \geq \beta_h ||\hat{\mathbf{q}}||_M \qquad \forall \hat{\mathbf{q}} \in \mathbb{R}^m. \tag{C.2}$$

Where $||\hat{\mathbf{v}}||_A^2 = \hat{\mathbf{v}}^T \mathbf{A}^T \hat{\mathbf{v}}$ is the norm associated to the matrix $\mathbf{A}$, and $||\hat{\mathbf{q}}||_M^2 = \hat{\mathbf{q}}^T \mathbf{M}^T \hat{\mathbf{q}}$ is the norm associated with the matrix $\mathbf{M}$, the pressure mass matrix.

As discussed above, a crucial issue is precisely the dependence of β_h on the shape of the elements in the mesh $\mathcal{T}$.

C.3. Eigenvalue tests of the associated numerical inf-sup constant to the incompressible Stokes problem

We propose the constant flow problem (see Equation C.3) with different boundary conditions (see Fig. C.2).

$$
\text{(C.3)} \qquad \begin{cases} u_x(x,y) = 1, \\ u_y(x,y) = 0, \\ p(x,y) = 0. \end{cases}
$$

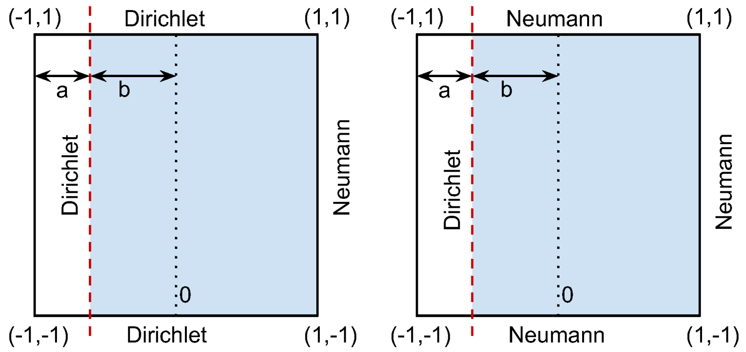

(a) Problem 1: with Dirichlet boundary conditions on $y = \pm 1$.

(b) Problem 2: with Neumann boundary conditions on $y = \pm 1$.

FIGURE C.2. Boundary value problems under consideration for the inf-sup eigenproblem.

More importantly, we consider three meshes for the inf-sup test problems:

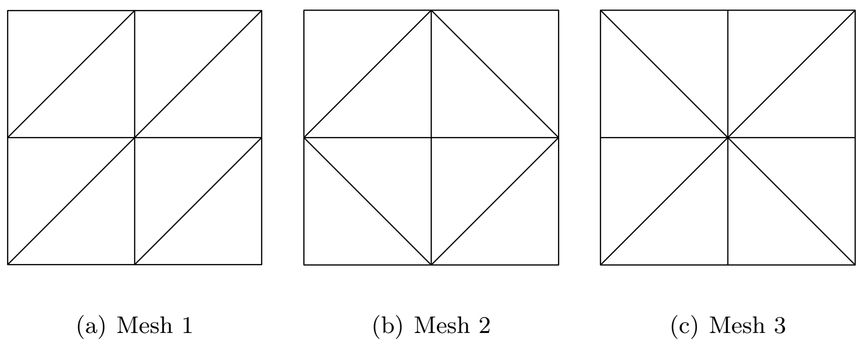

(a) Mesh 1

(b) Mesh 2

(c) Mesh 3

FIGURE C.3. The three meshes used for the generalized eigenproblem with different immersed boundary positions. The background domain is defined on $[-1, 1]^2$.

We are interested in these numerical tests to evaluate the eigenvalues and eigenvectors of the associated numerical inf-sup generalized eigenproblem:

$$\mathbf{B}\mathbf{A}^{-1}\mathbf{B}^T\mathbf{q} = \lambda\mathbf{M}\mathbf{q}. \tag{C.4}$$

We perform the tests with four mixed finite elements: $\mathbf{P}_2/P_0$, $\mathbf{P}_2/P_1$ (with continuous pressure), $\mathbf{P}_2^+/P_1$ (with continuous pressure) where + denotes a cubic bubble, and $\mathbf{P}_2^+/P_1^d$ (with discontinuous pressure). It is known that all four finite element schemes are inf-sup stable with isotropic meshes (see, e.g., **[22]** for detailed presentations and stability proofs).

We point out that all eigenvectors are orthogonalized using the Gram-Schmidt process.

C.4. Summary of Results

We first present a summary of the results and then in Section C.5 we give a series of plots of the first 8 square rooted eigenvalues of the generalized inf-sup eigenproblem (C.4). These plots allow deducing for the unstable cases, the order of degeneracy of the numerical inf-sup constant as function of a or b, as well as the number of degenerative modes. We then present a representation of some of the spurious modes. All eigenvectors given in the following sections represent degenerative cases with a or b equal to 10^{-5}. Spurious mode representations are not depicted on the real mesh since the distorted elements are very small but on more representative meshes. The element $\mathbf{P}_2^+/P_1^d$ has many spurious modes and it is not possible to represent them all. We proceed to a selection of the spurious modes to represent. We invite the readers to check tables reporting the first eigenvalues and eigenvectors in the Tables in Section C.6. We point out that regarding the tables for the $\mathbf{P}_2^+/P_1^d$ element, pressure on a given element reads $P(x, y) = \text{cst} + (\text{dx})x + (\text{dy})y$, where cst, dx and dy are real numbers.

The summary of results is associated to a table (see Tab. C.1) that reports for each mesh and each tests (i.e., $a \to 0$ and $b \to 0$) if it passes the test (i.e., if the numerical inf-sup constant remains bounded) or the number of spurious modes.

The instability of the $\mathbf{P}_2/P_0$ element comes from a single pressure mode on elements with the area behaving as $\mathcal{O}(b^2)$ (see, e.g., Fig. C.5 and C.7). This element fails for both problems. It implies that spurious modes are not concentrated only in corners on which Dirichlet boundary conditions are imposed. Also, all spurious modes have a dependence on $1/\sqrt{b}$.

The instability of $\mathbf{P}_2/P_1$ comes from a single rogue pressure mode on corners with Dirichlet boundary conditions (see Figures C.11 and C.13). Indeed, for Problem 2 and for Problem 1 with the Mesh 3, the pair is stable for all tests, even when the smallest element area is $\mathcal{O}(b^2)$. These results are in accordance with the observations made in Chapter 3. Convergence rates of the spurious modes have a dependence on $1/\sqrt{b}$.

The $\mathbf{P}_2^+/P_1$ element passes all tests.

The $\mathbf{P}_2^+/P_1^d$ element is the only one that fails for all tests. Furthermore, this element does not only have spurious modes with a dependence on $1/\sqrt{a}$ and $1/\sqrt{b}$ but also with a dependence on $1/b$ and $1/a$. In particular, this result implies that the condition number of the Schur complement would be much larger than for the other finite elements. We also observe that the number of spurious modes with an order $1/2$ corresponds to the number of spurious modes of the $\mathbf{P}_2/P_0$ element.

Mesh:		1	2	3
$a \to 0$	$\mathbf{P}_2/P_0$	P	P	P
	$\mathbf{P}_2/P_1$	P	P	P
	$\mathbf{P}_2^+/P_1$	P	P	P
	$\mathbf{P}_2^+/P_1^d$	2	2	2
$b \to 0$	$\mathbf{P}_2/P_0$	2	2	1
	$\mathbf{P}_2/P_1$	1	2	P
	$\mathbf{P}_2^+/P_1$	P	P	P
	$\mathbf{P}_2^+/P_1^d$	5	5	4

(a) Problem 1: with Dirichlet boundary conditions on $y = \pm 1$.

Mesh		1	2	3
$a \to 0$	$\mathbf{P}_2/P_0$	P	P	P
	$\mathbf{P}_2/P_1$	P	P	P
	$\mathbf{P}_2^+/P_1$	P	P	P
	$\mathbf{P}_2^+/P_1^d$	2	2	2
$b \to 0$	$\mathbf{P}_2/P_0$	1	P	1
	$\mathbf{P}_2/P_1$	P	P	P
	$\mathbf{P}_2^+/P_1$	P	P	P
	$\mathbf{P}_2^+/P_1^d$	2	1	2

(b) Problem 2: with Neumann boundary conditions on $y = \pm 1$.

TABLE C.1. Summary of the results: if an element passes the test it is denoted by P. On the contrary, if an element fails the test the table shows the number of spurious modes.

C.5. Eigenvalues and eigenvectors representation

Problem 1 (Dirichlet on $y = \pm 1$) with $\mathbf{P}_2/P_0$ for $b \to 0$ and Mesh 1

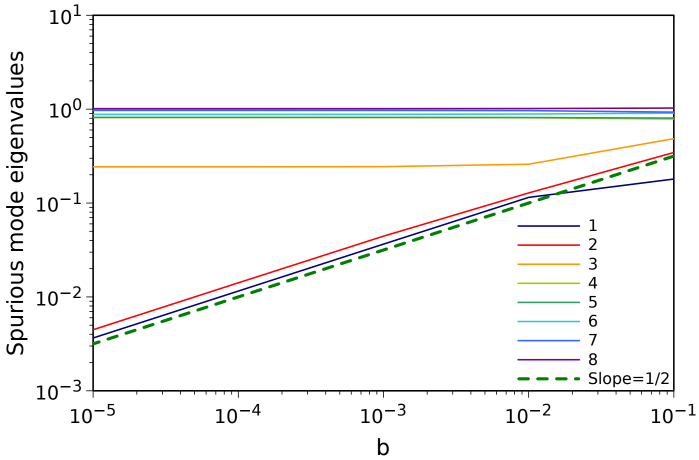

FIGURE C.4. There are 2 order 1/2 spurious modes.

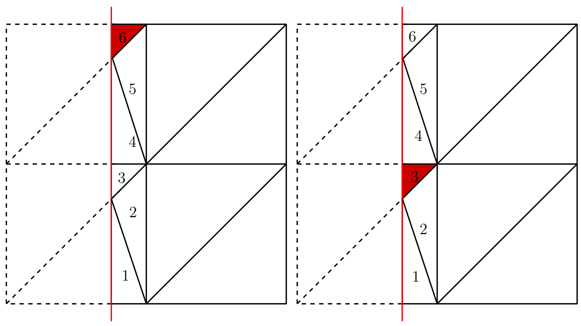

(a) Mode 1.

(b) Mode 2.

FIGURE C.5. Spurious modes are clearly located on elements with the smallest areas.

Problem 1 (Dirichlet on $y = \pm 1$) with $\mathbf{P}_2/P_0$ for $b \to 0$ and Mesh 2

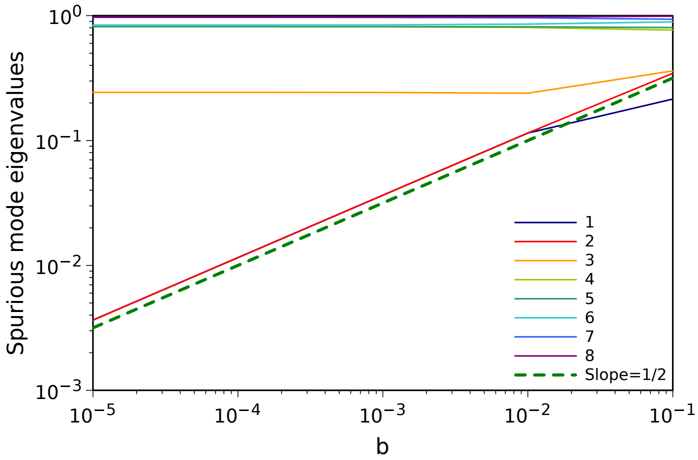

FIGURE C.6. There are 2 order 1/2 spurious modes.

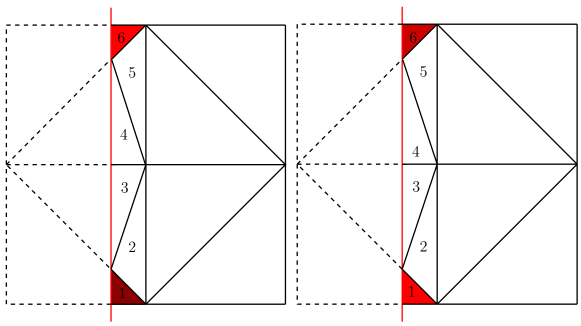

(a) Mode 1.

(b) Mode 2.

FIGURE C.7. Spurious modes: in the top and bottom corners.

Problem 1 (Dirichlet on $y = \pm 1$) for $\mathbf{P}_2/P_0$ with $b \to 0$ and Mesh 3

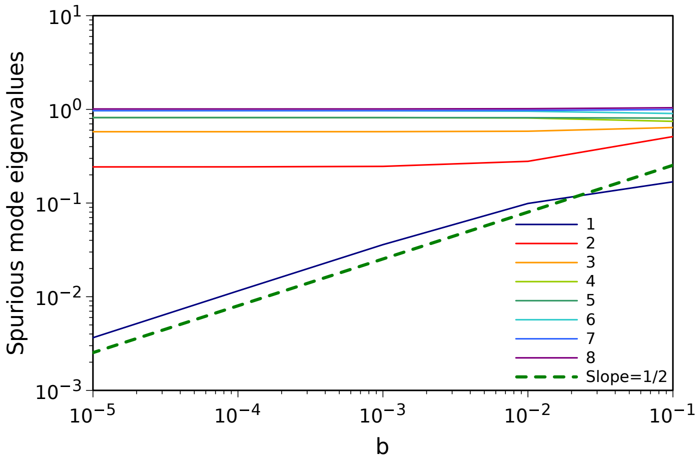

FIGURE C.8. There is 1 order 1/2 spurious mode.

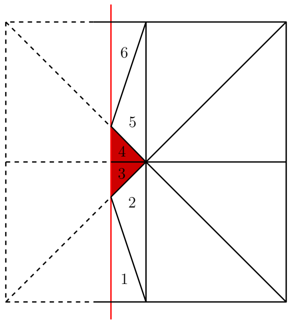

FIGURE C.9. In this test there is only one mode over both elements 3 and 4.

Problem 1 (Dirichlet on $y = \pm 1$) for $\mathbf{P}_2/P_1$ with $b \to 0$ and Mesh 1

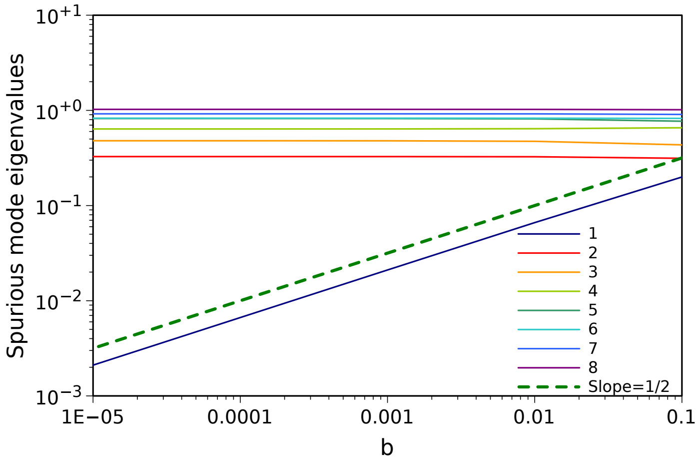

FIGURE C.10. There is 1 order 1/2 spurious mode.

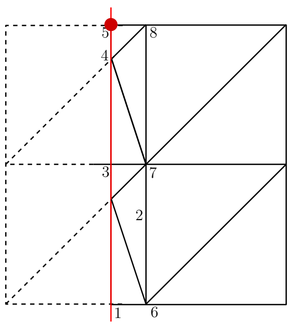

FIGURE C.11. The spurious mode is localized only on the node that is on the smallest element area and not connected to other elements. This result is in accordance with the results of more general test performed in Chapter 3. This test provide a clear location for the spurious mode.

Problem 1 (Dirichlet on $y = \pm 1$) for $\mathbf{P}_2/P_1$ with $b \to 0$ and Mesh 2

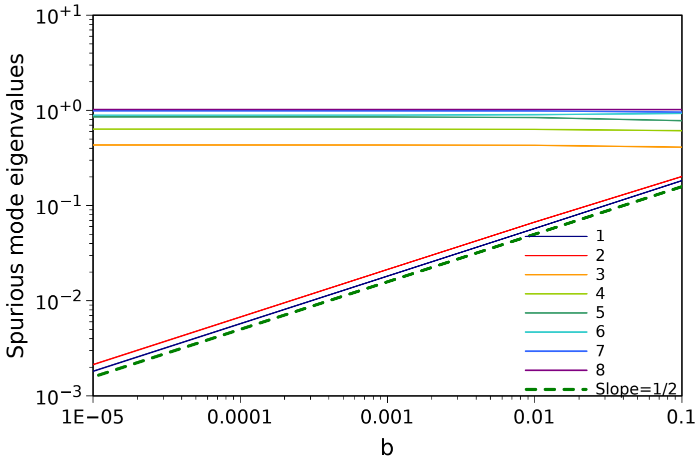

FIGURE C.12. There are 2 order 1/2 spurious modes.

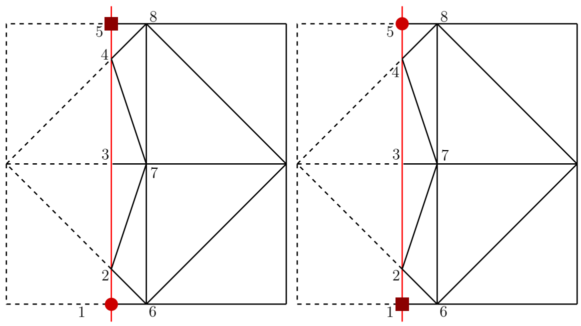

(a) Mode 1: $\mathcal{O}(\sqrt{b})$. (b) Mode 2: $\mathcal{O}(\sqrt{b})$.

FIGURE C.13. This result is consistent with the results of Problem 1 with Mesh 1. Indeed, we have two elements in corners and thus two spurious modes. For Problem 1 with Mesh 3 there are no elements in a corner and as consequence the element is stable.

Problem 1 (Dirichlet on $y = \pm 1$) for $\mathbf{P}_2^+/P_1^d$ with $a \to 0$ and Mesh 1

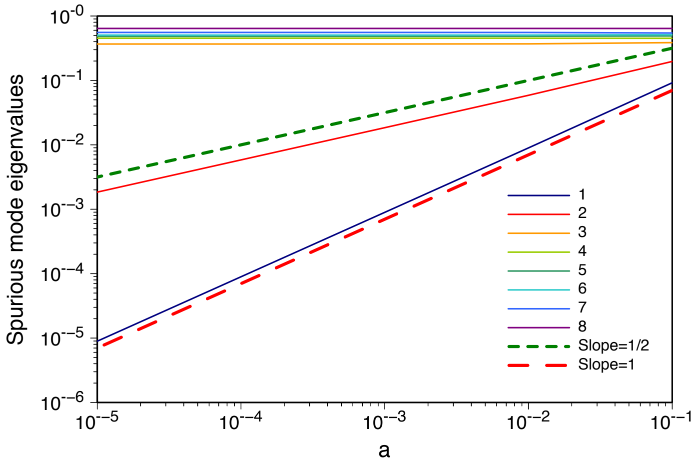

FIGURE C.14. There is are order 1 and one order 1/2 spurious modes.

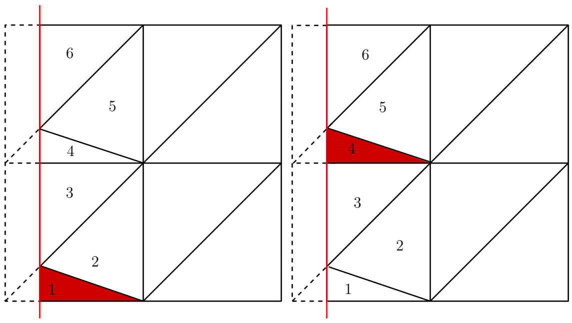

(a) Mode 1: $\mathcal{O}(a)$. (b) Mode 2: $\mathcal{O}(\sqrt{a})$.

FIGURE C.15. Notice that the order 1 spurious mode is located on the element which have two edges with a Dirichlet boundary condition enforced. On the contrary, the order 1/2 spurious mode is located on the element with only one edge constrained by a Dirichlet boundary condition. In Problem 2, both distorted elements have a spurious mode but with a degeneracy of order 1/2.

Problem 1 (Dirichlet on $y = \pm 1$) for $\mathbf{P}_2^+/P_1^d$ with $a \to 0$ and Mesh 2

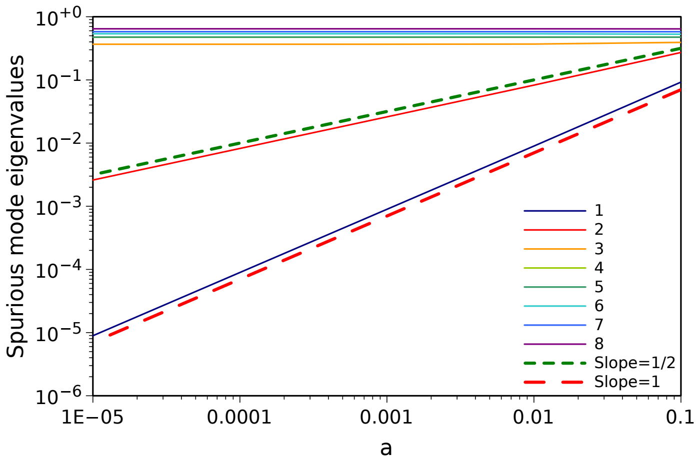

FIGURE C.16. There are 1 order 1 and 1 order 1/2 spurious modes.

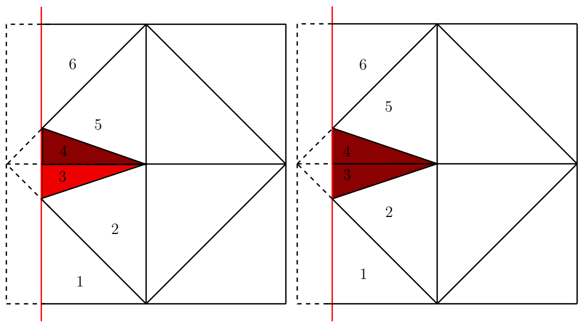

(a) Mode 1: $\mathcal{O}(a)$. (b) Mode 2: $\mathcal{O}(\sqrt{a})$.

FIGURE C.17. In this example, none of the distorted elements have Dirichlet boundary conditions on two of their edges. Nonetheless, this element has an order 1 spurious mode. This result is important since it indicates that it is not only in corners that this element shows a much faster degeneracy of the numerical inf-sup constant with respect to the other elements. An identical result is obtained for Problem 2 with Mesh 2 as $a \to 0$.

Problem 1 (Dirichlet on $y = \pm 1$) for $\mathbf{P}_2^+/P_1^d$ with $a \to 0$ and Mesh 3

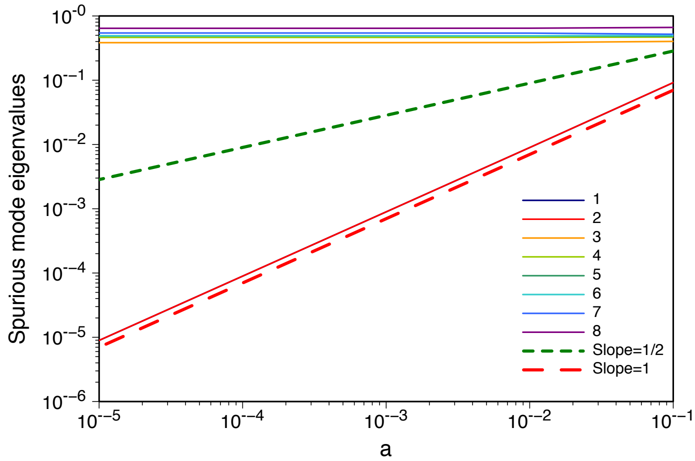

FIGURE C.18. There are 2 order 1 spurious modes. In this case, spurious modes are located on elements with an edge on $y \pm 1$.

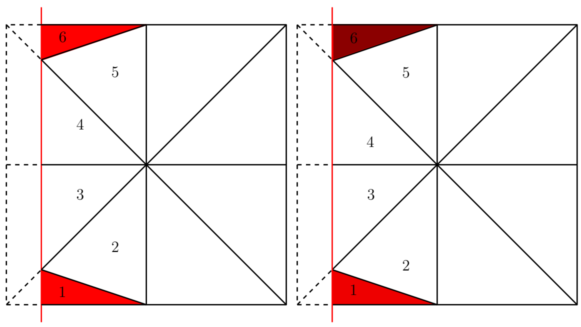

(a) Mode 1: $\mathcal{O}(a)$. (b) Mode 2: $\mathcal{O}(a)$.

FIGURE C.19. This result is consistent with Problem 1 with Mesh 1 as $a \to 0$ which has a spurious mode of $\mathcal{O}(a)$ on the distorted corner element. In this case we have two $\mathcal{O}(a)$ spurious modes since the two distorted elements are in corners with Dirichlet boundary conditions on both their edges. As we shall see with Problem 2, there are two spurious modes with this problem but both with orders 1/2 since there are Dirichlet boundary conditions only on one edge.

Problem 1 (Dirichlet on $y = \pm 1$) for $\mathbf{P}_2^+/P_1^d$ with $b \to 0$ and Mesh 1

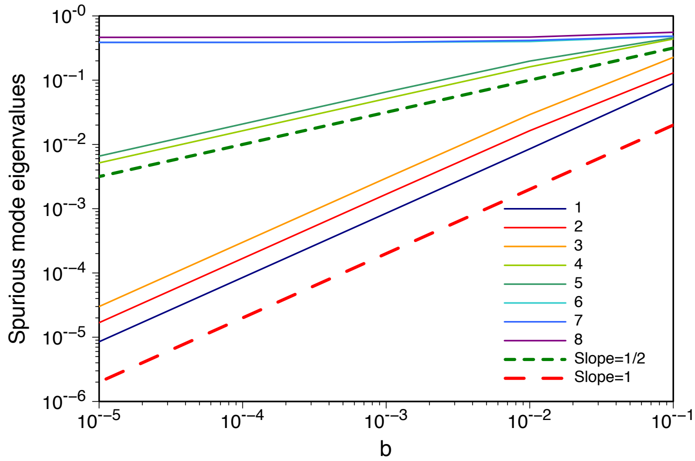

FIGURE C.20. There are 5 spurious modes: 3 order 1 and 2 order 1/2.

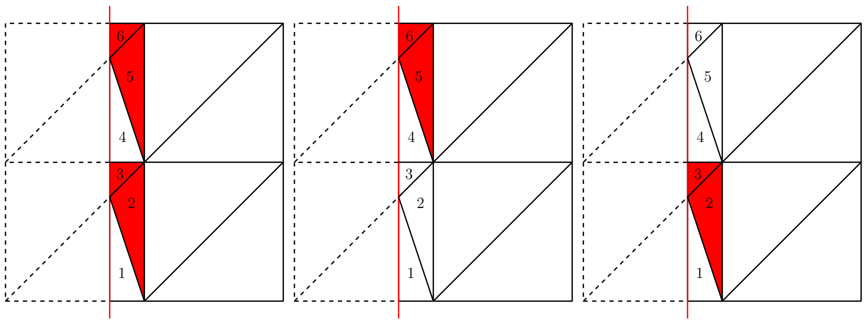

(a) Modes dx 1 to 3: $\mathcal{O}(b)$. (b) Mode dx 4: $\mathcal{O}(\sqrt{b})$. (c) Mode dx 5: $\mathcal{O}(\sqrt{b})$.

FIGURE C.21. Spurious modes for $\mathbf{P}_2^+/P_1^d$ modes are difficult to analyze. For this case we only depict the dx modes. See the eigenvectors in Section C.6 for more details.

Problem 1 (Dirichlet on $y = \pm 1$) for $\mathbf{P}_2^+/P_1^d$ with $b \to 0$ and Mesh 2

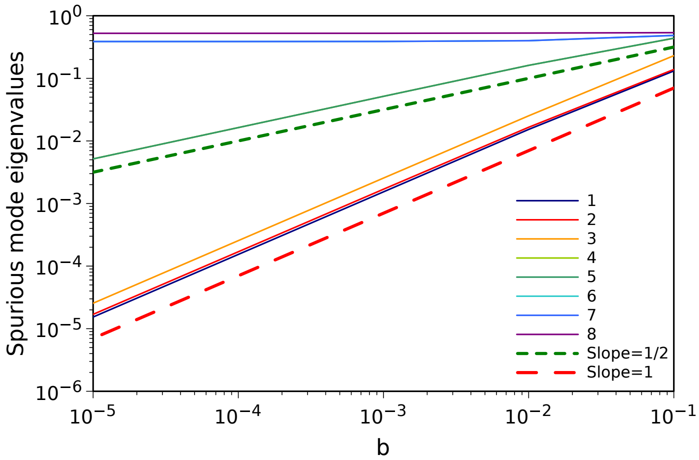

FIGURE C.22. There are 5 spurious modes: 3 order 1 and 2 order 1/2.

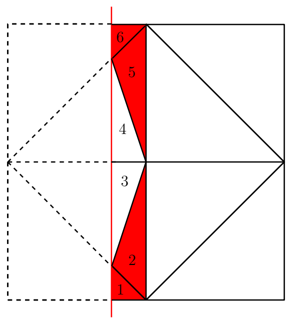

FIGURE C.23. Representation for all cst and dx spurious modes.

Problem 1 (Dirichlet on $y = \pm 1$) for $\mathbf{P}_2^+/P_1^d$ with $b \to 0$ and Mesh 3

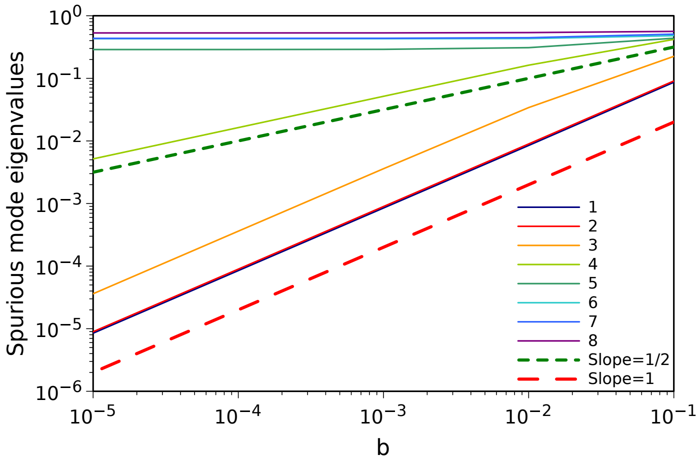

FIGURE C.24. There are 4 spurious modes: 3 order 1 and 1 order 1/2. By comparing the results from Problem 1 and 2 for $b \to 0$ and Mesh 3 we deduce that the first two modes result from the Dirichlet BCs on $y \pm 1$ while the last two are also present with Neumann BCs on $y \pm 1$.

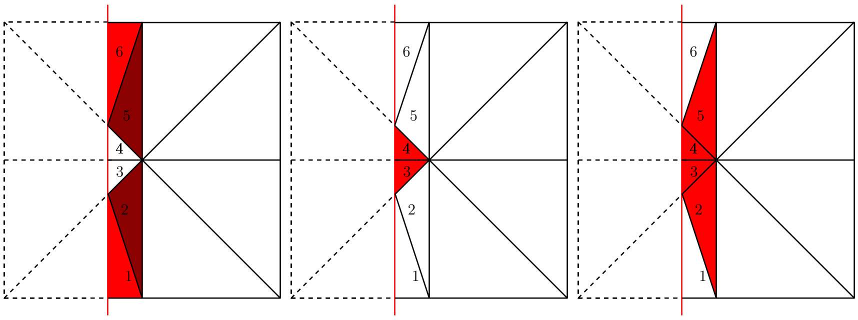

(a) Constant spurious modes 1 to 3: $\mathcal{O}(b)$.

(b) Representation for the constant and dy mode 4: $\mathcal{O}(\sqrt{b})$.

(c) Representation for the dx mode 4: $\mathcal{O}(\sqrt{b})$.

FIGURE C.25. For spurious modes 1 to 3 (i.e., $\mathcal{O}(b)$) a representation for the modes dx and dy is not clear. We invite the reader to look at the numerical values of the eigenvectors in Section C.6. Notice that for the mode 4 ($\mathcal{O}(b)$) the constant spurious mode corresponds to the position of the spurious modes of the $\mathbf{P}_2/P_0$ element for the same problem.

Problem 2 (Neumann on $y = \pm 1$) for $\mathbf{P}_2/P_0$ with $b \to 0$ and Mesh 1

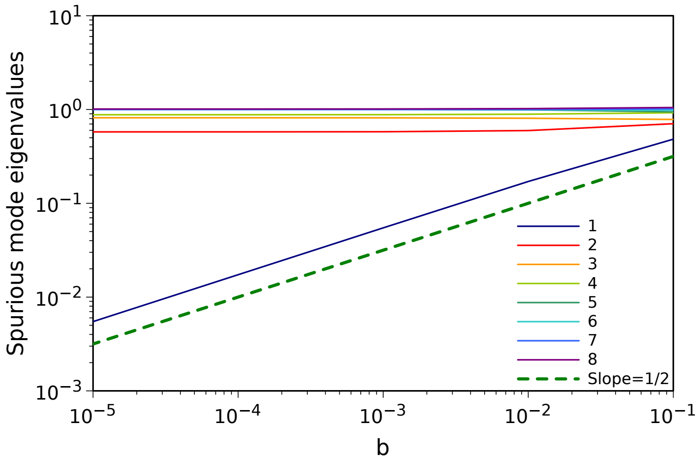

FIGURE C.26. There is 1 order $1/2$ spurious mode. For Problem 1 there are two modes located on elements 3 and 6.

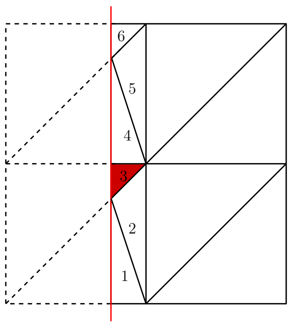

FIGURE C.27. The single spurious mode is not on the element with an edge on $y = 1$. The spurious mode is located near two elements which are distorted. This result is important since it indicates, on the contrary to the $\mathbf{P}_2/P_1$, that the tested element may be unstable when only one edge is constrained. We also notice, with respect to Problem 1, that there is no spurious mode on element 6. Indeed, for Problem 2 with Mesh 2 $\mathbf{P}_2/P_0$ is stable.

Problem 2 (Neumann on $y = \pm 1$) for $\mathbf{P}_2/P_0$ with $b \to 0$ and Mesh 3

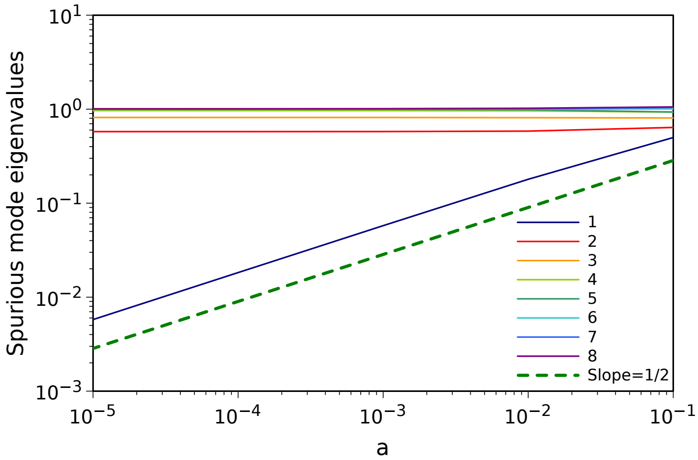

FIGURE C.28. There is 1 order 1/2 spurious mode. In this case, identical results with Problem 1 are obtained.

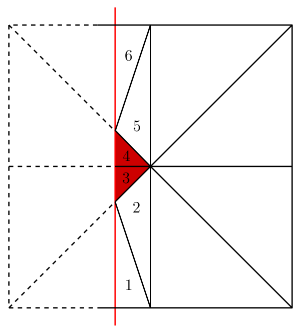

FIGURE C.29. Spurious mode locations: identical to the results with Problem 1.

Problem 2 (Neumann on $y = \pm 1$) for $\mathbf{P}_2^+/P_1^d$ with $a \to 0$ and Mesh 1

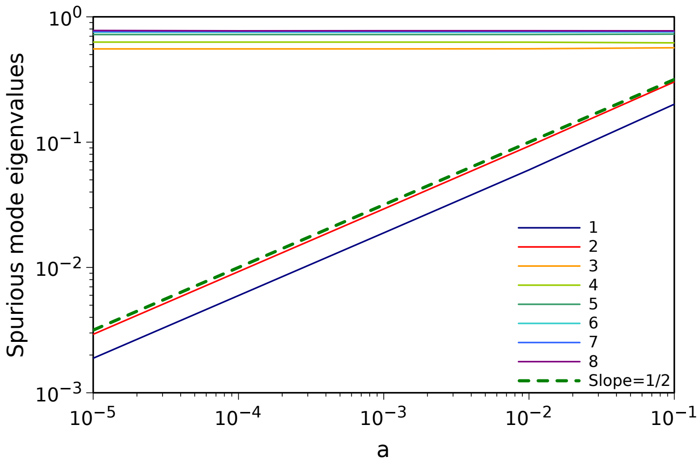

FIGURE C.30. There are 2 order 1/2 spurious modes. For this problem there are only 2 order 1/2 modes since there is no Dirichlet boundary conditions on $y\pm 1$. On the contrary, in Problem 1, there is 1 order 1 spurious mode, since there is one element on which it is imposed Dirichlet boundary conditions on two edges.

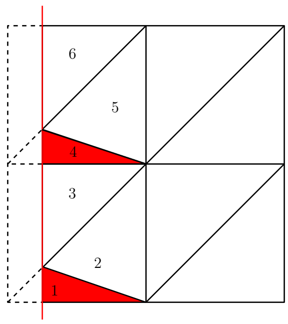

FIGURE C.31. Representation for cst and dx modes 1 and 2.

Problem 2 (Neumann on $y = \pm 1$) for $\mathbf{P}_2^+/P_1^d$ with $a \to 0$ and Mesh 2

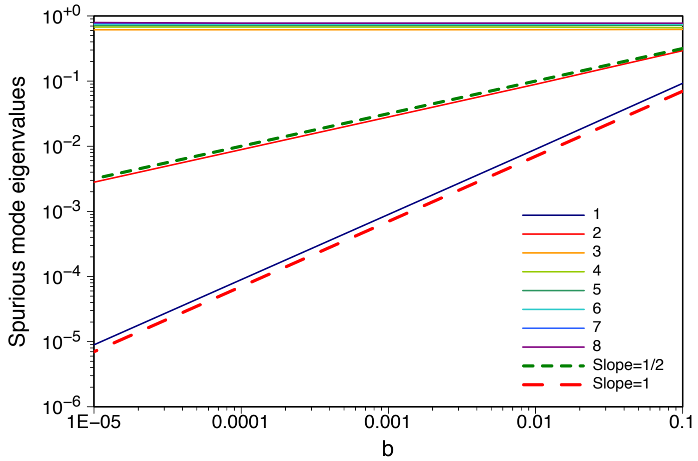

FIGURE C.32. There are 2 spurious modes: 1 order 1 and 1 order 1/2. For both Problem 1 and Problem 2 the spurious modes are not located on elements with an edge on $y \pm 1$ and as a consequence results are identical. Again, this result indicates that the $\mathbf{P}_2^+/P_1^d$ element has an order 1 inf-sup constant not only with Dirichlet boundary conditions in corners of the mesh.

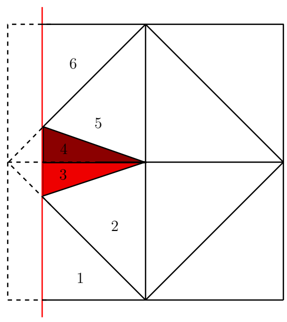

FIGURE C.33. Representation for spurious modes 1 and 2 (identical to the result of Problem 1).

Problem 2 (Neumann on $y = \pm 1$) for $\mathbf{P}_2^+/P_1^d$ with $a \to 0$ and Mesh 3

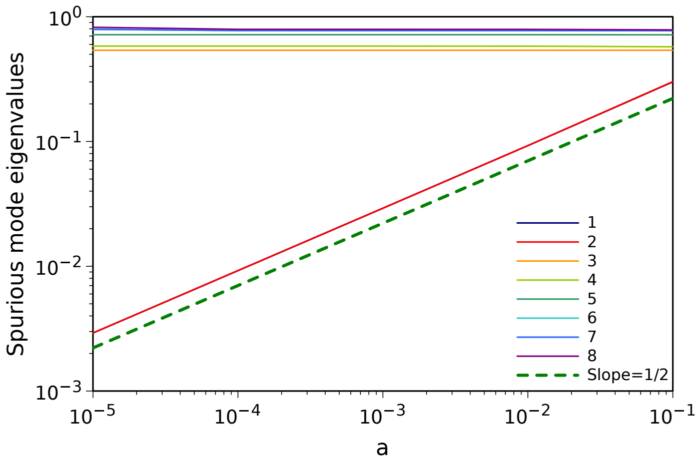

FIGURE C.34. There are 2 spurious modes: 2 order 1/2. We recall that for Problem 1 there are 2 order 1 modes. The two problems differ by the boundary conditions on $y \pm 1$. As for the case with Mesh 1, Dirichlet boundary conditions in corners (i.e., the degrees of freedom are only on one edge) imply an order 1 mode, and an order 1/2 mode if there are degrees of freedoms on two edges.

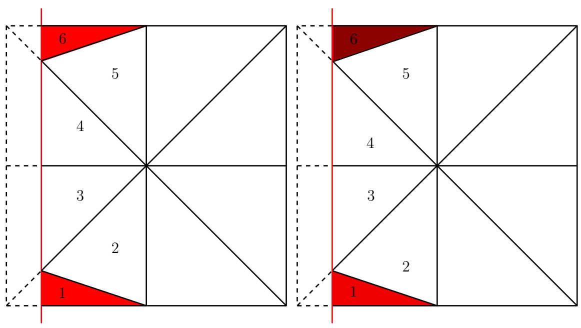

(a) Mode 1:

(b) Mode 2:

FIGURE C.35. Representation for spurious modes 1 and 2 (identical to the results of Problem 1).

Problem 2 (Neumann on $y = \pm 1$) for $\mathbf{P}_2^+/P_1^d$ with $b \to 0$ and Mesh 1

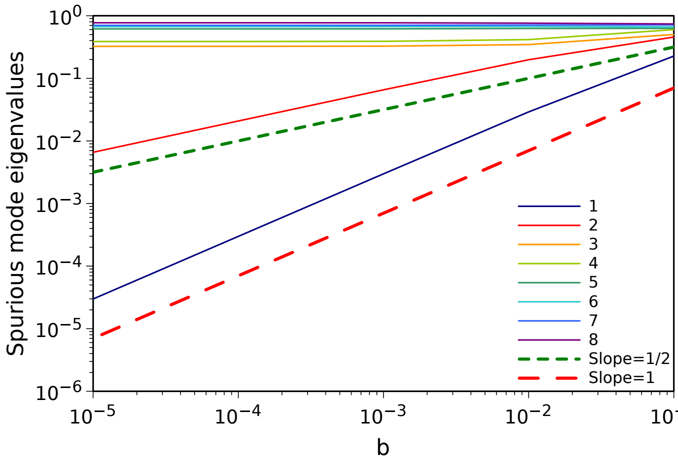

FIGURE C.36. There are 2 spurious modes: 1 order 1 and 1 order 1/2.

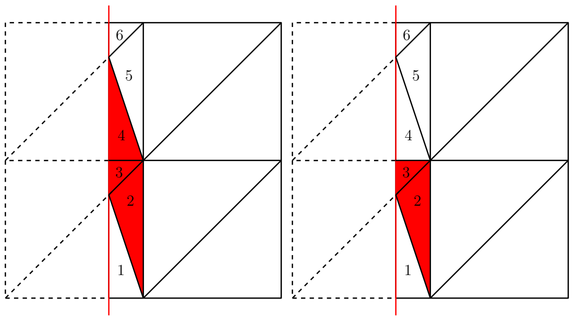

(a) Constant and dy

(b) dx

FIGURE C.37. Representation for spurious modes 1 and 2.

Problem 2 (Neumann on $y = \pm 1$) for $\mathbf{P}_2^+/P_1^d$ with $b \to 0$ and Mesh 2

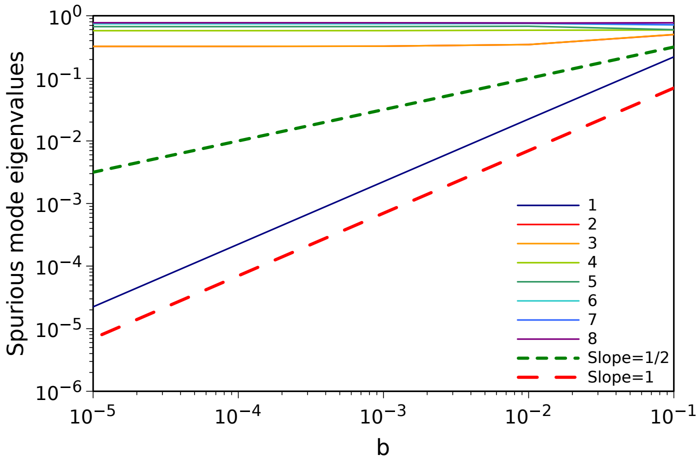

FIGURE C.38. There is 1 spurious mode: 1 order 1.

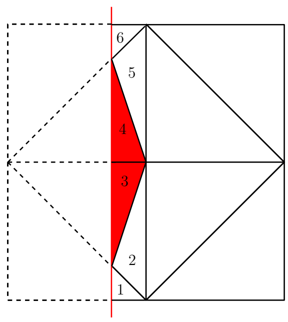

FIGURE C.39. Spurious cst and dy modes representation. For the dx spurious mode all elements are affected.

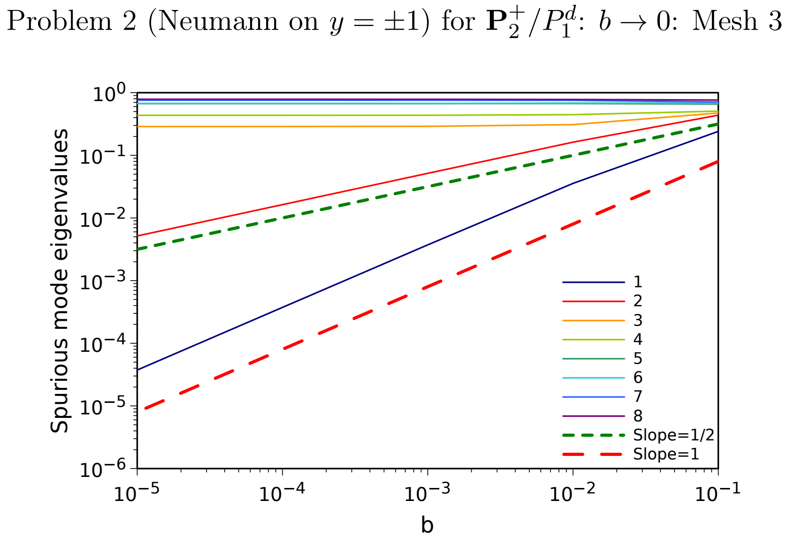

FIGURE C.40. There is 2 modes: 1 order 1 and 1 order 1/2.

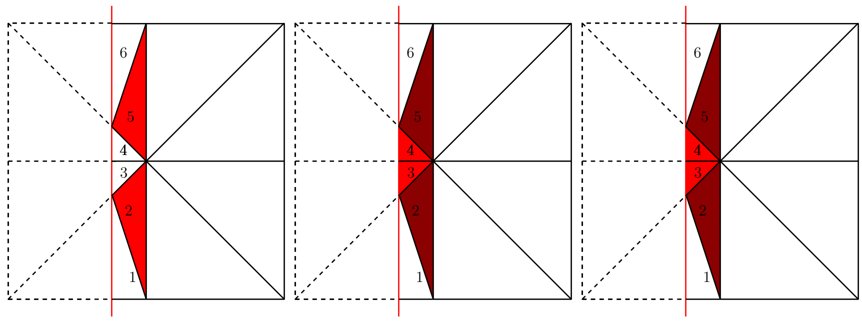

(a) Constant and dy (b) dx (c) dy

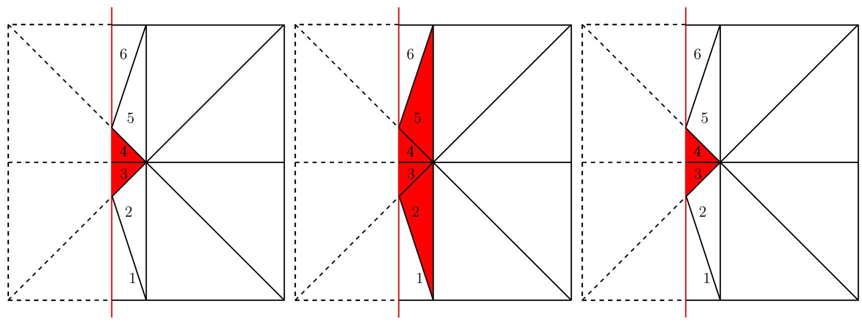

(d) Constant and dy (e) dx (f) dy

FIGURE C.41. Representation for spurious modes 1 $\mathcal{O}(b)$ (top) and 2 $\mathcal{O}(\sqrt{b})$ (bottom). Notice that the cst spurious mode scales as $b^{1/2}$ at the exact same location as with $\mathbf{P}_2/P_0$.

β_h	3.65e-03	5.44e-03	6.26e-01	7.46e-01
1	-3.09e-16	-4.71e-11	7.17e-02	-7.32e-01
2	-2.52e-12	-5.00e-06	-1.33e-01	-5.61e-01
3	5.04e-07	1.00e+00	1.81e-06	-1.86e-06
4	-2.52e-12	-5.00e-06	4.95e-01	1.90e-01
5	1.00e-10	-1.41e-10	6.99e-01	2.00e-02
6	1.00e+00	-5.04e-07	-6.99e-11	-2.00e-12

TABLE C.2. Problem 1 with $\mathbf{P}_2/P_0$ for $b \to 0$ and Mesh 1.

β_h	3.65e-03	3.65e-03	8.16e-01	8.16e-01
1	-6.31e-01	-7.76e-01	4.81e-11	-5.19e-11
2	-6.31e-11	-7.76e-11	-4.80e-01	5.19e-01
3	-1.00e-15	1.00e-15	-5.19e-01	-4.80e-01
4	1.00e-15	1.00e-15	5.19e-01	4.80e-01
5	7.76e-11	-6.31e-11	4.80e-01	-5.19e-01
6	7.76e-01	-6.31e-01	-4.81e-11	5.19e-11

TABLE C.3. Problem 1 with $\mathbf{P}_2/P_0$ for $b \to 0$ and Mesh 2.

β_h	3.65e-03	2.43e-01	5.77e-01	8.16e-01
1	-4.24e-05	7.65e-01	1.42e-05	-1.88e-01
2	-4.24e-05	6.30e-01	1.17e-05	1.88e-01
3	7.07e-01	5.50e-05	-7.07e-01	-1.44e-10
4	7.07e-01	2.87e-05	7.07e-01	-1.06e-10
5	1.63e-09	-1.36e-01	-2.51e-06	-1.88e-01
6	2.10e-14	-2.03e-06	-3.76e-11	-9.46e-01

TABLE C.4. Problem 1 with $\mathbf{P}_2/P_0$ for $b \to 0$ and Mesh 3.

C.6. Spurious mode eigenvectors

β_h	2.11e-03	3.27e-01	4.80e-01	6.38e-01
1	-1.11e-06	9.41e-01	-1.71e-01	-1.92e-01
2	5.56e-07	-2.98e-01	-5.97e-02	-4.35e-01
3	-1.67e-06	1.53e-01	7.55e-01	3.26e-01
4	2.22e-06	-5.33e-02	-5.04e-01	-8.58e-03
5	-1.00e+00	-1.58e-06	-2.22e-06	-5.92e-07
6	1.69e-12	1.15e-06	-6.95e-02	1.50e-01
7	2.83e-12	-7.36e-08	1.87e-01	-4.04e-01
8	-4.47e-11	2.02e-08	-3.17e-01	6.83e-01

TABLE C.5. Problem 1 with $\mathbf{P}_2/P_1$ for $b \to 0$ and Mesh 1.

β_h	1.81e-03	2.13e-03	4.33e-01	6.35e-01
1	9.99e-01	-3.33e-02	-6.84e-06	2.57e-07
2	-6.84e-06	6.08e-08	-1.00e+00	-1.81e-02
3	5.16e-07	4.83e-07	2.32e-02	-5.28e-01
4	-2.28e-07	-1.83e-06	-8.38e-03	7.04e-01
5	3.33e-02	9.99e-01	-1.94e-07	1.55e-06
6	3.80e-14	-5.39e-12	-3.87e-06	2.10e-01
7	-4.15e-12	1.93e-11	-1.46e-06	-3.50e-01
8	3.39e-13	3.63e-12	5.20e-07	2.10e-01

TABLE C.6. Problem 1 with $\mathbf{P}_2/P_1$ for $b \to 0$ and Mesh 2.

β_h	8.94e-06	1.84e-03	3.67e-01	4.52e-01
cst				
1	4.47e-01	-2.89e-07	3.46e-02	-1.12e-02
2	-1.51e-11	9.06e-08	9.13e-02	-2.00e-01
3	6.93e-12	2.35e-06	-3.16e-01	-6.68e-02
4	-5.63e-07	-4.47e-01	-1.70e-01	-9.06e-02
5	1.56e-12	1.90e-06	-7.33e-02	-8.04e-02
6	2.23e-12	-8.17e-07	-2.71e-02	7.45e-02
dx				
1	8.94e-01	9.64e-07	-1.73e-02	-5.60e-03
2	-1.38e-10	4.34e-07	2.63e-01	-4.85e-03
3	-1.25e-11	5.92e-06	-1.93e-01	-2.05e-02
4	1.10e-06	-8.94e-01	8.50e-02	-4.53e-0
5	-2.14e-11	4.69e-06	3.13e-01	1.19e-02
6	9.51e-12	2.28e-07	-2.07e-01	-4.79e-01
dy				
1	-1.19e-05	6.24e-07	3.33e-01	-1.85e-01
2	3.44e-11	1.84e-07	2.76e-01	1.56e-02
3	-3.01e-11	-1.80e-06	-6.72e-02	-2.73e-01
4	-2.35e-11	4.15e-06	1.66e-01	-1.44e-02
5	-2.07e-12	-1.64e-06	1.17e-01	3.44e-01
6	9.51e-12	2.28e-07	-4.49e-01	8.13e-02

TABLE C.7. Problem 1 with $\mathbf{P}_2^+/P_1^d$ for $a \to 0$ and Mesh 1.

β_h	8.94e-06	2.60e-03	3.67e-01	4.74e-01
cst				
1	1.19e-11	-1.52e-06	-3.42e-02	-4.80e-02
2	-3.71e-11	2.97e-06	-1.42e-01	1.48e-01
3	3.16e-01	-3.16e-01	-1.92e-01	8.79e-02
4	-3.16e-01	-3.16e-01	-1.92e-01	8.79e-02
5	3.71e-11	2.97e-06	-1.42e-01	1.48e-01
6	-1.19e-11	-1.52e-06	-3.42e-02	-4.80e-02
dx				
1	-1.32e-11	-3.13e-07	-2.04e-01	-4.77e-01
2	-7.50e-11	8.19e-06	2.19e-01	1.04e-01
3	6.32e-01	-6.32e-01	9.59e-02	-4.40e-02
4	-6.32e-01	-6.32e-01	9.59e-02	-4.40e-02
5	7.50e-11	8.19e-06	2.19e-01	1.04e-01
6	1.32e-11	-3.13e-07	-2.04e-01	-4.77e-01
dy				
1	1.32e-11	3.13e-07	5.03e-01	5.20e-02
2	-3.74e-11	2.40e-06	-9.77e-02	-1.65e-01
3	-2.36e-06	-8.18e-06	9.26e-07	-3.08e-06
4	-1.39e-06	9.15e-06	-2.85e-06	4.82e-06
5	-3.74e-11	-2.40e-06	9.77e-02	1.65e-01
6	1.32e-11	-3.13e-07	-5.03e-01	-5.20e-02

TABLE C.8. Problem 1 with $\mathbf{P}_2^+/P_1^d$ for $a \to 0$ and Mesh 2.

β_h	8.94e-06	8.94e-06	3.84e-01	4.64e-01
cst				
1	1.73e-01	-4.12e-01	-6.63e-02	1.31e-01
2	-1.32e-11	1.00e-11	-3.98e-02	1.03e-01
3	1.19e-11	1.92e-12	2.54e-01	-4.82e-02
4	7.17e-12	-9.70e-12	2.54e-01	-4.82e-02
5	-1.65e-11	2.09e-12	-3.98e-02	1.03e-01
6	4.12e-01	1.73e-01	-6.64e-02	1.31e-01
dx				
1	3.47e-01	-8.24e-01	3.32e-02	-6.54e-02
2	-6.52e-11	1.26e-10	-2.76e-01	1.39e-01
3	1.56e-12	1.07e-11	4.89e-02	-6.32e-02
4	-6.34e-12	-8.71e-12	4.89e-02	-6.32e-02
5	-1.34e-10	-4.42e-11	-2.76e-01	1.39e-01
6	8.24e-01	3.47e-01	3.32e-02	-6.54e-02
dy				
1	2.18e-06	9.20e-07	-4.26e-01	1.63e-02
2	6.49e-12	-4.09e-11	-2.68e-01	-1.31e-01
3	1.16e-12	3.16e-11	-3.84e-03	-3.07e-01
4	2.13e-11	2.34e-11	3.84e-03	3.07e-01
5	-3.32e-11	-2.47e-11	2.68e-01	1.31e-01
6	-6.85e-06	-2.88e-06	4.26e-01	-1.63e-02

TABLE C.9. Problem 1 with $\mathbf{P}_2^+/P_1^d$ for $a \to 0$ and Mesh 3.

β_h	8.50e-06	1.68e-05	3.00e-05	5.16e-03	6.58e-03	3.87e-01
cst						
1	-3.08e-01	-2.52e-01	2.05e-01	1.59e-11	-6.51e-06	4.31e-11
2	2.37e-02	-1.39e-02	1.84e-02	3.01e-07	-4.75e-02	-2.13e-06
3	5.45e-03	-3.21e-03	4.25e-03	1.44e-07	3.03e-02	8.13e-09
4	-2.37e-02	1.39e-02	-1.84e-02	3.03e-07	4.75e-02	-1.64e-06
5	2.23e-02	-1.32e-01	-1.28e-01	-6.04e-02	2.36e-06	3.77e-01
6	-7.52e-02	4.45e-01	4.33e-01	2.83e-01	-8.27e-06	1.51e-01
dx						
1	-3.17e-07	-1.37e-06	1.35e-06	8.33e-12	-1.58e-06	-6.03e-11
2	-7.28e-02	4.28e-02	-5.66e-02	-1.23e-06	3.11e-01	1.23e-05
3	-3.64e-01	2.14e-01	-2.83e-01	-5.65e-06	-8.28e-01	2.56e-06
4	2.10e-06	2.33e-06	6.00e-06	1.81e-06	8.66e-06	-1.13e-05
5	1.11e-02	-6.59e-02	-6.41e-02	-2.89e-01	2.15e-06	8.84e-02
6	5.57e-02	-3.30e-01	-3.21e-01	8.55e-01	2.12e-06	-6.14e-02
dy						
1	-6.15e-01	-5.03e-01	4.10e-01	4.85e-11	-1.40e-05	-2.21e-11
2	4.73e-02	-2.78e-02	3.68e-02	6.02e-07	-9.50e-02	-4.25e-06
3	-6.08e-01	3.57e-01	-4.73e-01	-1.50e-06	4.40e-01	-2.51e-06
4	4.73e-02	-2.78e-02	3.68e-02	-1.81e-06	-9.50e-02	1.08e-05
5	-4.46e-02	2.64e-01	2.56e-01	1.21e-01	-4.73e-06	-7.54e-01
6	5.57e-02	-3.30e-01	-3.20e-01	-2.95e-01	6.45e-06	-5.06e-01

TABLE C.10. Problem 1 with $\mathbf{P}_2^+/P_1^d$ for $b \to 0$ and Mesh 1.

β_h	1.54e-05	1.70e-05	2.55e-05	5.16e-03	5.16e-03	3.87e-01
cst						
1	4.22e-01	4.42e-01	-1.32e-01	1.77e-01	1.77e-01	-4.17e-03
2	-1.25e-01	-1.31e-01	3.92e-02	-3.78e-02	-3.78e-02	-1.04e-02
3	9.47e-02	2.79e-06	3.02e-01	2.04e-06	2.04e-06	3.04e-08
4	-9.47e-02	-1.72e-07	-3.02e-01	-1.19e-06	-1.19e-06	9.57e-08
5	1.25e-01	-1.31e-01	-3.92e-02	-4.71e-02	-4.71e-02	-2.22e-03
6	-4.22e-01	4.42e-01	1.32e-01	2.21e-01	2.21e-01	-8.91e-04
dy						
1	-3.12e-01	-3.27e-01	9.81e-02	5.35e-01	5.35e-01	1.69e-03
2	-6.25e-02	-6.55e-02	1.96e-02	-1.81e-01	-1.81e-01	-2.44e-03
3	2.09e-06	2.62e-06	-2.25e-05	5.36e-07	5.36e-07	3.98e-07
4	-1.95e-06	2.62e-06	2.29e-05	1.16e-06	1.16e-06	-1.46e-07
5	6.25e-02	-6.55e-02	-1.96e-02	-2.25e-01	-2.25e-01	-5.21e-04
6	3.12e-01	-3.27e-01	-9.81e-02	6.67e-01	6.67e-01	3.62e-04
dy						
1	3.12e-01	3.27e-01	-9.80e-02	1.84e-01	1.84e-01	-1.39e-02
2	-2.50e-01	-2.62e-01	7.84e-02	-7.55e-02	-7.55e-02	-2.08e-02
3	1.89e-01	8.20e-06	6.03e-01	4.83e-06	4.83e-06	2.69e-07
4	1.89e-01	-2.28e-06	6.03e-01	1.43e-06	1.43e-06	-2.36e-07
5	-2.50e-01	2.62e-01	7.84e-02	9.43e-02	9.43e-02	4.44e-03
6	3.12e-01	-3.27e-01	-9.80e-02	-2.30e-01	-2.30e-01	2.98e-03

TABLE C.11. Problem 1 with $\mathbf{P}_2^+/P_1^d$ for $b \to 0$ and Mesh 2.

β_h	8.48e-06	8.94e-06	3.62e-05	5.16e-03	2.88e-01	4.30e-01
cst						
1	-1.80e-01	3.16e-01	-2.60e-01	3.18e-06	3.18e-06	-4.84e-04
2	1.46e-02	-1.23e-07	-1.01e-02	1.18e-06	1.18e-06	2.80e-03
3	-1.76e-06	1.19e-06	1.22e-06	-1.18e-01	-1.18e-01	1.70e-02
4	1.76e-06	1.19e-06	-1.22e-06	-1.18e-01	-1.18e-01	1.70e-02
5	-1.46e-02	1.23e-07	1.01e-02	1.18e-06	1.18e-06	2.80e-03
6	1.80e-01	3.16e-01	2.60e-01	3.18e-06	3.18e-06	-4.84e-04
dx						
1	-1.59e-07	1.14e-06	-1.27e-06	1.30e-10	1.30e-10	-5.61e-03
2	-5.86e-02	5.23e-06	4.05e-02	-4.72e-01	-4.72e-01	5.98e-02
3	-2.93e-01	-1.97e-06	2.03e-01	4.41e-01	4.41e-01	-3.08e-01
4	2.93e-01	-6.88e-06	-2.03e-01	4.41e-01	4.41e-01	-3.08e-01
5	5.86e-02	4.25e-06	-4.05e-02	-4.72e-01	-4.72e-01	5.98e-02
6	1.26e-06	3.08e-06	2.87e-06	1.49e-10	1.49e-10	-5.61e-03
dy						
1	-3.60e-01	6.32e-01	-5.20e-01	6.35e-06	6.35e-06	2.42e-04
2	2.93e-02	-2.46e-07	-2.03e-02	4.72e-06	4.72e-06	6.80e-03
3	-4.98e-01	6.81e-06	3.44e-01	-2.62e-01	-2.62e-01	-6.33e-01
4	-4.98e-01	1.54e-06	3.44e-01	2.62e-01	2.62e-01	6.33e-01
5	2.93e-02	-2.46e-07	-2.03e-02	-4.72e-06	-4.72e-06	-6.80e-03
6	-3.60e-01	-6.32e-01	-5.20e-01	-6.35e-06	-6.35e-06	-2.42e-04

TABLE C.12. Problem 1 with $\mathbf{P}_2^+/P_1^d$ for $b \to 0$ and Mesh 3.

β_h	5.48e-03	5.77e-01	8.16e-01	8.80e-01
P0				
1	1.46e-11	-2.43e-11	-8.45e-06	-1.91e-01
2	5.00e-06	-1.58e-10	-7.07e-01	-2.74e-01
3	-1.00e+00	1.83e-10	3.43e-11	-2.74e-06
4	5.00e-06	1.43e-10	7.07e-01	-2.74e-01
5	8.02e-11	1.50e-05	3.93e-05	7.39e-01
6	-1.82e-10	-1.00e+00	8.03e-10	1.11e-05

TABLE C.13. Problem 2 with $\mathbf{P}_2/P_0$ for $b \to 0$ and Mesh 1.

β_h	5.77e-03	5.77e-01	8.16e-01	9.66e-01
P0				
1	3.90e-11	8.03e-16	-1.13e-05	7.00e-01
2	7.07e-06	-8.12e-11	-7.07e-01	-1.24e-05
3	-7.07e-01	-7.07e-01	8.12e-11	2.07e-15
4	-7.07e-01	7.07e-01	-8.12e-11	-1.73e-15
5	7.07e-06	8.12e-11	7.07e-01	1.24e-05
6	3.90e-11	-3.10e-16	1.13e-05	-7.00e-01

TABLE C.14. Problem 2 with $\mathbf{P}_2/P_0$ for $b \to 0$ and Mesh 3.

β_h	1.89e-03	2.93e-03	5.55e-01	6.29e-01
cst				
1	-1.89e-02	-4.47e-01	-4.63e-01	-2.30e-01
2	-8.02e-08	-1.86e-07	-1.20e-01	-9.08e-03
3	2.80e-06	8.65e-07	1.79e-01	-4.11e-02
4	-4.47e-01	1.90e-02	2.66e-02	3.89e-02
5	1.79e-06	-9.57e-08	-7.38e-02	1.10e-01
6	-1.04e-06	-2.23e-08	1.07e-01	-2.68e-01
dx				
1	-3.79e-02	-8.94e-01	2.32e-01	1.15e-01
2	2.99e-07	8.57e-06	-3.77e-02	2.70e-03
3	6.34e-06	1.51e-06	2.44e-01	-2.90e-01
4	-8.94e-01	3.79e-02	-1.33e-02	-1.94e-02
5	3.95e-06	-5.73e-08	-1.90e-01	4.96e-02
6	6.07e-07	-1.26e-07	-8.05e-03	1.38e-01
dy				
1	3.07e-06	1.11e-05	-5.88e-01	-2.84e-01
2	-2.37e-07	-4.48e-06	-1.41e-01	-1.98e-02
3	-1.61e-06	2.95e-06	1.58e-01	2.95e-01
4	3.93e-06	1.10e-07	-3.80e-01	3.85e-01
5	-1.67e-06	9.99e-08	7.33e-02	-3.31e-01
6	1.47e-06	-5.45e-08	-1.33e-01	4.47e-01

TABLE C.15. Problem 2 with $\mathbf{P}_2^+/P_1^d$ for $a \to 0$ and Mesh 1.

β_h	8.95e-06	2.80e-03	6.14e-01	6.76e-01
cst				
1	-2.18e-13	-1.86e-06	2.36e-01	2.72e-01
2	-4.99e-12	3.18e-06	-9.29e-02	-2.71e-02
3	3.16e-01	-3.16e-01	1.31e-06	-8.50e-02
4	-3.16e-01	-3.16e-01	-1.03e-06	-8.50e-02
5	6.56e-11	3.18e-06	9.29e-02	-2.71e-02
6	-3.52e-11	-1.86e-06	-2.36e-01	2.72e-01
dx				
1	-5.07e-12	7.85e-07	-7.48e-02	-1.20e-01
2	-3.24e-12	7.01e-06	-1.43e-01	2.37e-01
3	6.32e-01	-6.32e-01	1.06e-06	4.25e-02
4	-6.32e-01	-6.32e-01	-4.94e-07	4.25e-02
5	1.37e-10	7.01e-06	1.43e-01	2.37e-01
6	2.00e-11	7.85e-07	7.48e-02	-1.20e-01
dy				
1	2.83e-12	-2.44e-06	3.50e-01	4.68e-01
2	-7.70e-12	3.01e-06	-2.04e-01	-3.07e-01
3	-2.36e-06	-8.18e-06	4.58e-01	-1.08e-05
4	-1.39e-06	9.15e-06	4.58e-01	1.15e-05
5	-6.51e-11	-3.01e-06	-2.04e-01	3.07e-01
6	4.93e-11	2.44e-06	3.50e-01	-4.68e-01

TABLE C.16. Problem 2 with $\mathbf{P}_2^+/P_1^d$ for $a \to 0$ and Mesh 2.

β_h	2.92e-03	2.92e-03	5.39e-01	5.82e-01
cst				
1	-3.16e-01	-3.16e-01	3.97e-01	4.21e-01
2	-2.34e-08	-1.62e-07	3.15e-02	4.14e-02
3	4.24e-07	8.42e-07	-8.09e-02	-3.06e-02
4	4.23e-07	-8.42e-07	8.09e-02	-9.64e-02
5	-2.31e-08	1.62e-07	-3.15e-02	6.70e-02
6	-3.16e-01	3.16e-01	4.17e-01	-3.82e-01
dx				
1	-6.33e-01	-6.32e-01	-1.98e-01	-2.11e-01
2	6.10e-06	6.02e-06	1.93e-02	1.74e-02
3	1.07e-06	1.40e-06	-1.60e-01	5.64e-02
4	1.06e-06	-1.40e-06	1.60e-01	-7.37e-02
5	6.09e-06	-6.03e-06	-1.93e-02	3.31e-02
6	-6.32e-01	6.33e-01	-2.08e-01	1.91e-01
dy				
1	-5.26e-06	-6.38e-06	5.00e-01	5.27e-01
2	-3.03e-06	-3.19e-06	3.05e-02	4.55e-02
3	1.70e-06	2.15e-06	2.77e-03	-1.68e-01
4	-1.70e-06	2.15e-06	2.77e-03	1.65e-01
5	3.03e-06	-3.20e-06	3.05e-02	-7.03e-02
6	-1.64e-05	1.90e-05	-5.17e-01	4.74e-01

TABLE C.17. Problem 2 with $\mathbf{P}_2^+/P_1^d$ for $a \to 0$ and Mesh 3.

β_h	2.98e-05	6.58e-03	3.24e-01	3.87e-01
cst				
1	9.91e-07	1.42e-06	-4.80e-11	8.73e-06
2	-3.30e-02	-4.75e-02	1.60e-06	-2.91e-01
3	-7.62e-03	3.03e-02	-5.67e-07	-2.43e-01
4	3.30e-02	4.75e-02	-1.60e-06	2.91e-01
5	-3.93e-11	-5.65e-11	-7.22e-11	-3.46e-10
6	-1.05e-05	-1.50e-05	-6.73e-01	1.52e-06
dx				
1	-1.32e-06	-1.90e-06	6.40e-11	-1.16e-05
2	1.02e-01	3.11e-01	-8.67e-06	1.91e-01
3	5.08e-01	-8.28e-01	1.08e-05	1.18e-01
4	-3.86e-06	8.66e-06	-1.36e-10	-3.99e-06
5	-3.75e-10	-5.40e-10	-1.72e-05	-9.12e-10
6	5.62e-06	8.07e-06	3.07e-01	6.66e-06
dy				
1	1.32e-06	1.90e-06	-6.40e-11	1.16e-05
2	-6.61e-02	-9.50e-02	3.20e-06	-5.82e-01
3	8.49e-01	4.40e-01	-2.34e-05	-2.09e-01
4	-6.61e-02	-9.50e-02	3.20e-06	-5.82e-01
5	5.59e-11	8.03e-11	5.85e-11	4.92e-10
6	1.05e-05	1.50e-05	6.73e-01	-1.52e-06

TABLE C.18. Problem 2 with $\mathbf{P}_2^+/P_1^d$ for $b \to 0$ and Mesh 1

β_h	2.24e-05	3.24e-01	3.24e-01	5.77e-01
cst				
1	-8.01e-05	6.73e-01	-1.31e-02	-1.41e-01
2	-2.66e-10	7.22e-11	-1.44e-12	1.53e-05
3	3.16e-01	3.90e-05	3.75e-05	6.29e-06
4	-3.16e-01	-3.90e-05	-3.75e-05	-6.29e-06
5	2.66e-10	-1.37e-12	-7.22e-11	-1.53e-05
6	8.01e-05	-1.31e-02	-6.73e-01	1.65e-01
dx				
1	4.30e-05	-3.07e-01	5.98e-03	-6.17e-01
2	-2.85e-09	1.72e-05	-3.35e-07	4.50e-05
3	-2.08e-05	-2.57e-09	-2.47e-09	-6.05e-05
4	2.13e-05	2.63e-09	2.53e-09	6.05e-05
5	2.89e-09	-3.35e-07	-1.72e-05	-4.77e-05
6	-4.30e-05	5.98e-03	3.07e-01	7.24e-01
dy				
1	-8.01e-05	6.73e-01	-1.31e-02	-1.41e-01
2	-3.90e-10	5.84e-11	-1.18e-12	2.16e-05
3	6.32e-01	7.80e-05	7.50e-05	3.66e-06
4	6.32e-01	7.80e-05	7.50e-05	3.66e-06
5	-3.90e-10	1.09e-12	5.84e-11	2.16e-05
6	-8.01e-05	1.31e-02	6.73e-01	-1.65e-01

TABLE C.19. Problem 2 with $\mathbf{P}_2^+/P_1^d$ for $b \to 0$ and Mesh 2.

β_h	3.74e-05	5.16e-03	2.88e-01	4.35e-01
cst				
1	-5.34e-07	-1.06e-10	1.78e-06	-1.36e-11
2	1.78e-02	1.18e-06	-5.94e-02	1.49e-07
3	-2.14e-06	-1.18e-01	-3.25e-06	-1.52e-02
4	2.14e-06	-1.18e-01	3.12e-06	-1.52e-02
5	-1.78e-02	1.18e-06	5.94e-02	1.55e-07
6	5.34e-07	-1.06e-10	-1.78e-06	-1.38e-11
dx				
1	7.12e-07	1.42e-10	-2.38e-06	1.81e-11
2	-7.12e-02	-4.72e-01	2.38e-01	-6.09e-02
3	-3.56e-01	4.41e-01	-5.78e-01	3.08e-01
4	3.56e-01	4.41e-01	5.78e-01	3.08e-01
5	7.12e-02	-4.72e-01	-2.38e-01	-6.09e-02
6	-7.12e-07	1.42e-10	2.38e-06	1.84e-11
dy				
1	-7.12e-07	-1.42e-10	2.38e-06	-1.81e-11
2	3.56e-02	4.72e-06	-1.19e-01	6.03e-07
3	-6.05e-01	-2.62e-01	3.03e-01	6.33e-01
4	-6.05e-01	2.62e-01	3.03e-01	-6.33e-01
5	3.56e-02	-4.72e-06	-1.19e-01	-6.15e-07
6	-7.12e-07	1.42e-10	2.38e-06	1.84e-11

TABLE C.20. Problem 2 with $\mathbf{P}_2^+/P_1^d$ for $b \to 0$ and Mesh 3.

APPENDIX D

Notes on the finite element implementation

The finite elements implementations have been written from scratch by the author. The code used in Chapter 2 is a 1D code written in Python using Numpy and Scipy. This code only handles piecewise linear elements both with exact and approximated quadratures. Many error measurements in various norms, as described in Chapter 2, have been implemented both for nodal and integral errors.

The code used in Chapters 3 and 4 and in Appendices B and C has been written in MATLAB. It is inspired by the implementation in [**41**] and there is not a single for-loop on elements. It drastically improve efficiency since all operation over the elements are performed vectorially. The mesh is provided by FreeFem++ (see [**82**]) because it has a very simple management of the boundary conditions for 2D problems. The code only handles affine triangles. It also has XFEM type sub-integration strategies for affine mappings alongside the collocated Lagrange multiplier as described in Appendix B. The implemented elements are: $\mathbf{P}_1^+/P_1$ (MINI), $\mathbf{P}_2 - \text{iso} - \mathbf{P}_1/P_0$, $\mathbf{P}_2/P_0$, $\mathbf{P}_2/P_1$ (Hood-Taylor), $\mathbf{P}_2^+/P_1$, and $\mathbf{P}_2^+/P_1^d$ (Crouzeix-Raviart). The version of the code used in Appendix B allows for selective type of elements between refined and non-refined elements. Also, different quadrature rules can be used for all operators and over refined and non-refined elements. Such capabilities are not implemented in the time dependent Navier-Stokes version of the code used in Chapter 4. In that version, a single element, as well as a single quadrature rule, have to be used for all elements, intersected or not. All versions of the code use backslash as linear solver.

The intersection algorithm has been also written by the author. For simple cases, such as straight lines over the whole domain, a level set approach has been used. For more complex geometries, a discrete description of the immersed boundary has to be given by set of segments. Again, there is not a single for-loop over the elements of the fluid domain in order to compute the intersections of the immersed boundary with the edges of the fluid mesh. Indeed, for a given point in the fluid domain a function evaluates all barycentric coordinates for all triangles with respect to that point. The triangle which contains the point is found if all the barycentric coordinates are positive. The algorithm then loops over all segments of the immersed boundary and all edges of the triangles (except if that edge has already been intersected). When it finds the intersected edge it moves to the next element associated to it and it reiterate until all segments of the immersed boundary have been parsed. Therefore, the algorithm loops only over intersected fluid elements. Robust implementations of segments intersections as well as right or left position of a point with respect to a segment have been used in order to avoid round-off errors.

Bibliography

1. M. Ainsworth and P. Coggins, *The stability of mixed hp-finite element methods for stokes flow on high aspect ratio elements*, SIAM J. Numer. Anal. **38** (2000), no. 5, 1721–1761.
2. S. Amdouni, M. Moakher, and Y. Renard, *A local projection stabilization of fictitious domain method for elliptic boundary value problems*, Applied Numerical Mathematics **76** (2014), 60–75.
3. T. Apel, *Anisotropic finite elements: Local estimates and applications*, Teubner, 1999.
4. T. Apel and S. Nicaise, *The inf-sup condition for low order elements on anisotropic meshes*, Calcolo **41** (2004), 89–113.
5. T. Apel and H.M. Randrianarivony, *Stability of discretizations of the stokes problem on anisotropic meshes*, Journal Mathematics and Computers in Simulation **61** (2003), 437–447.
6. F. Auricchio, D. Boffi, L. Gastaldi, A. Lefieux, and A. Reali, *On a fictitious domain method with distributed lagrange multiplier for interface problems*, accepted (2014).
7. ______, *A study on unfitted 1d finite element methods*, Computers and Mathematics with Applications **68** (2014), 2080–2102.
8. F. Auricchio, F. Brezzi, A. Lefieux, and A. Reali, *An "immersed" finite element method based on a locally anisotropic remeshing for the incompressible stokes problem*, Computer Methods In Applied Mechanics and Engineering (2014), Submitted.
9. F. Auricchio, F. Brezzi, and C. Lovadina, *Mixed finite element methods*, Encyclopedia of Computational Mechanics, John Wiley & Sons, 2004.
10. I. Babuška, *The finite element method for elliptic equations with discontinuous coefficients*, Computing **5** (1970), 207–213.
11. I. Babuška and A.K. Aziz, *On the angle condition in the finite element method.*, SIAM J. Numer. Anal. **13** (1976), no. 2, 214–226.
12. J. Baiges, R. Codina, F. Henke, S. Shahmiri, and W.A. Wall, *A symmetric method for weakly imposing dirichlet boundary conditions in embedded finite element meshes*, Int. J. Numer. Meth. Engng. **90** (2012), 636–658.
13. G.R. Barrenechea and F. Chouly, *A local projection stabilized method for fictitious domains*, Applied Mathematics Letters **25** (2012), no. 12, 2071–2076.

14. J.W. Barrett and C.M. Elliott, *Fitted and unfitted finite-element methods for elliptic equations with smooth interfaces*, IMA Journal of Numerical Analysis **7** (1987), 283–300.
15. S. Basting and M. Weismann, *A hybrid level set-front tracking finite element approach for fluid-structure interaction and two-phase flow applications*, Journal of Computational Physics **255** (2013), 228–244.
16. É. Béchet, N. Moës, and B. Wohlmuth, *A stable Lagrange multiplier space for stiff interface conditions within the extended finite element method*, Int. J. Numer. Meth. Engng. **78** (2009), 931–954.
17. R. Becker, *An adaptive finite element method for the incompressible navier-stokes equations on time-dependent domains*, Ph.D. thesis, University of Heidelberg, 1995.
18. M. Bern and D. Eppstein, *Mesh generation and optimal triangulation*, Computing in Euclidian Geometry, Lecture Notes Series on Computing, vol. 1, World Scientific, 1992, pp. 23–90.
19. S. Bertoluzza, M. Ismail, and B. Maury, *Analysis of the fully discrete fat boundary method*, Numer. Math. **118** (2011), 49–77.
20. F. Bertrand, P.A. Tanguy, and F. Thibault, *A three-dimensional fictitious domain method for incompressible fluid flow problems*, Journal for numerical methods in fluids **25** (1997), no. 25, 719–736.
21. P.B. Bochev, C.R. Dohrmann, and M.D. Gunzburger, *Stabilization of low-order mixed finite elements for the stokes equations*, SIAM J. Numer. Anal. **44** (2006), 82–101.
22. D. Boffi, F. Brezzi, and M. Fortin, *Mixed finite element methods*, Springer, 2013.
23. D. Boffi, N. Cavallini, and L. Gastaldi, *Finite element approach to immersed boundary method with different fluid and solid densities*, Mathematical Models and Methods in Applied Sciences **21** (2011), 2523–2550.
24. D. Boffi, L. Gastaldi, L. Heltai, and C.S. Peskin, *On the hyper-elastic formulation of the immersed boundary method*, Comput. Methods Appl. Mech. Engrg. **197** (2008), 2210–2231.
25. M. Braack, *A stabilized finite element scheme for the navier-stokes equations on quadrilateral anisotropic meshes*, Mathematical Modelling and Numerical Analysis **42** (2008), 903–924.
26. M. Braack and T. Richter, *Local projection stabilization for the stokes system on anisotropic quadrilateral meshes*, Numerical Mathematics and Advanced Applications, Enumath 2005, 2006.
27. E. Burman, *Projection stabilisation of lagrange multipliers for the imposition of constraints on interfaces and boundaries*, 2012.
28. E. Burman and P. Hansbo, *Fictitious domain methods using cut elements: III. a stabilized nitsche method for Stokes' problem*, Tech. report, Jönköping University, 2011.

29. G.F. Carey, *Derivative calculation from finite element solutions*, Comput. Methods Appl. Mech. Engrg. **35** (1982), 1–14.

30. G.F. Carey, S.S. Chow, and M.K. Seager, *Approximate boundary-flux calculations*, Comput. Methods Appl. Mech. Engrg. **50** (1985), 107–120.

31. P. Causin, J.F. Gerbeau, and F. Nobile, *Added-mass effect in the design of partitioned algorithms for fluid–structure problems*, Comput. Methods Appl. Mech. Engrg. **194** (2005), 4506–4527.

32. P. Causin, N.D. Dos Santos, J.-F. Gerbeau, C. Guiver, and P. Métier, *An embedded surface method for valve simulation. application to stenotic aortic valve estimation*, ESAIM: PROCEEDINGS, vol. 14, 2005, pp. 48–62.

33. S. Court, M. Fournier, and A. Lozinski, *A fictitious domain approach for the stokes problem based on the extended finite element method*, Int. J. Numer. Mech. Fluids **74** (2014), 73–99.

34. L. Beirõ da Veiga, F. Brezzi, L.D. Marini, and A. Russo, *The hitchhiker's guide to the virtual element method*, Math. Models Meth. Appl. Sci. **24** (2014), 1541–1573.

35. L. Beirão da Veiga, F. Brezzi, A. Cangiani, G. Manzini, L.D. Marini, and A. Russo, *Basic principles of virtual element methods*, Mathematical Models and Methods in Applied Sciences **23** (2013), 199–214.

36. L. Demkowicz, *A note on symmetry boundary conditions in finite element methods*, Applied Mathematics Letters **4** (1991), no. 5, 27–30.

37. N. Diniz dos Santos, *Numerical methods for fluid-structure interaction problems with valves*, Ph.D. thesis, Université Pierre & Marie Curie, 2007.

38. J. Dolbow and I. Harari, *An efficient finite element method for embedded interface problems*, Int. J. Numer. Meth. Engng. **78** (2009), 229–252.

39. J. Donea, A. Huerta, J.-Ph. Ponthot, and A. Rodríguez-Ferran, *Arbitrary lagrangian/eulerian methods*, Encyclopedy of Computational Mechanics, ch. 14, John Wiley & Sons, 2004.

40. D. Elman, H. Silvester and A. Wathen, *Finite elements and fast iterative solvers with applications in incompressible fluid dynamics*, Oxford Press, 2005.

41. H. Elman, A. Ramage, and D.J. Silvester, *Ifiss, a matlab toolbox for modelling incompressible flow*, ACM Transctions on Mathematical Software (2007).

42. A. Ern and J.-L. Guermond, *Theory and practice of finite elements*, Springer, 2004.

43. B. Fabrèges, *Une méthode de prolongement régulier pour la simulation d'écoulements fluide/particules*, Ph.D. thesis, Université Paris-Sud, 2012.

44. B. Fabrèges, L. Gouarin, and B. Maury, *A smooth extension method*, Comptes Rendus - Mathématiques **351** (2013), 361–366.

45. S. Frei and R. Richter, *A locally modified parametric finite element method for interface problems*, SIAM J. Numer. Anal. **52** (2014), no. 5, 2315–2334.

46. P.J. Frey and P.-L. George, *Mesh generation*, Wiley, 2008.

47. T.-P. Fries and T. Belytschko, *The extended/generalized finite element method: An overview of the method and its applications*, Int. J. Numer. Meth. Engng. **84** (2010), 253–304.

48. A. Gerstenberger and W.A. Wall, *An eXtended Finite Element Method/Lagrange multiplier based approach for fluid-structure interaction*, Comput. Methods Appl. Mech. Engrg. **197** (2008), 1699–1714.

49. A. Gil, A. Arranz Carreño, J. Bonet, and O. Hassan, *The immersed structural potential method for haemodynamic applications*, Journal of Computational Physics **229** (2010), 8613–8641.

50. V. Girault and R. Glowinski, *Error Analysis of Fictitious Domain Method Applied to a Dirichlet Problem*, Japan J. Indust. Appl. Math. **12** (1995), 487–514.

51. V. Girault, R. Glowinski, and T. Pan, *A fictitious-domain method with distributed multiplier for the stokes problem*, Applied Nonlinear Analysis, Kluwer Academic/Plenum Publishers, 2002, pp. 159–174.

52. R. Glowinski, *Handbook of numerical analysis: Numerical methods for fluids (part 3)*, vol. 9, ch. VIII, North-Holland, 2003.

53. A. Hannukainen, S. Korotov, and M. Křížek, *The maximum angle condition is not necessary for convergence of the finite element method*, Numer. Math. **120** (2012), 79–88.

54. A. Hansbo and P. Hansbo, *An unfitted finite element method, based on Nitsche's method, for elliptic interface problems.*, Comput. Methods Appl. Mech. Engrg. **191** (2002), 5537–5552.

55. P. Hansbo, M.G. Larson, and S. Zahedi, *A cut finite element method for a stokes interface problem*, Applied Numerical Mathematics **85** (2013), 90–114.

56. P. Hansbo, C. Lovadina, I. Perugia, and G. Sangali, *A lagrange multiplier method for the finite element solution of elliptic interface problems using non-matching meshes*, Numer. Math. **100** (2008), 91–115.

57. J. Haslinger and Y. Renard, *A new fictitious domain approach inspired by the extended finite element method*, SIAM J. Numer. Anal. **47** (2009), 1474–1499.

58. M. Hautefeuille, C. Annavrapu, and J.E. Dolbow, *Robust imposition of dirichlet boundary conditions on embedded surfaces*, Int. J. Numer. Meth. Engng. **90** (2012), 40–64.

59. L. Heltai and F. Costanzo, *Variational implementation of immersed finite element methods*, Comput. Methods Appl. Mech. Engrg. **229-232** (2012), 110–127.

60. John G. Heywood, Rolf Rannacher, and Stefan Turek, *Artificial boundaries and flux and pressure conditions for the incompressible Navier-Stokes equations*, Internat. J. Numer. Methods Fluids **22** (1996), no. 5, 325–352.

61. F. Ilinca and J.-F. Hétu, *A finite element immersed boundary method for fluid flow around rigid objects*, Int. J. Numer. Meth. Fluids **65** (2011), 856–875.

62. P. Jamet, *Estimations d'erreur pour des éléments finis droits presque dégénérés*, RAIRO. Analyse Numérique **10** (1976), 43–60.

63. L. Kamenski, W. Huang, and H. Xu, *Conditioning of finite element equations with arbitrary anistropic meshes*, Mathematics of Computations **83** (2014), no. 289, 2187–2211.

64. R.B. Kellogg, *Singularities in interface problems*, Numerical Solution of Partial Differential Equations, Academic Press, 1971, pp. 351–400.

65. M. Křížek, *On semiregular families of triangulations and linear interpolation*, Applications of Mathematics **36** (1991), no. 3, 223–232.

66. K. Lemrabet, *Régularité de la solution d'un problème de transmission*, J. Math. Pures. Appl. **9** (2977), no. 56, 1–38.

67. A.J. Lew and G.C. Buscaglia, *A discontinuous-galerkin-based immersed boundary method*, Int. J. Numer. Meth. Engng. **76** (2008), 427–454.

68. J. Li, J.M. Melenk, B. Wohlmuth, and J. Zou, *Optimal a priori estimates for higher order finite elements for elliptic interface problems*, Applied Numerical Mathematics **60** (2010), 19–37.

69. Z. Li, *The immersed interface method using a finite element formulation*, Applied Numerical Mathematics **27** (1998), 253–267.

70. Z. Li and K. Ito, *The immersed interface method*, SIAM, 2006.

71. Q. Liao and D. Silvester, *Robust stabilized stokes approximation methods for highly stretched grids*, IMA Journal of Numerical Analysis **33** (2013), 413–431.

72. Rainald Löhner, *Applied computational fluid dynamics techniques, an introduction based on finite element methods*, John Wiley and Sons, 2008.

73. G. Lube, T. Knopp, and R. Gritzki, *Stabilized fem with anisotropic mesh refinement for the Oseen problem*, Numerical Mathematics and Advanced Applications, Springer-Verlag, 2006.

74. B. Maury, *A fat boundary method for the poisson problem in a domain with holes*, J. Sci. Comput. **16** (2001), 319–339.

75. ______, *Numerical analysis of a finite element/volume penalty method*, SIAM J. Numer. Anal. **47** (2009), no. 2, 1126–1148.

76. S. Micheletti, S. Perotto, and M. Picasso, *Stabilized finite elements on anisotropic meshes: A priori error estimates for the advection-diffusion and the stokes problems*, SIAM J. Numer. Anal. **41** (2004), no. 3, 1131–1162.

77. S. Nicaise, *Polygonal interface problems*, Peter Lang, 1993.

78. J. Parvizian, A. Düster, and E. Rank, *Finite cell method*, Computational Mechanics **41** (2007), 121–133.

79. G. Pedrizzetti, *Kinematic characterization of valvular opening*, Physical Review Letters **95** (2005), 194502.

80. G. Pedrizzetti and F. Domenichini, *Flow-driven opening of a valvular leaflet*, J. Fluid Mech. **569** (2006), 321–330.

81. C. S. Peskin, *The immersed boundary method*, Acta Numerica (2002), 1–39.

82. O. Pironneau, F. Hecht, A Le Hyaric, and J. Morice, *Freefem++*.

83. J. D. Sanders, J. E. Dolbow, and T. A. Laursen, *On methods for stabilizing constraints over enriched interfaces in elasticity*, Int. J. Numer. Meth. Engng. **78** (2009), 1009–1036.

84. J.D. Sanders, T.A. Laursen, and M.A. Puso, *A Nitsche embedded mesh method*, Computational Mechanics **49** (2012), 243–257.

85. D. Schötzau and C. Schwab, *Mixed hp-fem on anisotropic meshes*, Math. Models Meth. Appl. Sci. **8** (1998), 787–820.

86. D. Schötzau, C. Schwab, and R. Stenberg, *Mixed hp-fem on anisotropic meshes ii: Hanging nodes and tensor products of boundary layer meshes*, Numer. Math. **83** (1999), 667–697.

87. R. Stenberg, *On some techniques for approximating boundary conditions in the finite element method*, J. Comp. Appl. Maths. **63** (1995), 139–148.

88. K. Takizawa, Y. Bazilevs, and E. Tezduyar, *Computational fluid mechanics and fluid-structure interaction*, Computational Mechanics **50** (2012).

89. E.H. van Brummelen, K.G. van der Zee, V.V. Garg, and S. Prudhomme, *Flux evaluation in primal and dual boundary-coupled problems*, J. Appl. Mech. **79** (2011), 010904.

90. R. van Loon, P.D. Anderson, J. de Hart, and F.P.T. Baaijens, *A combined fictitious domain/adaptive meshing method for fluid-structure interaction in heart valves*, Int. J. Numer. Mech. Fluids **46** (2004), 533–544.

91. R. van Loon, P.D. Anderson, and F.N. van de Vosse, *A fluid-structure interaction method with solid-rigid contact for heart valve dynamics*, Journal of Computational Physics **217** (2006), 806–823.

92. R. van Loon, P.D. Anderson, F.N. van de Vosse, and S.J. Sherwin, *Comparison of various fluid-structure interaction methods for deformable bodies*, Computers & Structures **85** (2007), no. 11-14, 833 – 843.

93. A. Veneziani, *Boundary conditions for blood flow problems*, Proceedings of ENUMATH97 (R. Rannacher, H. G. Bock, G. Kanschat, F. Brezzi, R. Glowinski, Y.A. Kuznetsov, and J. Périeux, eds.), World Scientic: River edge, NJ, 1998, pp. 596–605.

94. P.E.J. Vos, R. van Loon, and S.J. Sherwin, *A comparaison of fictitious domain methods appropriate for spectral/hp element discretisations*, Comput. Methods Appl. Mech. Engrg. **197** (2008), 2275–2289.

95. M. Vukicevic and G. Pedrizzetti, *Role of inertia in the interaction between oscillatory flow and a wall-mounted leaflet*, Physical Review E **83** (2011), 016310.

96. A. Ženíšek, *The convergence of the finite element method for boundary value problems of a system of elliptic equations (in czech)*, Apl. Mat. **14** (1969), 355–377.

97. W. A. Wall, A. Gerstenberger, P. Gamnitzer, C. Förster, and E. Ramm, *Large deformation fluid-structure interaction - advances in ALE methods and new fixed grid approaches*, Lectures Notes in Computational Science and Engineering: Fluid-Structure Interaction (H.-J. Bungatz and M. Schäfer, eds.), vol. 53, Springer, 2006.

98. M. Zlámal, *On the finite element method*, Numer. Math. **12** (1968), 394–409.